博士論文

Study of polymeric nanocarrier design on the membrane transporter mediated-targeting of the central nervous system

(中枢神経系を標的としたトランスポーター介在薬剤送達システムの基礎的解析)

中村　乃理子

Preface

This dissertation presents results of my three-year research performed in Associate Professor Horacio Cabral's Laboratory from 2018 to 2021 as a doctoral course student. This study focused on understanding of structural design on polymeric nanocarrier as membrane transporter-mediated targeting of the central nervous system.

I believe that this work has made significant contribution to the understanding and further application of nanoparticulated polymeric drug delivery carrier to the brain mediated by membrane transporters. I would like to express my sincere gratitude to all of mi supervisors and colleagues for their invaluable support and suggestion.

Noriko NAKAMURA

Department of Bioengineering, Graduate School of Engineering

The University of Tokyo

March 2021

Acknowledgement

I would like to express my sincere gratitude to Associate Professor Horacio Cabral for offering my great opportunities and insightful advices throughout the course of my study.

I am wholeheartedly thankful to Associate Professor Yasutaka Anraku for their valuable support and instructions as my direct mentors to proceed with my research activities.

I sincerely appreciate Professor Kazunori Kataoka for his insightful advuces throughout the course of my study.

I am deeply grateful to Dr. Kazuko Toh for her technical instructions in intravital real-time laser confocal microscopy observation. I appreciate Dr. Yuki Mochida for his technical instructions in small angle X-ray scattering measurement. I would like to thank Mr. Shigeto Fukushima for the polymer synthesis. I appreciate Ms. Mai Kaneko for her valuable assistance in animal experiments and polymer synthesis.

I am deeply grateful to Ms. Hiroko Koyama for her secretarial assistance and her kindness for my research activities. I also thank all of the lab members for fruitful discussions and kind help.

I am much obliged to financial supports of the research fellowship from the Japan Society for Promotion of Science (JSPS), Specially Promoted Research from the Ministry of Education, Culture, Sports, Science, and Technology (MEXT) of Japan, the Center of Innovation (COI) Program from the Japan Science and Technology Agency (JST) and the Strategic Research Program for Brain Sciences from Japan Agency for Medical Research and Development (AMED).

Finally, I would like to express my deep gratitude to my family for their consistent support and encouragement throughout my life.

Contents

Chapter 1.
General introduction

1. 1. Nanoparticulated drug delivery carriers

The development of delivery methodology of medical agents to the specific diseased organs and cells is crucial for the therapy and diagnosis of patients so that it is one of the most crucial research subjects in this 21st century. Drug delivery system (DDS) is described as the system which enables providing a foreign medical agent to specific target organs, tissues as well as cells inside the body. These developed systems improve effectivity by incrementing the concentration of molecular agents at a target site as long as simultaneously reducing the toxicity by minimizing the off-targeted accumulation and clearance *in vivo*. There have been significant progresses in the development of therapeutic methods as well as novel imaging tools.

The major goal of the development of DDS carrier is circulating under the bloodstream stably, avoiding non-specific interactions with ingredients in the blood compartment, also with the reticuloendothelial systems (RES)[1], as well as selectively exploding at the targeted disease tissue, which is followed by the internalization with targeted sites. Nanoparticulated DDS carriers achieve the low volume of distribution to non-targeted organs so as the extravasation of these carriers in healthy tissues is limited due to the stable and tight covering of blood vasculatures in these tissues[1-6]. Nanoparticulated DDS carriers with macromolecular characteristics also restrain their renal clearance from the kidney since the verge size for glomerular filtration is relatively 50 kDa[7], in other words 6 nm[8], so that the half-life of loaded drugs is significantly extended. Furthermore, the modification of carriers with bioadaptable hydrophilic materials for example poly(ethylene glycol) (PEG) is crucial to escape from the recognition by opsonin proteins that facilitate the recognition and eradication of exogenous agents from the blood circulation system by the RES. PEGylation of

nanoparticulated DDS carriers results in reduced unspecific distribution and impaired pharmacokinetic features principally[1, 9-10]. Additionally, the size and the surface charge of the nanoparticulated carriers determines their biodistribution. Nanoparticles (NPs) with a diameter of smaller than 150 nm are inclined to accumulate to the liver on the other hand NP larger than 150 nm retained in the spleen[11-12]. NPs with the positively charged surface property are rapidly captured by the liver, spleen and lungs while neutral or negatively charged materials show prolonged blood circulation caused by much lower opsonization rate[11]. The translational clinical trial of some of nanoparticulated delivery systems supports the proposal to the development of effective therapeutic method[13-15]. Among these translational strategies, polymeric micelles have been demonstrating advantages for incorporating a various type of medical agents and overwhelming biological barriers locating on the way to the targeted tissue[16].

1. 2. Polymeric micelles for drug delivery

Precisely designed amphiphilic block copolymers spontaneously provide polymeric micelles with a core-shell phase separated construction with a hydrophobic inner core surrounded by a hydrophilic outer shell in aqueous media[17]. These amphiphilic block copolymers and their self-assemblages broadly have been explored from basic to applied science for several decades. This point of view has been motivated by the block copolymers characteristics such as narrow molecular weight distribution and compartmentalized segments for phase separation forming highly hierarchical structures like micelles, rods and vesicles. In addition to the fundamental understanding, polymeric micelles have been demonstrating great potential as DDS carrier due to its unique features. A hydrophilic shell constructed with PEG chains provides the solubility into the water *via*

steric stabilization and also harmoniousness with the biological system and a stealth effect in the bloodstream[18-19]. Systemically controlled the structure of a segment forming the core facilitates the structural stability of micelles and the ability to encapsulate a various type of medical agents such as drugs and imaging agents. Moreover, polymeric micelle are more stable and can maintain loaded drugs in it under the diluted condition in the biological system for longer time period in contrast to micelles from small surfactants[20].

In particular, PEG-poly(amino acid) block copolymers, which are synthesized by the ring-opening polymerization of N-carboxy-anhydrides from a ω-terminal amine of PEG, have advantage to be prepared as a platform of DDS carrier for varying drugs because functional groups in the core-forming segments are useful to introduce drugs into the core. Different intermolecular driving forces for micellar formation are available, such as hydrophobic interactions[21-23], electrostatic interactions[24-27], metal complexation[28-29] and hydrogen bonding[30]. Additionally, the variety of the intermolecular interaction constructing core of polymeric micelles may regulate the prolonged circulation of polymeric micelles in the bloodstream.

1. 3. Ligand-installed polymeric micelles

Polymeric micelles loading anti-cancer drugs with a diameter of several tens nm are most likely to selectively accumulate to tumor trough the enhanced permeability and retention (EPR) effect, which occurs from the hyperpermeable vasculature, active opening the vasculature walls of tumor tissues and the defective lymphatic draining from the tumors (**Figure 1-1. (a)**)[31-33]. Recently, it has been indicated that certain histological features, like blood vessel biological process, compression of the vasculature, stroma and stiffness of tumor tissues, restrain the efficiency of EPR effect especially for bigger

polymeric micelles[34]. In addition, the effect of EPR on early metastatic tumors remains poorly understood and hydrophilic shells extend half-life of polymeric micelles in the bloodstream while impair the uptake to targeted cells, which is known as the "PEG dilemma". Therefore, novel strategies should be developed to improve the accumulation of polymeric micelles into tumor tissues disregarding EPR and cellular internalization.

Installing ligands on the surface of nanoparticulated carriers with strong adsorptoin to unique cellular marker proteins on the targeted cells for the purpose of enhancing targeting and internalization of carriers to targets (**Figure 1-1. (b)**)[35-36]. Ligand-installed nanoparticulated carriers can achieve improved tumor extravasation be recognizing markers in the tumor vasculature[37-38], deeper penetration to the tumor[39], increased cellular binding[40-41] and uptake in the tumor and promoted intracellular delivery[42]. Furthermore, ligand-installed nanoparticulated carriers has great potential to overcome biological barriers in the vasculature and enable the extravasation and accumulation in impermeable tissues like brain.

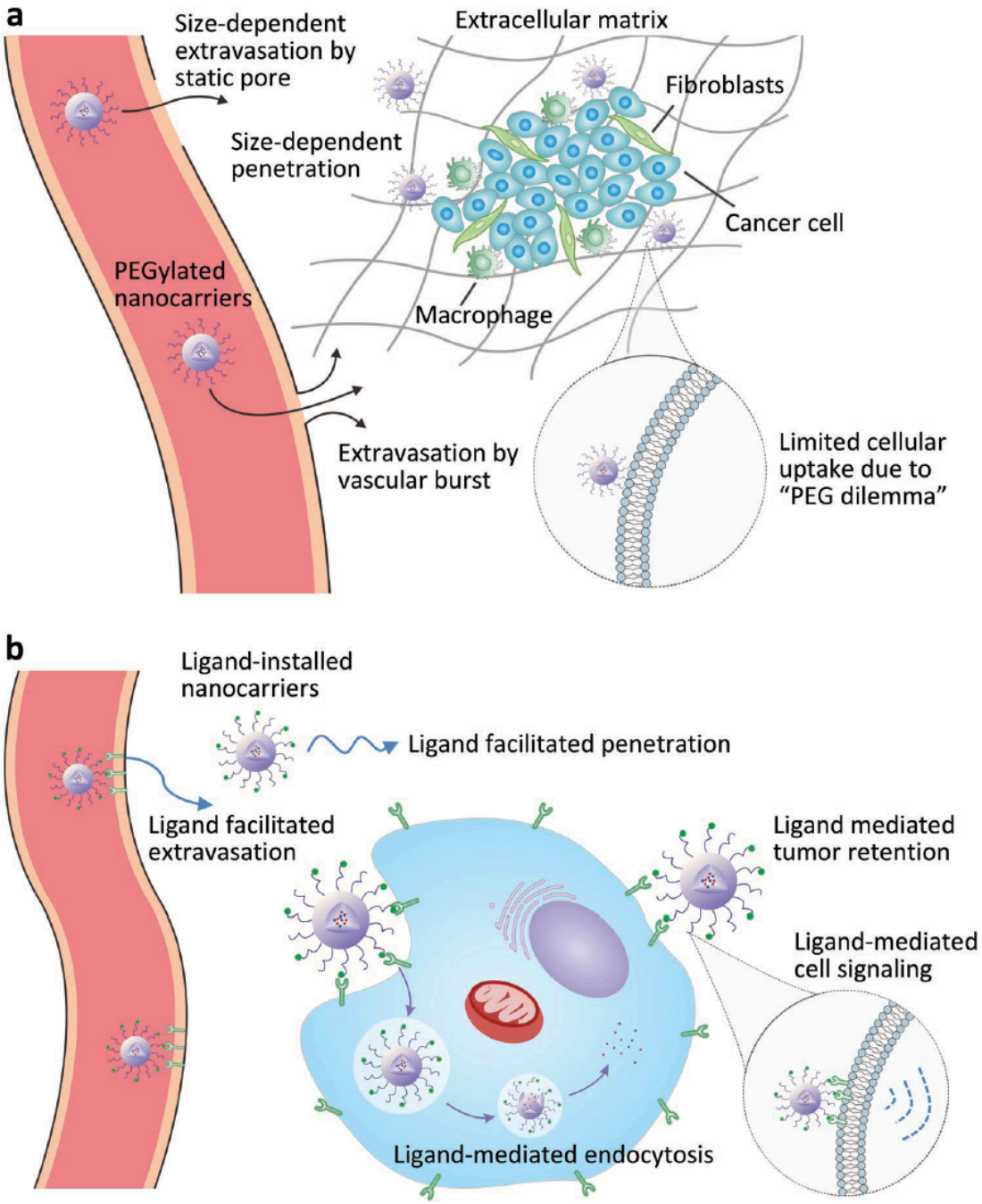

Figure 1-1. Tumor targeting by nanoparticulated carriers (a) and ligand-installed nanoparticulated carriers (b)[43]

1. 4. Ligand-installed drug delivery targeting the blood-brain barrier

The vasculature barrier between the systemic circulation and the brain, which is known as the blood-brain barrier (BBB) is designed to secure the brain from exogenous pathogens. Nanoparticulated carriers installing ligand molecules has been developed for crossing the BBB for drug delivery to the central nervous system (CNS) and made significant progress because the BBB is a challenging obstruction for biofunctional molecules and imaging probes to deliver to the brain. The BBB is consisted with multicellular vasculature structure (for example capillary endothelial cells forming continuous intracellular tight junctions) (**Figure 1-2.**) consisting the interface between the blood circulation system and the CNS for the purpose of maintaining brain homeostasis and to regulate influx/efflux transport[44]. The BBB limitedly allows modest types of molecules to pass through, such as oxygen, small hydrophobic molecules (like ethanol), solutes (like nutrients) and specific proteins or peptides trough the receptor-mediated transcytosis[45] (**Figure 1-3.**). Nevertheless, several diseases occur in the CNSsuch as Parkinson's disease (PD) and Alzheimer's disease (AD). It is essential to have the capability to deliver bioactive molecules or imaging agents to the brain for the development of therapeutic strategies for these CNS disorders. Recently, there has been explored several ligands which have binding affinity to endothelial markers for crossing the BBB, for example, transferrin (Tf) peptide binding to Tf receptors (TfRs)[46], angiopep-2 binding to low-density lipoprotein receptor-related protein-1 (LRP-1)[47] and glucose transporter-1 (GLUT-1) antibody scFv binding to GLUT-1[48].

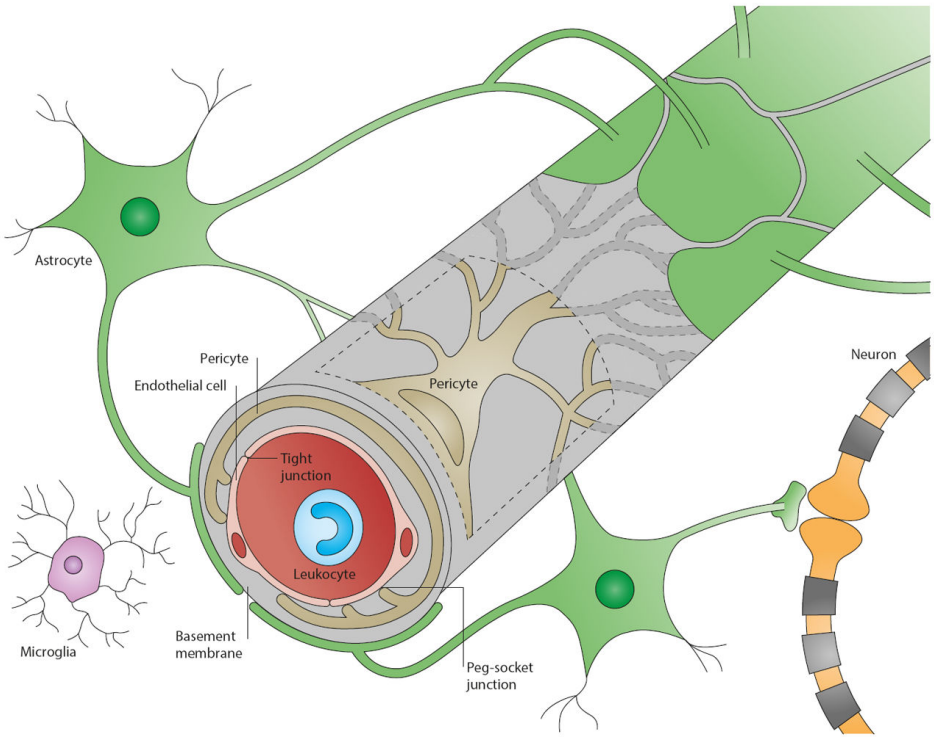

Figure 1-2. Cellular interplay at the BBB

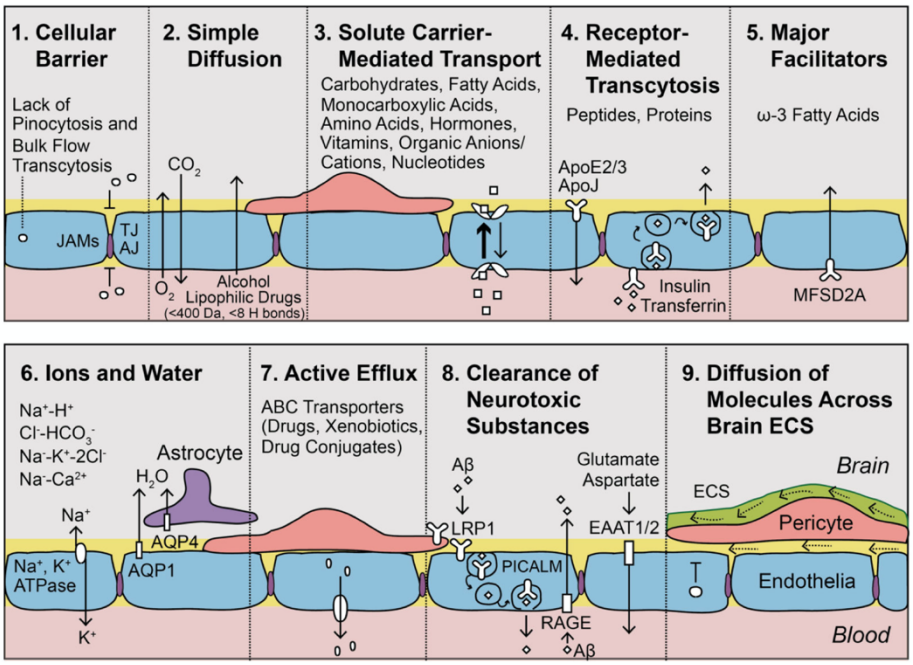

Figure 1-3. Key transport roles in BCECs

1. 5. Glucose-decorated polymeric micelle as drug delivery carrier to the brain

Emerging ligand strategies targeting membrane transporters by using the small molecules that pass through them have attracted much attention for developing nanoparticulated carriers capable of overcoming tissue and cellular barriers [49]. Among the research on transporter-guided delivery, substantial efforts have been dedicated to develop glucosylated nanocarriers for targeting the glucose transporter (GLUT), as it is one of the most overarching membrane transporters due to its central roles in tissue homeostasis and diseases[38, 50-51]. For example, GLUT-1 is overexpressed on cancer cells to promote increased glycolysis rate of tumors, or on brain capillary endothelial cells (BCECs) for actively taking glucose due to the accelerated metabolism in the brain, and because otherwise glucose cannot pass through the tight BBB protecting theCNS. However, the development of glucosylated nanocarriers effectively targeting GLUT-1 is challenging as the binding affinity of glucose to GLUT-1 is low (K_D = 3 mM) because it assumes channel transportation of glucose passing in or out of the cells [52] and the intrinsic glucose molecules in blood compete for the binding sites.

Recently, our lab have succeeded to use the GLUT-1 on BCECs for effectively overcoming the BBB by developing polymeric micelle decorated with multiple glucose molecules(G-PM)[53] (**Figure 1-4.**), which allowed effective delivery of Fab fragment of antibodies[54] and antisense oligonucleotides[55] into the brain after intravenous injection. These G-PMs benefited from the accelerated translocation of GLUT-1 from the apical side to the basal side after a period of fasting followed by administration of free glucose, which simultaneously transfers the multi-glucosylated micelles bound to the GLUT-1 to the brain parenchyma. These findings indicate that the binding/dissociation balance of multi-glucosylated micelles to/from GLUT-1 is important in the serial process of binding-

translocation-release at the BBB. In this regard, the balance between binding and dissociation of multi-glucosylated micelles is necessarily managed by controlling the density of glucose ligands on the nanocarrier surface for tuning the multivalent interactions, by which the whole affinity is determined as the integration of the weak affinity between each component, *i.e.* glucose and GLUT-1[56] (**Figure 1-5.**). Thus, the crucial parameters involved in multivalent interactions are (i) the number of ligand molecules on each nanocarrier and (ii) the accessibility to GLUT-1 for the glucose molecules on the surface of nanocarriers. Making further reference to the second parameter, the steric repulsive effect of glucose ligands on the surface of nanoparticles should be considered because the recognition site of GLUT-1 is located in a recessed position with low accessibility[57]. Such steric repulsion may be alleviated by inserting flexible spacers to the glucose ligands for promoting effective binding to GLUT-1. In fact, it has been reported that the spacer effect improves the binding between proteins and nanoparticles decorated with ligands having relatively weak molecular interactions, for example, lectins and sugar-installed nanoparticles [58-59].

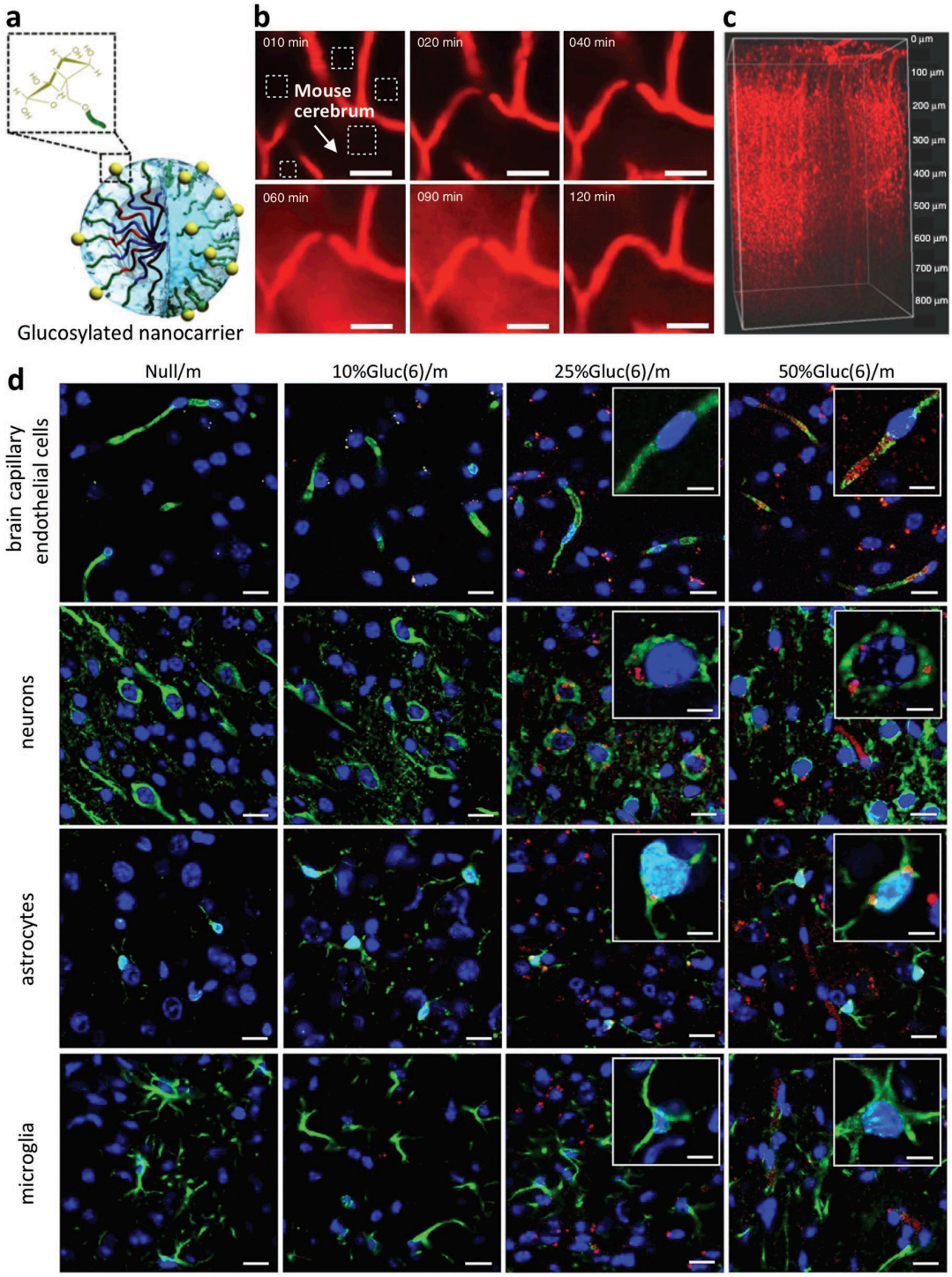

Figure 1-4. G-PM as a drug delivery carrier targeting the brain (a) scheme of G-PM, (b) real time observation of G-PM crossing the BBB, (c) G-PM in the mice cerebrum observed using intravital two-photon microscopy and (d) immunohistochemical staining of mice brains

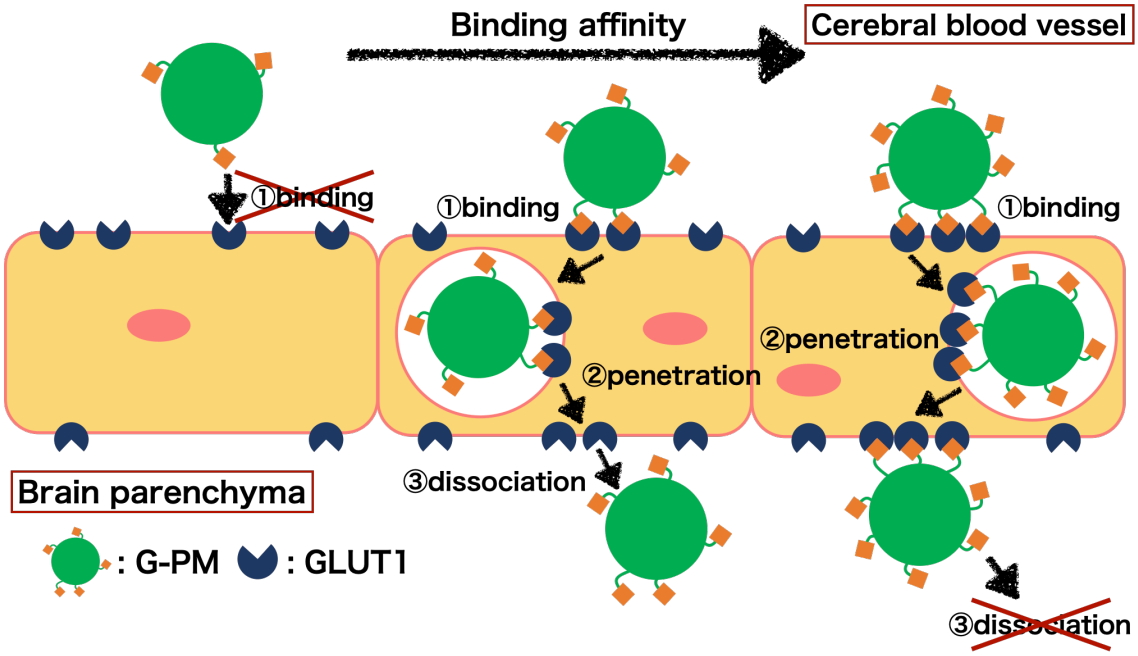

Figure 1-5. Binding/dissociation balance of multi-glucosylated polymeric micelles to/from GLUT-1

1. 6. Spacer effect of polymer chains on nanoparticles

There have been reported successful target recognition of ligand-installed nanoparticulated carriers by many previous researches. Among them, not many studies have considered about fundamental aspects, such as the effect of the length of PEG chains, flexibility, and conformational state on ligand-receptor interactions[58, 60-62]. One of the drawbacks of the PEGylation with single chain length is that PEG chains and ligand molecules conjugated to the end of them are likely to be interference from neighboring PEG strands (**Figure 1-6. (a)**). The mobility of ligands as well as the flexibility of PEG strands are possibly reduced by the neighboring PEG strands so that the recognition ability of ligand molecules to the target membrane protein is reduced[60-61]. To overcome this drawback, the technique called “cocktail PEGylation”, which tether shorter PEG

chains between ligand-conjugated longer PEG chains, is suggested to be useful because it alleviates the interfering effect of neighboring PEG without compromising their surface functions for negligible unspecific protein adsorption (**Figure 1-6. (b)**). Cocktail PEGylation generates the spacer effect for ligand-conjugated longer PEG chains, followed by enhanced mobility of ligand molecules for improved accessibility to the target membrane proteins[59, 63-64].

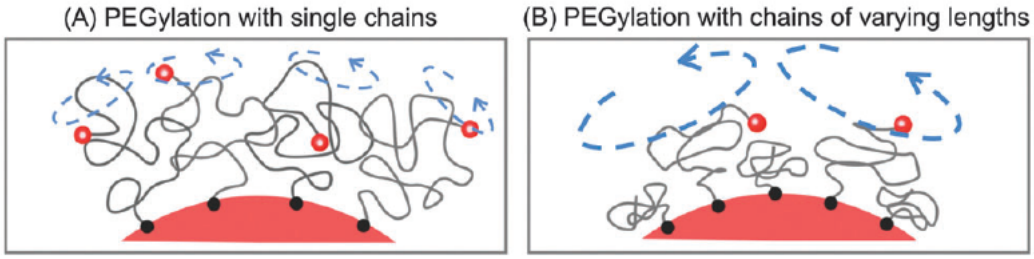

Figure 1-6. Spacer effects generated by cocktail PEGylation (a) restrained ligand mobility by neighboring PEG chains and (b) rescued ligand mobility by shorter PEG chains

1. 7. Polyion complex nanoparticles

With the progress of polymer technology, self-assembled supramolecular structures of precisely designed polymers have been receiving much attention for both fundamental studies[65-66] and development of functional biomaterials[67-68]. Among supramolecular assemblies, polyion complexes (PICs), which are formed by electrostatic interaction between oppositely charged polymers in aqueous conditions without using organic solvents, have shown exceptional features for constructing biomaterials with controlled behavior at the biointerface and wide-range applicability, such as DDS[16, 69], bio-imaging [70] and artificial organelles[71].

PIC structures are versatile biomaterials with the ability to obtain different physical properties based on the same polymer combination just by changing the surroundings, such as the ionic strength of solvent [72-73] and environmental pH [74], as well as by controlling parameters of the polymers in the mixture, including the degree of polymerization of charged segments [75], the polymer concentration and the mixing charge ratio [24]. For example, tuning the chain length of the charged segments and the ionic strength of solvents resulted in different PIC structures in solution, precipitate and coacervate states[12, 76]. Nevertheless, effective control of PIC assembly is challenging, and slight variations in the abovementioned factors may lead to catastrophic changes in the nanostructures.

We have been developing various types of PIC assemblies formed by block aniomers and block catiomers consisting of PEG as a hydrophilic segment and polyamino acids as the charged blocks. These PIC assemblies have been effectively used as nanocarriers for drug and gene delivery[53]. The approach allows preparing a wide variety of PIC structures with nano- and micron-sized architectures by controlling the dimensional influence of the charged segment[77], the weight fraction of PEG[78] and the ionic strength[79]. In addition, PIC assemblies, such as micelles and vesicles, are appropriate for investigating the surface structural parameters as DDS carrier because of its stability in the biological system.

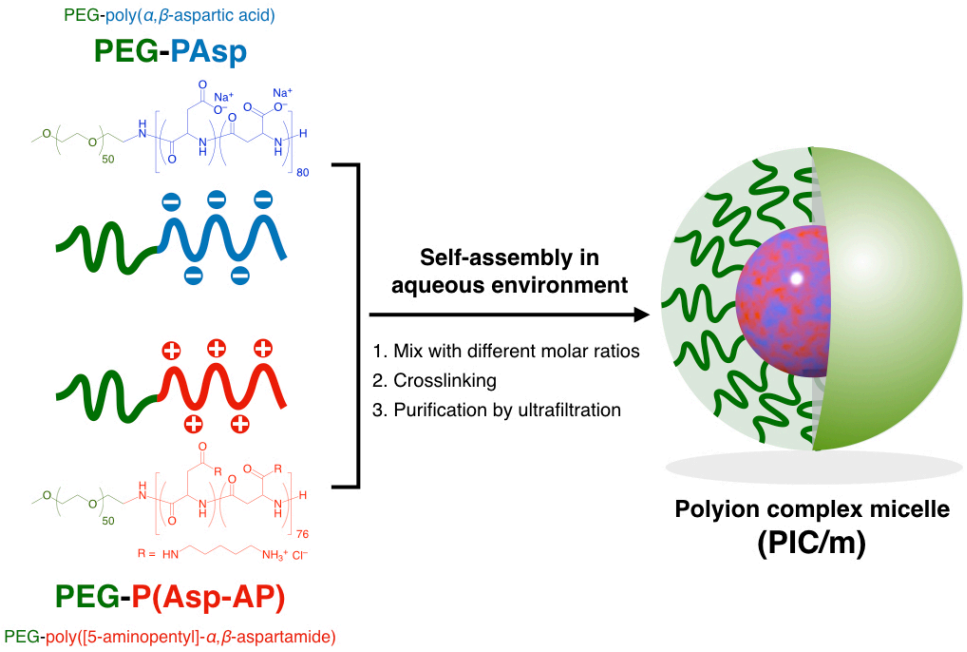

Scheme 1-1. Preparation of PIC micelle via self-assembly driven by electrostatic interaction between oppositely charged block copolymers in *the chapter 2*

1. 8. Overview of this dissertation

1. 8. 1. Significance of this study

Polymeric micelles have been demonstrated great advantages as DDS carrier for cancer therapy due to its unique features rather than other nanoparticulated carriers. In this century, ligand-installed polymeric micelles have attracted attentions as active targeting DDS carriers for the development of therapeutic method of tumors cannot be targeted by EPR effect as well as CNS disorders because of their potential to overcome blood-brain barrier, which is the biological barrier protecting the brain from exogenous molecules including drug. Moreover, one of the major characteristics of polymeric micelles is flexible chemical structure of a side chain in core-forming segment which enables loading of diverse types of drugs by introducing functional groups there. Nevertheless, general structural parameters which do not affected by encapsulated drugs

have rarely been reported yet, there is no platform for DDS towards brain with high efficiency in spite of urgent requirement for neurodegenerative diseases therapy.

1. 8. 2. Outline of this study

This thesis consists of following chapters.

Chapter 1 gives general introduction of nanoparticulated DDS carriers, in particular, ligand-installed polymeric micelle for active targeting as well as PIC micelle as a platform of DDS carrier for the investigation of universal structural parameter of it regardless of the type of encapsulating drugs, describing background of this study.

Chapter 2 describes the structural characteristics of PIC micelles prepared with varying charge mixing ratio in oppositely charged segment in the core. Hydrophilic surface properties, such as size distribution, morphology and surface potential, as well as structural properties attributed by core-forming segment which have hardly ever been described were investigated. Moreover, the performance of PIC micelle with different structural features in the core in the biological system were evaluated, and then the essential parameters of PIC micelle as a DDS carrier were proposed.

Chapter 3 describes the target efficiency of G-PM, the ligand-installed DDS carrier actively targeting BBB, was evaluated, and then crucial parameters which determine the binding affinity of G-PM to target membrane protein (GLUT-1) were defined; 1) chain length of hydrophilic segment and 2) distance between two ligand molecules on the surface of micelles.

Chapter 4 describes the fabrication of G-PM with cocktail PEGylation, which is a technique improving accessibility of ligand molecules conjugated to longer PEG chain to target membrane proteins. Cocktail PEGylation demonstrated dramatically improved brain delivery of G-PM.

Chapter 5 gives overall conclusions and future perspectives of this study.

1. 9. References

1. Petros, R. A.; DeSimone, J. M., Strategies in the design of nanoparticles for therapeutic applications. *Nat Rev Drug Discov* **2010,** *9* (8), 615-27.

2. Kataoka, K.; Harada, A.; Nagasaki, Y., Block copolymer micelles for drug delivery: design, characterization and biological significance. *Adv Drug Deliv Rev* **2001,** *47* (1), 113-31.

3. Kabanov, A. V.; Batrakova, E. V.; Alakhov, V. Y., Pluronic block copolymers as novel polymer therapeutics for drug and gene delivery. *J Control Release* **2002,** *82* (2-3), 189-212.

4. Peer, D.; Karp, J. M.; Hong, S.; Farokhzad, O. C.; Margalit, R.; Langer, R., Nanocarriers as an emerging platform for cancer therapy. *Nature Nanotechnology* **2007,** *2* (12), 751-760.

5. Davis, M. E.; Chen, Z. G.; Shin, D. M., Nanoparticle therapeutics: an emerging treatment modality for cancer. *Nat Rev Drug Discov* **2008,** *7* (9), 771-82.

6. Lammers, T.; Hennink, W. E.; Storm, G., Tumour-targeted nanomedicines: principles and practice. *Br J Cancer* **2008,** *99* (3), 392-7.

7. Rappaport, J.; Hanss, B.; Kopp, J. B.; Copeland, T. D.; Bruggeman, L. A.; Coffman, T. M.; Klotman, P. E., Transport of phosphorothioate oligonucleotides in kidney: implications for molecular therapy. *Kidney Int* **1995,** *47* (5), 1462-9.

8. Choi, H. S.; Liu, W.; Misra, P.; Tanaka, E.; Zimmer, J. P.; Itty Ipe, B.; Bawendi, M. G.; Frangioni, J. V., Renal clearance of quantum dots. *Nat Biotechnol* **2007,** *25* (10), 1165-70.

9. Storm, G.; Belliot, S. O.; Daemen, T.; Lasic, D. D., Surface modification of nanoparticles to oppose uptake by the mononuclear phagocyte system. *Advanced Drug*

Delivery Reviews **1995,** *17* (1), 31-48.

10. Owens, D. E., 3rd; Peppas, N. A., Opsonization, biodistribution, and pharmacokinetics of polymeric nanoparticles. *Int J Pharm* **2006,** *307* (1), 93-102.

11. Nel, A. E.; Madler, L.; Velegol, D.; Xia, T.; Hoek, E. M.; Somasundaran, P.; Klaessig, F.; Castranova, V.; Thompson, M., Understanding biophysicochemical interactions at the nano-bio interface. *Nat Mater* **2009,** *8* (7), 543-57.

12. Anraku, Y.; Kishimura, A.; Kobayashi, A.; Oba, M.; Kataoka, K., Size-controlled long-circulating PICsome as a ruler to measure critical cut-off disposition size into normal and tumor tissues. *Chemical Communications* **2011,** *47* (21), 6054-6056.

13. Allen, T. M.; Cullis, P. R., Liposomal drug delivery systems: from concept to clinical applications. *Adv Drug Deliv Rev* **2013,** *65* (1), 36-48.

14. Cabral, H.; Kataoka, K., Progress of drug-loaded polymeric micelles into clinical studies. *J Control Release* **2014,** *190*, 465-76.

15. Wicki, A.; Witzigmann, D.; Balasubramanian, V.; Huwyler, J., Nanomedicine in cancer therapy: challenges, opportunities, and clinical applications. *J Control Release* **2015,** *200*, 138-57.

16. Cabral, H.; Miyata, K.; Osada, K.; Kataoka, K., Block Copolymer Micelles in Nanomedicine Applications. *Chem Rev* **2018,** *118* (14), 6844-6892.

17. Kazunori, K.; Glenn S, K.; Masayuki, Y.; Teruo, O.; Yasuhisa, S., Block copolymer micelles as vehicles for drug delivery. *Journal of Controlled Release* **1993,** *24* (1), 119-132.

18. Jeon, S. I.; Lee, J. H.; Andrade, J. D.; De Gennes, P. G., Protein—surface interactions in the presence of polyethylene oxide: I. Simplified theory. *Journal of Colloid and Interface Science* **1991,** *142* (1), 149-158.

19. Otsuka, H.; Nagasaki, Y.; Kataoka, K., Self-assembly of poly(ethylene glycol)-based block copolymers for biomedical applications. *Current Opinion in Colloid & Interface Science* **2001,** *6* (1), 3-10.

20. Kwon, G.; Naito, M.; Yokoyama, M.; Okano, T.; Sakurai, Y.; Kataoka, K., Micelles based on AB block copolymers of poly(ethylene oxide) and poly(.beta.-benzyl L-aspartate). *Langmuir* **1993,** *9* (4), 945-949.

21. Bader, H.; Ringsdorf, H.; Schmidt, B., Watersoluble polymers in medicine. *Die Angewandte Makromolekulare Chemie* **1984,** *123* (1), 457-485.

22. Yokoyama, M.; Inoue, S.; Kataoka, K.; Yui, N.; Okano, T.; Sakurai, Y., Molecular design for missile drug: Synthesis of adriamycin conjugated with immunoglobulin G using poly(ethylene glycol)-block-poly(aspartic acid) as intermediate carrier. *Die Makromolekulare Chemie* **1989,** *190* (9), 2041-2054.

23. Gref, R.; Minamitake, Y.; Peracchia, M. T.; Trubetskoy, V.; Torchilin, V.; Langer, R., Biodegradable long-circulating polymeric nanospheres. *Science* **1994,** *263* (5153), 1600-3.

24. Harada, A.; Kataoka, K., Formation of Polyion Complex Micelles in an Aqueous Milieu from a Pair of Oppositely-Charged Block Copolymers with Poly(ethylene glycol) Segments. *Macromolecules* **1995,** *28* (15), 5294-5299.

25. Kataoka, K.; Togawa, H.; Harada, A.; Yasugi, K.; Matsumoto, T.; Katayose, S., Spontaneous Formation of Polyion Complex Micelles with Narrow Distribution from Antisense Oligonucleotide and Cationic Block Copolymer in Physiological Saline. *Macromolecules* **1996,** *29* (26), 8556-8557.

26. Kabanov, A. V.; Bronich, T. K.; Kabanov, V. A.; Yu, K.; Eisenberg, A., Soluble Stoichiometric Complexes from Poly(N-ethyl-4-vinylpyridinium) Cations and

Poly(ethylene oxide)-block-polymethacrylate Anions. *Macromolecules* **1996,** *29* (21), 6797-6802.

27. Harada, A.; Kataoka, K., Chain length recognition: core-shell supramolecular assembly from oppositely charged block copolymers. *Science* **1999,** *283* (5398), 65-7.

28. Yokoyama, M.; Okano, T.; Sakurai, Y.; Suwa, S.; Kataoka, K., Introduction of cisplatin into polymeric micelle. *Journal of Controlled Release* **1996,** *39* (2), 351-356.

29. Nishiyama, N.; Yokoyama, M.; Aoyagi, T.; Okano, T.; Sakurai, Y.; Kataoka, K., Preparation and Characterization of Self-Assembled Polymer−Metal Complex Micelle from cis-Dichlorodiammineplatinum(II) and Poly(ethylene glycol)−Poly(α,β-aspartic acid) Block Copolymer in an Aqueous Medium. *Langmuir* **1999,** *15* (2), 377-383.

30. Kataoka, K.; Ishihara, A.; Harada, A.; Miyazaki, H., Effect of the Secondary Structure of Poly(l-lysine) Segments on the Micellization in Aqueous Milieu of Poly(ethylene glycol)−Poly(l-lysine) Block Copolymer Partially Substituted with a Hydrocinnamoyl Group at the Nε-Position. *Macromolecules* **1998,** *31* (18), 6071-6076.

31. Matsumura, Y.; Maeda, H., A new concept for macromolecular therapeutics in cancer chemotherapy: mechanism of tumoritropic accumulation of proteins and the antitumor agent smancs. *Cancer Res* **1986,** *46* (12 Pt 1), 6387-92.

32. Kwon, G.; Suwa, S.; Yokoyama, M.; Okano, T.; Sakurai, Y.; Kataoka, K., Enhanced tumor accumulation and prolonged circulation times of micelle-forming poly (ethylene oxide-aspartate) block copolymer-adriamycin conjugates. *Journal of Controlled Release* **1994,** *29* (1), 17-23.

33. Chauhan, V. P.; Jain, R. K., Strategies for advancing cancer nanomedicine. *Nat Mater* **2013,** *12* (11), 958-62.

34. Cabral, H.; Matsumoto, Y.; Mizuno, K.; Chen, Q.; Murakami, M.; Kimura, M.;

Terada, Y.; Kano, M. R.; Miyazono, K.; Uesaka, M.; Nishiyama, N.; Kataoka, K., Accumulation of sub-100 nm polymeric micelles in poorly permeable tumours depends on size. *Nat Nanotechnol* **2011,** *6* (12), 815-23.

35. Allen, T. M., Ligand-targeted therapeutics in anticancer therapy. *Nat Rev Cancer* **2002,** *2* (10), 750-63.

36. Bertrand, N.; Wu, J.; Xu, X.; Kamaly, N.; Farokhzad, O. C., Cancer nanotechnology: the impact of passive and active targeting in the era of modern cancer biology. *Adv Drug Deliv Rev* **2014,** *66*, 2-25.

37. Miura, Y.; Takenaka, T.; Toh, K.; Wu, S.; Nishihara, H.; Kano, M. R.; Ino, Y.; Nomoto, T.; Matsumoto, Y.; Koyama, H.; Cabral, H.; Nishiyama, N.; Kataoka, K., Cyclic RGD-linked polymeric micelles for targeted delivery of platinum anticancer drugs to glioblastoma through the blood-brain tumor barrier. *ACS Nano* **2013,** *7* (10), 8583-92.

38. Suzuki, K.; Miura, Y.; Mochida, Y.; Miyazaki, T.; Toh, K.; Anraku, Y.; Melo, V.; Liu, X.; Ishii, T.; Nagano, O.; Saya, H.; Cabral, H.; Kataoka, K., Glucose transporter 1-mediated vascular translocation of nanomedicines enhances accumulation and efficacy in solid tumors. *J Control Release* **2019,** *301*, 28-41.

39. Quader, S.; Liu, X.; Chen, Y.; Mi, P.; Chida, T.; Ishii, T.; Miura, Y.; Nishiyama, N.; Cabral, H.; Kataoka, K., cRGD peptide-installed epirubicin-loaded polymeric micelles for effective targeted therapy against brain tumors. *J Control Release* **2017,** *258*, 56-66.

40. Deshayes, S.; Cabral, H.; Ishii, T.; Miura, Y.; Kobayashi, S.; Yamashita, T.; Matsumoto, A.; Miyahara, Y.; Nishiyama, N.; Kataoka, K., Phenylboronic acid-installed polymeric micelles for targeting sialylated epitopes in solid tumors. *J Am Chem Soc* **2013,** *135* (41), 15501-7.

41. Oyewumi, M. O.; Yokel, R. A.; Jay, M.; Coakley, T.; Mumper, R. J., Comparison of cell uptake, biodistribution and tumor retention of folate-coated and PEG-coated gadolinium nanoparticles in tumor-bearing mice. *J Control Release* **2004,** *95* (3), 613-26.

42. Xiong, X. B.; Lavasanifar, A., Traceable multifunctional micellar nanocarriers for cancer-targeted co-delivery of MDR-1 siRNA and doxorubicin. *ACS Nano* **2011,** *5* (6), 5202-13.

43. Mi, P.; Cabral, H.; Kataoka, K., Ligand-Installed Nanocarriers toward Precision Therapy. *Adv Mater* **2020,** *32* (13), e1902604.

44. Obermeier, B.; Daneman, R.; Ransohoff, R. M., Development, maintenance and disruption of the blood-brain barrier. *Nat Med* **2013,** *19* (12), 1584-96.

45. Sweeney, M. D.; Sagare, A. P.; Zlokovic, B. V., Blood-brain barrier breakdown in Alzheimer disease and other neurodegenerative disorders. *Nat Rev Neurol* **2018,** *14* (3), 133-150.

46. Wiley, D. T.; Webster, P.; Gale, A.; Davis, M. E., Transcytosis and brain uptake of transferrin-containing nanoparticles by tuning avidity to transferrin receptor. *Proc Natl Acad Sci U S A* **2013,** *110* (21), 8662-7.

47. Jiang, Y.; Yang, W.; Zhang, J.; Meng, F.; Zhong, Z., Protein Toxin Chaperoned by LRP-1-Targeted Virus-Mimicking Vesicles Induces High-Efficiency Glioblastoma Therapy In Vivo. *Adv Mater* **2018,** *30* (30), e1800316.

48. Sarisozen, C.; Dhokai, S.; Tsikudo, E. G.; Luther, E.; Rachman, I. M.; Torchilin, V. P., Nanomedicine based curcumin and doxorubicin combination treatment of glioblastoma with scFv-targeted micelles: In vitro evaluation on 2D and 3D tumor models. *Eur J Pharm Biopharm* **2016,** *108*, 54-67.

49. Kou, L.; Bhutia, Y. D.; Yao, Q.; He, Z.; Sun, J.; Ganapathy, V., Transporter-

Guided Delivery of Nanoparticles to Improve Drug Permeation across Cellular Barriers and Drug Exposure to Selective Cell Types. *Front Pharmacol* **2018,** *9*, 27.

50. Shao, K.; Ding, N.; Huang, S.; Ren, S.; Zhang, Y.; Kuang, Y.; Guo, Y.; Ma, H.; An, S.; Li, Y.; Jiang, C., Smart nanodevice combined tumor-specific vector with cellular microenvironment-triggered property for highly effective antiglioma therapy. *ACS Nano* **2014,** *8* (2), 1191-203.

51. Yi, Y.; Kim, H. J.; Zheng, M.; Mi, P.; Naito, M.; Kim, B. S.; Min, H. S.; Hayashi, K.; Perche, F.; Toh, K.; Liu, X.; Mochida, Y.; Kinoh, H.; Cabral, H.; Miyata, K.; Kataoka, K., Glucose-linked sub-50-nm unimer polyion complex-assembled gold nanoparticles for targeted siRNA delivery to glucose transporter 1-overexpressing breast cancer stem-like cells. *J Control Release* **2019,** *295*, 268-277.

52. Patching, S. G., Glucose Transporters at the Blood-Brain Barrier: Function, Regulation and Gateways for Drug Delivery. *Mol Neurobiol* **2017,** *54* (2), 1046-1077.

53. Anraku, Y.; Kuwahara, H.; Fukusato, Y.; Mizoguchi, A.; Ishii, T.; Nitta, K.; Matsumoto, Y.; Toh, K.; Miyata, K.; Uchida, S.; Nishina, K.; Osada, K.; Itaka, K.; Nishiyama, N.; Mizusawa, H.; Yamasoba, T.; Yokota, T.; Kataoka, K., Glycaemic control boosts glucosylated nanocarrier crossing the BBB into the brain. *Nat Commun* **2017,** *8* (1), 1001.

54. Xie, J.; Gonzalez-Carter, D.; Tockary, T. A.; Nakamura, N.; Xue, Y.; Nakakido, M.; Akiba, H.; Dirisala, A.; Liu, X.; Toh, K.; Yang, T.; Wang, Z.; Fukushima, S.; Li, J.; Quader, S.; Tsumoto, K.; Yokota, T.; Anraku, Y.; Kataoka, K., Dual-Sensitive Nanomicelles Enhancing Systemic Delivery of Therapeutically Active Antibodies Specifically into the Brain. *ACS Nano* **2020,** *14* (6), 6729-6742.

55. Min, H. S.; Kim, H. J.; Naito, M.; Ogura, S.; Toh, K.; Hayashi, K.; Kim, B. S.;

Fukushima, S.; Anraku, Y.; Miyata, K.; Kataoka, K., Systemic Brain Delivery of Antisense Oligonucleotides across the Blood-Brain Barrier with a Glucose-Coated Polymeric Nanocarrier. *Angew Chem Int Ed Engl* **2020,** *59* (21), 8173-8180.

56. Mammen, M.; Choi, S. K.; Whitesides, G. M., Polyvalent Interactions in Biological Systems: Implications for Design and Use of Multivalent Ligands and Inhibitors. *Angew Chem Int Ed Engl* **1998,** *37* (20), 2754-2794.

57. Barnett, J. E.; Holman, G. D.; Munday, K. A., Structural requirements for binding to the sugar-transport system of the human erythrocyte. *Biochem J* **1973,** *131* (2), 211-21.

58. Otsuka, H.; Nagasaki, Y.; Kataoka, K., Characterization of aldehyde-PEG tethered surfaces: influence of PEG chain length on the specific biorecognition. *Langmuir* **2004,** *20* (26), 11285-7.

59. Ishii, T.; Miyata, K.; Anraku, Y.; Naito, M.; Yi, Y.; Jinbo, T.; Takae, S.; Fukusato, Y.; Hori, M.; Osada, K.; Kataoka, K., Enhanced target recognition of nanoparticles by cocktail PEGylation with chains of varying lengths. *Chemical Communications* **2016,** *52* (7), 1517-1519.

60. Sutton, D.; Nasongkla, N.; Blanco, E.; Gao, J., Functionalized micellar systems for cancer targeted drug delivery. *Pharm Res* **2007,** *24* (6), 1029-46.

61. Chen, C. C.; Dormidontova, E. E., Architectural and structural optimization of the protective polymer layer for enhanced targeting. *Langmuir* **2005,** *21* (12), 5605-15.

62. Uchida, K.; Otsuka, H.; Kaneko, M.; Kataoka, K.; Nagasaki, Y., A Reactive Poly(ethylene glycol) Layer To Achieve Specific Surface Plasmon Resonance Sensing with a High S/N Ratio: The Substantial Role of a Short Underbrushed PEG Layer in Minimizing Nonspecific Adsorption. *Analytical Chemistry* **2005,** *77* (4), 1075-1080.

63. Pearson, R. M.; Sen, S.; Hsu, H. J.; Pasko, M.; Gaske, M.; Kral, P.; Hong, S., Tuning the Selectivity of Dendron Micelles Through Variations of the Poly(ethylene glycol) Corona. *ACS Nano* **2016,** *10* (7), 6905-14.

64. Pannuzzo, M.; Esposito, S.; Wu, L. P.; Key, J.; Aryal, S.; Celia, C.; di Marzio, L.; Moghimi, S. M.; Decuzzi, P., Overcoming Nanoparticle-Mediated Complement Activation by Surface PEG Pairing. *Nano Lett* **2020,** *20* (6), 4312-4321.

65. Zhu, G.; Huang, Z.; Xu, Z.; Yan, L. T., Tailoring Interfacial Nanoparticle Organization through Entropy. *Acc Chem Res* **2018,** *51* (4), 900-909.

66. Chen, L. J.; Yang, H. B., Construction of Stimuli-Responsive Functional Materials via Hierarchical Self-Assembly Involving Coordination Interactions. *Acc Chem Res* **2018,** *51* (11), 2699-2710.

67. Li, F.; Lu, J.; Kong, X.; Hyeon, T.; Ling, D., Dynamic Nanoparticle Assemblies for Biomedical Applications. *Adv Mater* **2017,** *29* (14).

68. Magana, J. R.; Sproncken, C. C. M.; Voets, I. K., On Complex Coacervate Core Micelles: Structure-Function Perspectives. *Polymers (Basel)* **2020,** *12* (9).

69. Palivan, C. G.; Goers, R.; Najer, A.; Zhang, X.; Car, A.; Meier, W., Bioinspired polymer vesicles and membranes for biological and medical applications. *Chemical Society Reviews* **2016,** *45* (2), 377-411.

70. Ge, Z.; Liu, S., Functional block copolymer assemblies responsive to tumor and intracellular microenvironments for site-specific drug delivery and enhanced imaging performance. *Chem Soc Rev* **2013,** *42* (17), 7289-325.

71. Godoy-Gallardo, M.; York-Duran, M. J.; Hosta-Rigau, L., Recent Progress in Micro/Nanoreactors toward the Creation of Artificial Organelles. *Adv Healthc Mater* **2018,** *7* (5).

72. McQuigg, D. W.; Kaplan, J. I.; Dubin, P. L., Critical conditions for the binding of polyelectrolytes to small oppositely charged micelles. *The Journal of Physical Chemistry* **1992,** *96* (4), 1973-1978.

73. Wang, Y.; Kimura, K.; Huang, Q.; Dubin, P. L.; Jaeger, W., Effects of Salt on Polyelectrolyte−Micelle Coacervation. *Macromolecules* **1999,** *32* (21), 7128-7134.

74. Chen, J.-X.; Wang, M.; Tian, H.-H.; Chen, J.-H., Hyaluronic acid and polyethylenimine self-assembled polyion complexes as pH-sensitive drug carrier for cancer therapy. *Colloids and Surfaces B: Biointerfaces* **2015,** *134*, 81-87.

75. Harada, A.; Kataoka, K., Effect of Charged Segment Length on Physicochemical Properties of Core−Shell Type Polyion Complex Micelles from Block Ionomers. *Macromolecules* **2003,** *36* (13), 4995-5001.

76. Abe, K.; Ohno, H.; Tsuchida, E., Phase changes of polyion complex between poly(methacrylic acid) and a polycation carrying charges in the chain backbone. *Die Makromolekulare Chemie* **1977,** *178* (8), 2285-2293.

77. Mutaf, O. F.; Kishimura, A.; Mochida, Y.; Kim, A.; Kataoka, K., Induction of Secondary Structure through Micellization of an Oppositely Charged Pair of Homochiral Block- and Homopolypeptides in an Aqueous Medium. *Macromol Rapid Commun* **2015,** *36* (22), 1958-64.

78. Wibowo, A.; Osada, K.; Matsuda, H.; Anraku, Y.; Hirose, H.; Kishimura, A.; Kataoka, K., Morphology Control in Water of Polyion Complex Nanoarchitectures of Double-Hydrophilic Charged Block Copolymers through Composition Tuning and Thermal Treatment. *Macromolecules* **2014,** *47* (9), 3086-3092.

79. Anraku, Y.; Kishimura, A.; Oba, M.; Yamasaki, Y.; Kataoka, K., Spontaneous formation of nanosized unilamellar polyion complex vesicles with tunable size and

properties. *J Am Chem Soc* **2010,** *132* (5), 1631-6.

Chapter 2.

Effect of charge in the core of polymeric micelle on the performance in biological condition

2. 1. Introduction

We have been developing various types of PIC assemblies formed by block aniomers and block catiomers consisting of poly(ethylene glycol) (PEG) as a hydrophilic segment and polyamino acids as the charged blocks. These PIC assemblies have been effectively used as nanocarriers for drug and gene delivery[1]. The approach allows preparing a wide variety of PIC structures with nano- and micron-sized architectures by controlling the dimensional influence of the charged segment[2], the weight fraction of PEG[3] and the ionic strength[4]. Herein, we extended the understanding on PIC formation by focusing on the effect of the mixing charge ratio on the formation of core-shell PIC micelles (PIC/m) having PEG-catiomers and PEG-aniomers with fixed chemical structures. Thus, the structural changes of the micelles, and the accompanying *in vivo* behavior were assessed to determine the influence of the charge mixing ratio.

2. 2. Experimental Section

2. 2. 1. Materials

α-methoxy-ω-amino poly(ethylene glycol) (MeO-PEG-NH_2) (M_n = 2,000; M_w/M_n = 1.05) was purchased from Nippon Oil and Fats Co. Ltd. (Tokyo, Japan). β-benzyl-L-aspartate *N*-carboxyl-anhydride (BLA-NCA) was purchased from Chuo Kaseihin Co. Inc. (Tokyo, Japan). Dimethylformamide (DMF) and dichloromethane (DCM) were purchased from Kanto Chemical Co. Inc. (Tokyo, Japan). Hexane, ethyl acetate and deuterium oxide were purchased from Sigma Aldrich Japan Co. LLC (Tokyo, Japan). *N*-methyl-2-pyrrolidone (NMP) and D-PBS(-) were purchased from FUJIFILM Wako Pure Chemical Co. (Tokyo, Japan). 1,5-diaminopentane (DAP) and 1-ethyl-3-(3-dimethylaminopropyl) carbodiimide hydrochloride (EDC/HCl) were purchased from Tokyo Chemical Industry Co. Ltd.

(Tokyo, Japan). NMP and DAP were distilled over CaH_2 prior to use. Sulfo-cyanine 5 succinimidyl ester (sulfo-cy5-NHS ester) was purchased from Lumiprobe Co. (Hunt Valley, MD, USA). Dimethyl sulfoxide (DMSO) was purchased from Nacalai Tesque Inc. (Kyoto, Japan). Passive lysis buffer was purchased from Promega Co. (Madison, WI, USA). Isoflurane was purchased fron Abbott Japan Co. Ltd., Tokyo, Japan). eFuor450-conjugated CD31 (PECAM-1) monoclonal antibody was purchased from Thermo Scientific (Waltham, MA, USA). Balb/c mice (female; 5 weeks old) were purchased from Charles River Laboratories Japan (Kanagawa, Japan). All the animal experiments were performed according to the Guidelines for the Care and Use of Laboratory Animals, as stated by The University of Tokyo (Tokyo, Japan) and iCONM (Innovation Center of NanoMedicine, Kawasaki, Japan).

2. 2. 2. Polymer characterization

The degree of polymerization (DP) was determined by proton nuclear magnetic resonance (^{1}H-NMR) spectroscopy using JEOL ECS400 (JEOL Ltd., Tokyo, Japan). The molecular weight distribution of block copolymers was verified gel permeation chromatography (GPC) using a high performance liquid chromatography (HPLC) system (JASCO, Tokyo, Japan) connected with a Superdex 200-10/300GL column (GE Healthcare, Chicago, IL, USA).

2. 2. 3. Synthesis of poly(ethylene glycol)-b-poly(β-benzyl-L-aspartate)

Poly(ethylene glycol)-poly(β-benzyl-L-aspartate) (PEG-PBLA) was polymerized by ring-opening polymerization of β-benzyl-L-aspartate *N*-carboxyl-anhydride (BLA-NCA) using the terminal primary amine group of α-methoxy-ω-amino

poly(ethylene glycol) (MeO-PEG-NH_2) (M_n = 2,000) as the initiator (**Scheme 2-1.**). Lyophilized MeO-PEG-NH_2 was dissolved in DCM firstly. BLA-NCA was dissolved in DMF and then mixed with DCM. The solution of MeO-PEG-NH_2 was subsequentially added to BLA-NCA solution. The reaction solution was stirred at 35 ℃ under an argon atmosphere for more than 3 days. After the completion of the reaction, the reaction mixture was reprecipitated with mixed solvent of hexane and ethyl acetate (3:2 v/v), followed by a filtration with 0.22 μm PVDF filter under reduced pressure.

The DP of BLA units was calculated to be 80 from the ^{1}H-NMR measurement by comparing the peak area ratio using the methylene protons of PEG as the reference peak.

2. 2. 4. Synthesis of poly(ethylene glycol)-b-poly(α, β- aspartic acid)

Poly(ethylene glycol)-b-poly(α, β- aspartic acid) (MeO-PEG-PAsp) was synthesized by deprotection of the benzyl ester groups of PEG-PBLA (**Scheme 2-2.**). PEG-PBLA was dissolved in 0.25 M NaOH (5 molar equivalent to benzyl group) and stirred at room temperature for 2 hours to hydrolyze the benzyl ester moiety. The reaction mixture was dialyzed against deionized water using a Specra/Por 1 dialysis membrane (Repligen, Waltham, MA, USA) [MWCO: 6,000 – 8,000 Da] for 2 days, and then lyophilized subsequently.

The DP of poly(aspartic acid) unit was calculated to be 80 from the ^{1}H-NMR measurement by comparing the peak area ratio using the methylene protons of PEG as the reference peak (**Figure 2-1.**). The GPC trace of the obtained MeO-PEG-PAsp was unimodal (**Figure 2-2.**).

2. 2. 5. Synthesis of poly(ethylene glycol)-b-poly([5-aminopenthyl]-α, β-aspartamide)

Poly(ethylene glycol)-b-poly([5-aminopenthyl]- α, β-aspartamide) (MeO-PEG-P(Asp-AP) was synthesized by the deprotection of the benzyl ester groups of MeO-PEG-PBLA by ester-amide exchange reaction (**Scheme 2-3.**). Firstly, lyophilized MeO-PEG-PBLA was dissolved in NMP. A mixture of NMP and DAP (100 molar equivalent to BLA moiety) was added to the solution, and then stirred at 12 ℃ for 1 hour respectively. The reaction solution was neutralized with 1 M HCl in ice bath. The resulting solution was dialyzed against 10 mM HCl for 1 day and subsequently against deionized water for 2 days using a Specra/Por 1 dialysis membrane [MWCO: 6,000 – 8,000 Da]. MeO-PEG-P(Asp-AP) was given as a chloride salt after the lyophilization.

The DP of P(Asp-AP) unit was calculated to be 76 from the ^{1}H-NMR measurement by comparing the peak area ratio using the methylene protons of PEG as the reference peak (**Figure 2-3.**). The GPC trace of the obtained MeO-PEG-P(Asp-AP) was nearly unimodal (**Figure 2-4.**).

2. 2. 6. Preparation of cy5-labeled block copolymer

MeO-PEG-P(Asp-AP) labeled with cy5 (MeO-PEG-P(Asp-AP)-cy5) was prepared by labeling the ω-terminal end of PEG-PBLA-NH_2 with sulfo-cy5-NHS ester and subsequent ester-amido exchanging of the benzyl ester moiety. Firstly, PEG-PBLA was dissolved in DMSO. The DMSO solution of sulfo-cy5-NHS ester (1 molar equivalent to PEG-PBLA) was added to the PEG-PBLA solution, followed by stirring at room temperature overnight. The resulting solution was reprecipitated with mixed solvent of hexane and ethyl acetate (3:2 v/v), followed by a filtration with 0.22 μm PVDF filter under reduced pressure. The obtained polymer was reacted according to the scheme described in the *section 2. 2. 5.*

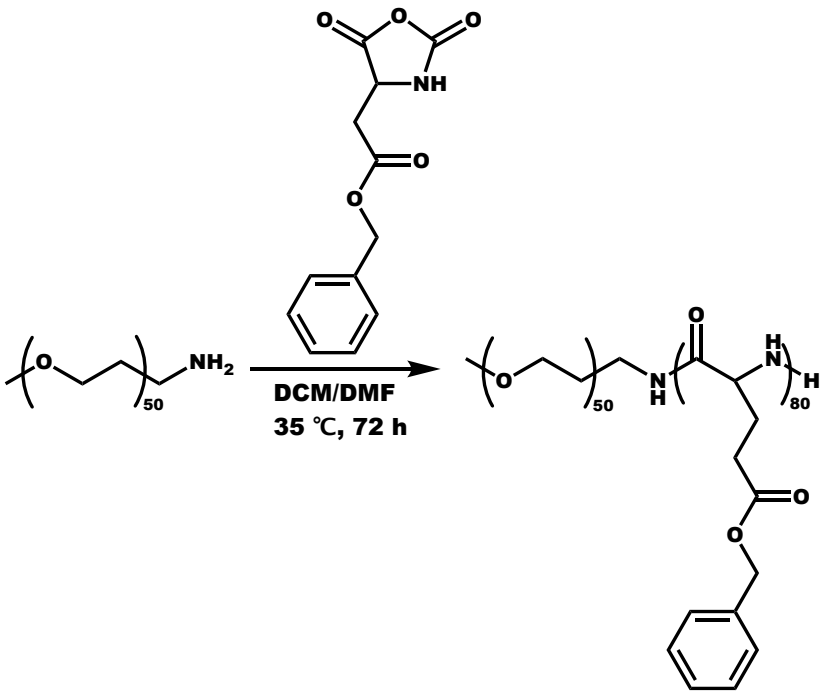

Scheme 2-1. Synthesis of MeO-PEG-PBLA

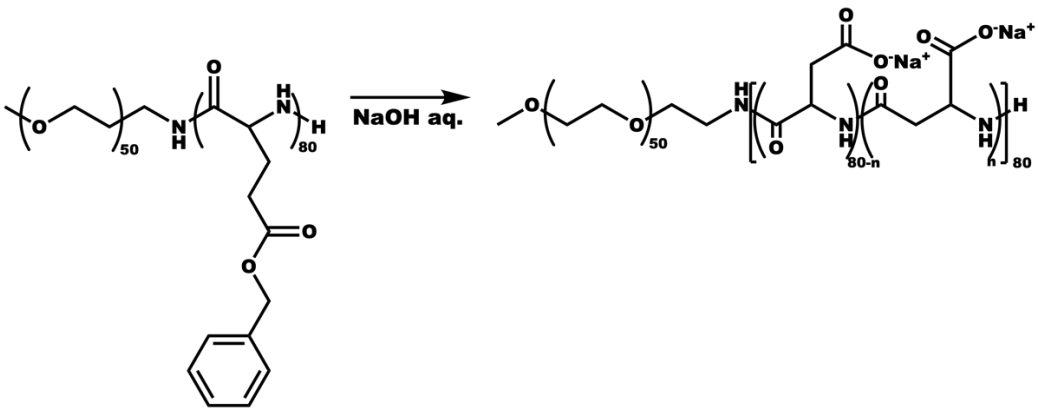

Scheme 2-2. Synthesis of MeO-PEG-PAsp

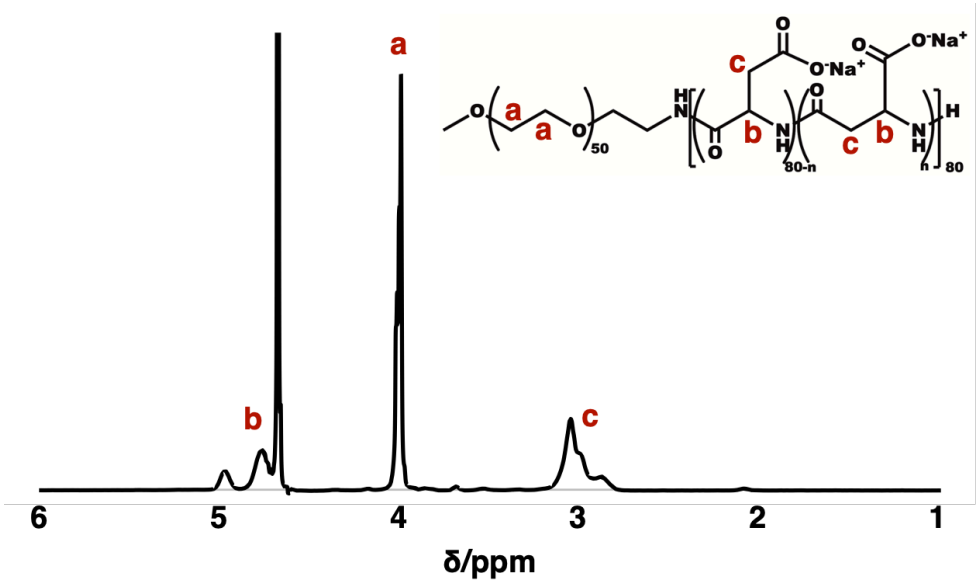

Figure 2-1. ^{1}H-NMR spectrum of MeO-PEG-PAsp (solvent: D_2O, temperature: 80 ℃)

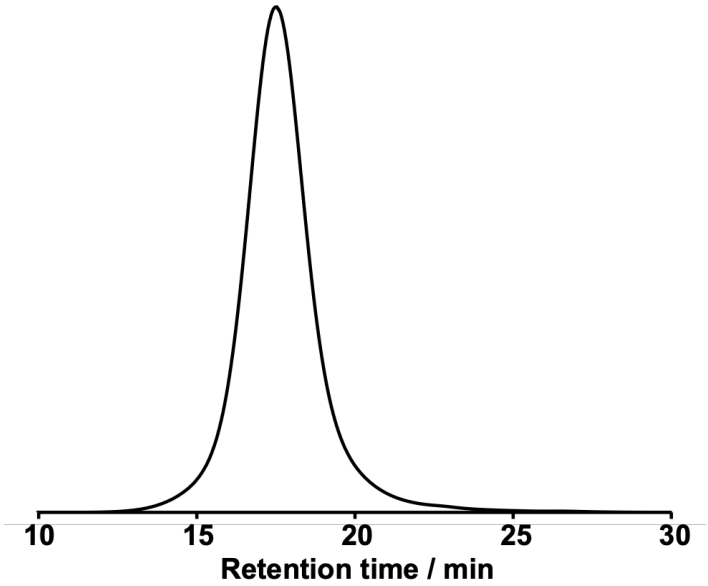

Figure 2-2. GPC chromatogram of MeO-PEG-PAsp (eluent: 10 mM PB (pH 7.4), 150 mM NaCl, detector: UV)

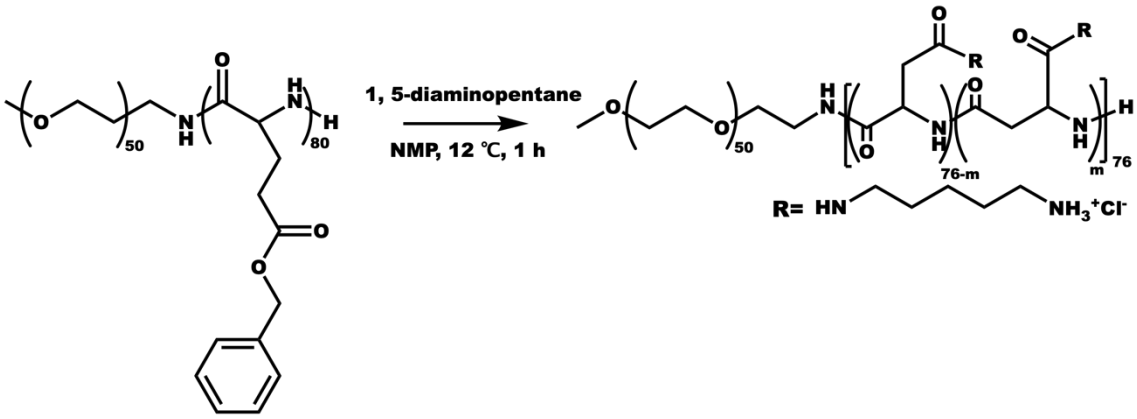

Scheme 2-3. Synthesis of MeO-PEG-P(Asp-AP)

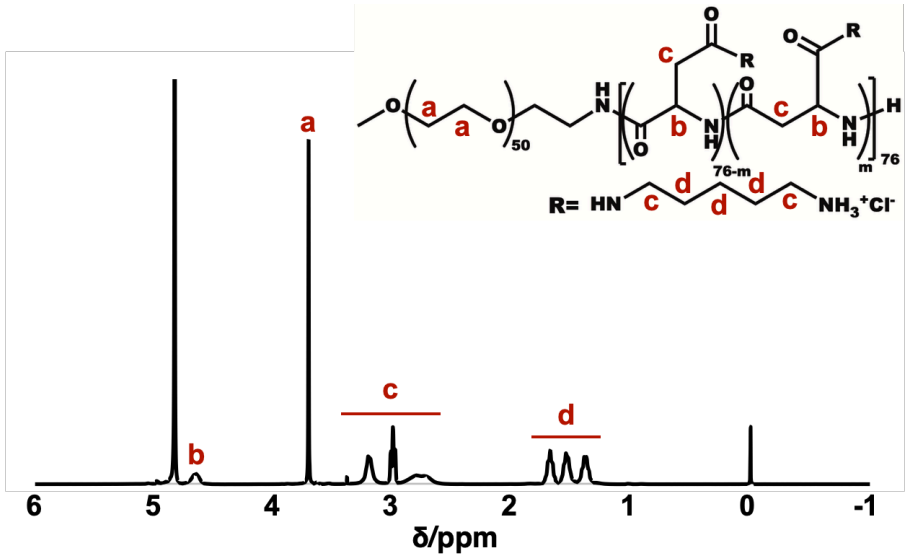

Figure 2-3. ^{1}H-NMR spectrum of MeO-PEG-P(Asp-AP) (solvent: D_2O, temperature: 25 ℃)

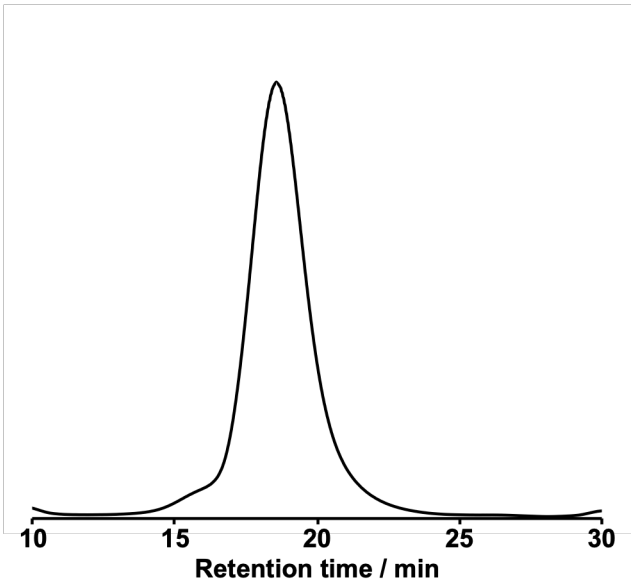

Figure 2-4. GPC chromatogram of MeO-PEG-P(Asp-AP) (eluent: 10 mM Acetic acid, 500 mM NaCl, detector: UV)

2. 2. 7. Preparation of polyion complex (PIC) micelle

MeO-PEG-PAsp, MeO-PEG-P(Asp-AP) (and MeO-PEG-P(Asp-AP)-cy5 for the preparation of cy5-labeled micelle) were dissolved in 10 mM phosphate buffer (PB, pH 7.4, 0 mM NaCl) separately to prepare a 1 mg/mL polymer solution and passed through a 0.22 μm membrane filter to remove dust particulates. These aniomer and catiomer solution were subjected to vortex-mixing at a residual molar ratio of amino groups to carboxyl groups in the side chains of each ionome with a range of $0.85 \leqq$ [carboxyl]/[amine] (C/A) $\leqq 1.15$. The mixed solution was vortexed (2,000 rpm, 2 minutes) to form polyion complex (PIC) micelle. The solution of EDC/HCl (10 molar equivalent to carboxyl units of MeO-PEG-PAsp) with a concentration of 10 mg/mL in 10 mM PB (pH 7.4, 0 mM NaCl) was added and subsequently reacted at room temperature overnight for cross-linking the PIC core. The residual EDC and block copolymers were

removed by the purification *via* ultrafiltration with VIVA SPIN 6 (Satrious stedium Biotech GmbH, Goettingen, Germany) [MWCO: 100,000 Da] (**Scheme 2-4.**). During the purification process, the solvent was replaced with deionized water (for transmission electron microscopy observation and static light scattering measurement), 10 mM PB (pH 7.4, 0 mM NaCl, for dynamic light scattering measurement and small angle X-ray scattering measurement), 10 mM deuterium PB (pD 7.0, 0 mM NaCl, for nuclear magnetic resonance measurement and Fourier transform infrared spectroscopy measurement) or D-PBS (-) (for animal experiment samples).

2. 2. 8. Dynamic light scattering measurement

The hydrodynamic diameter and corresponding of PIC micelles were investigated by conducting dynamic light scattering (DLS) measurement in 10 mM PB (pH 7.4, 0 mM NaCl) at 25 ℃ using a Zatasizer Nano ZS90 (Marvern Instruments Ltd., Worcestershire, UK) with a diode-pumped solid state laser (wavelength = 532 nm). The intensity averaged hydrodynamic diameter and polydispersity index (PdI) were derived from the cumulant method as described[4].

2. 2. 9. Electrophoretic light scattering measurement

The surface zeta potential of PIC micelles was evaluated by conducting electrophoretic light scattering (ELS) measurement using a Zatasizer Nano ZS90 equipped with a diope-pumped laser (532 nm) at room temperature. PIC micelle samples were prepared in 10 mM PB (pH 7.4, 0 mM NaCl) and 10 mM acetic acid buffer (pH 4.0, 0 mM NaCl), and then cross-linked and purified by ultrafiltration as described in the *section 2. 2. 7*.

2. 2. 10. Static light scattering measurement

The static light scattering (SLS) measurement was done using a DLS-8000 instrument (Otsuka Electronics, Osaka, Japan). Vertically polarized light with a wavelength of 633 nm from a He-Ne laser was used as the incident beam. All measurements were conducted at 25 ℃. The light scattered by a diluted polymer solution was expressed by the equation follows

$$\frac{Kc}{\Delta R(\theta)} = \frac{1}{M_W}\left(1 + \frac{1}{3}\langle {R_g}^2\rangle q^2 + \cdots\right) + 2A_2c + \cdots$$

where C is the concentration of polymer, ΔR(θ) is the difference between the Rayleigh ratio of the solution and that of the solvent, Mw is the apparent weight-average molecular weight, $<R_g^2>$ is the mean square radius of gyration, A2 is the second viral coefficient, and $K = \frac{4\pi^2 n^2 (dn/dc)^2}{N_A {\lambda_0}^4}$ (N_A is Avogadro's number). The known Rayleigh ratio of toluene was used as a standard for the calibration. The Zimm plots were made from the dependence of ΔR(θ) on detection angle (13 angles from 30 to 150° with intervals of 10°) and a series of concentrations (0.125, 0.25, 0.5, 1 and 2 mg/mL). The increments of refractive index, dn/dc, of the sample solutions were obtained using a DRM-3000 double beam differential refractometer (Otsuka Electronics, Osaka, Japan).

2. 2. 11. Transmission electron microscopy observation

The structural morphology of PIC micelles was evaluated using transmission electron microscopy (TEM) observation. Firstly, the copper grid surface with 400 mesh

was exposed to hydrophilic treatment by plasma irradiation under the condition of vacuum. Then, 2 μL of the sample solution prepared in deionized water was applied onto the surface of grid, subsequently visualized by dropping 2 μL of 2 wt% uranyl acetate in 50 v/v% ethanol solution, followed by drying at room temperature. TEM observations were conducted with a transmission electron microscope JEM-1400 (JEOL, Tokyo, Japan) operating at 120 kV acceleration voltage.

2. 2. 12. Size exclusion chromatography measurement

The size exclusion chromatography measurement was conducted for the purpose of evaluate the excess amount of block copolymers after PIC micelle formation and cross-linking by EDC coupling. The molecular weight distribution was verified gel permeation chromatography (GPC) using a high performance liquid chromatography (HPLC) system (JASCO, Tokyo, Japan) equipped with a Superdex 200-10/300GL column (GE Healthcare, Chicago, IL, USA). The column was eluted with 10 mM phosphate buffer (PB, pH 7.4) containing 500 mM NaCl at a flow rate of 0.75 mL/min at room temperature. PIC micelle samples were administrated to the system after cross-linked, before purified by ultrafiltration.

2. 2. 13. Proton nuclear magnetic resonance spectroscopy

PIC micelles were prepared in 10 mM deuterated phosphate buffer (PB, pD 7.0), and then ^{1}H-NMR measurement was conducted using JEOL ECS400 (JEOL Ltd., Tokyo, Japan) at room temperature. It has been reported that the peak intensity of poly(amino acid) protons appears lower than expected from the structure of building block

copolymers due to the restrained mobility of atoms by assembled into the core of micelles [5-7].

2. 2. 14. Fourier transform infrared spectroscopy

Cross-linking degree of PIC micelles was quantified by fourier transform infrared spectroscopy (FT-IR) measurement as previously described [8]. PIC micelles were prepared in 10 mM deuterated phosphate buffer (PB, pD 7.0) and concentrated to 5 mg/mL polymer concentration by ultrafiltration. FT-IR measurement was conducted using FT/IR-6300 (JASCO, Tokyo, Japan) connected to PS-4000 (JASCO). FT-IR spectra were obtained with 4 cm^{-1} spectral resolution and 64 scans. Resulting spectra were analyzed using Igor Pro 8 (Wave Metrics, Portland, OR, USA). Cross-linking degree was determined by calculating consumption of carboxyl groups by ratio of the PEG peak (1460 cm^{-1}, from scissoring and bending of C-H groups) to the carboxylic acid peak (1600 cm^{-1}, from anti-summetric stretching of $-COO^-$ groups) using the spectra of MeO-PEG-PAsp polymer as a reference of non-cross-linked material.

2. 2. 15. Small angle X-ray scattering measurement

To get further investigation about the structure of PIC micelle, small angle X-ray scattering (SAXS) measurement was carried out with 2 mg/mL micelle samples in 10 mM phosphate buffer (PB, pH 7.4, 0 mM NaCl). The measurement was performed using FR-X/BioSAXS-1000 (Rigaku, Tokyo, Japan) with a Cu Kα incident beam (λ = 1.54187 Å). The scattering vector (q) vs intensity (I(q)) curves (SAXS) profiles of 10 mM PB was subtracted from the SAXS profiles of PIC micelles. Obtained SAXS profile was linearly extrapolated to zero-angle scattering by the conventional Guinier approximation method.

The intersection at the regressed zero-angle scattering derives the radius of Gyration (R_g) according to the linearized equation:

$$\ln I(q) = \ln I(q) - \frac{{R_g}^2}{3} \cdot q^2$$

2. 2. 14. Biodistribution of PIC micelles

Balb/c mice (n = 3, female, 7 weeks old) were injected with 200 μL of 1 mg/mL cy5-labeled PIC micelles in D-PBS(-) from tail vein. And then, the mice were sacrificed 1, 6 and 24 hours after sample administration and the remaining blood was washed by perfusion with D-PBS(-). Blood was collected from the interior vena cava, heparinized and centrifuged to obtain plasma. The liver, kidneys, spleen, heart, lung and femoral muscle were excised, washed with D-PBS(-) and homogenized with cell lysis buffer using Multi Beads Shocker MBX (Yasui Kikai, Osaka, Japan). The accumulation rate of PIC micelle was evaluated by fluorescence intensity measurement using an Infinite M2000 Pro spectrophotometer (Tecan, Mannedorf, Switzerland).

2. 2. 16. Intravital real time laser scanning confocal microscopy observation

All the intravital observation were conducted using A1R confocal laser scanning microscope (Nikon Co., Tokyo, Japan) equipped with an upright Eclipse FN1 (Nikon Co.). The 200 μL of cy5-labeled PIC micelle in D-PBS(-) was administrated to mice (Balb/c, female, 7 weeks old) from tail vein under the anesthetized with 2.5 % isoflurane using a NARCOBIT-E Univentor 400 Anesthesia Unit (Natsume Seisakusho Co. Ltd., Tokyo, Japan), and then real-time observation was conducted continuously. The anesthetized mice were placed onto Thermoplate (Tokai Hit Co. Ltd., Shizuoka, Japan) with the temperature set 37 ℃. Cy5 was excited with a 640-nm laser and detected using

700-50-nm bandpass emission filter. A 20× objective lens was used for earlobe observation and 40× objective lens was used for liver observation. Obtained images were analyzed using NIS-Elements software (Nikon Co.).

The blood circulation profile of cy5-labeled PIC micelles was evaluated by quantifying the fluorescent intensity inside of the blood vessels in the earlobe for 30 minutes continuously after the intravenous administration of samples to the mice as previously described [9]. The fluorescent intensity in the region of interest (ROI) in the vein was measured, followed by the subtraction of the background fluorescent intensity in ROI before the sample administration. The intensity value was standardized with the maximum fluorescent intensity in ROI during the observation.

For the liver imaging, 10 μg of eFluor 450-comjugated PECAM-1 was intravenously injected to the mice 30 minutes before the PIC micelle administration in order to visualize sinusoidal walls by exciting eFuor 450 using a 405 nm laser and detecting 450/50-nm emission filter. Liver imaging was conducted for 2 hours after the intravenous sample injection.

2. 3. Results and discussion

2. 3. 1. Characterization of PIC micelle

PIC polymeric micelles were prepared by combination of block copolymer solutions in 10 mM phosphate buffer (0 mM NaCl, pH 7.4) with a concentration of 1 mg/mL, and then the characteristic features were identified by dynamic light scattering (DLS) measurement. Samples with mixing mol ratios of [carboxylate]/[amine] ([mol]/[mol], C/A) in the range from 0.85 to 1.15 resulted in narrow distributed micelles with 30-50 diameter (**Figure 2-5.**). The carboxylate and amine units of the charged

segments were cross-linked by 1-ehtyl-3-(3-dimethylamino-propyl) carbodiimide (EDC), followed by ultrafiltration to remove the excess EDC and free polymers. The surface Z-potential of each micelle was determined by electrophoretic light scattering (ELS) measurement. It has been reported that the surface potential of nanoparticles is attenuated after PEGylation due to steric effects of PEG chains[10-11]. In our case, the PIC micelles with excess amount of anionic-charged block copolymers showed decreasing Z-potential depending on the amount of additional carboxylate units regardless of PEGylation. On the other hand, the PIC micelles with excess cationic-charged block copolymers did not change the Z-potential so much (**Figure 2-6.**). This result is suggested to be independent from the ionization ratio of carboxylates and amines in buffer as the trend of Z-potential was similar in 10 mM acetate buffer (0 mM NaCl, pH 4.0). Thus, we hypothesized that the excess of carboxylate or amine units may have an effect to the structure of PIC micelles. Hence, the amount of block copolymers that do not participate in the micellar formation was quantified using size exclusion chromatography (SEC) before purification of micelles. As shown in Figure 1ef, PIC micelles were detected at 8.8 mL regardless of C/A in a range from 0.85 to 1.15, whereas the block copolymers that were not integrated in the micelles were only detected for C/A = 1.10 and C/A = 1.15 at elution volume of 15.2 mL (**Figure 2-7.**). Additionally, the ratio of the integration of the peak of block copolymers to that of PIC micelles was found to be larger for C/A = 1.15 than for C/A = 1.10. Thus, while the extra anionic-charged block copolymers were excluded from micelle formation, the excess cationic-charged block copolymers can participate in the formation of PIC micelles against unfavorable charge mismatching. These results propose the asymmetric micelle formation of anionic charged block copolymers and cationic charged ones. Note that MeO-PEG-P(Asp-AP) has the longer side chain in its cationic

charged segment comparing to the side chain in anionic charged segment of MeO-PEG-PAsp. Previously, it was reported that the polyion complex formation with the combination of PEG-polyanion (block aniomer) and homo-polycation (homo catiomer) was affected not only by the weight fraction of PEG but also the length of aliphatic side chain of the homo-polycation. The favorable PIC formation caused by the hydrophobic characteristic of long aliphatic side chain of homo-polycation was suggested[12]. Based on their findings, one plausible explanation of asymmetric micellar formation of oppositely charged block copolymers may be due to the higher hydrophobicity of the longer aliphatic side chain of MeO-PEG-P(Asp-AP) compared to MeO-PEG-PAsp.

To further understand the formation of the PIC micelles, we evaluated how C/A affected other structural characteristics. Thus, we first look into the association number of each PIC micelle was quantified by identifying molecular weight through static light scattering (SLS) to get more insight on their architecture. The association number of PIC micelles with stoichiometric charge balance (C/A = 1.0) was found to be 400 polymers, which is 4-fold higher than that of PIC micelles with C/A = 0.90, *i.e.* 97 polymers, and about twice higher than that of PIC micelles with C/A = 1.10, *i.e.* 177 polymers (**Figure 2-8.**). These results suggest that the PIC micelles may be forming different core-shell structures depending on C/A though the size distribution evaluated by DLS and morphology observed by TEM (**Figure 2-9.** and **Table 2-1.**) were comparable. Therefore, detailed structural features of the charged core of PIC micelles were investigated by ^{1}H-NMR and SAXS.

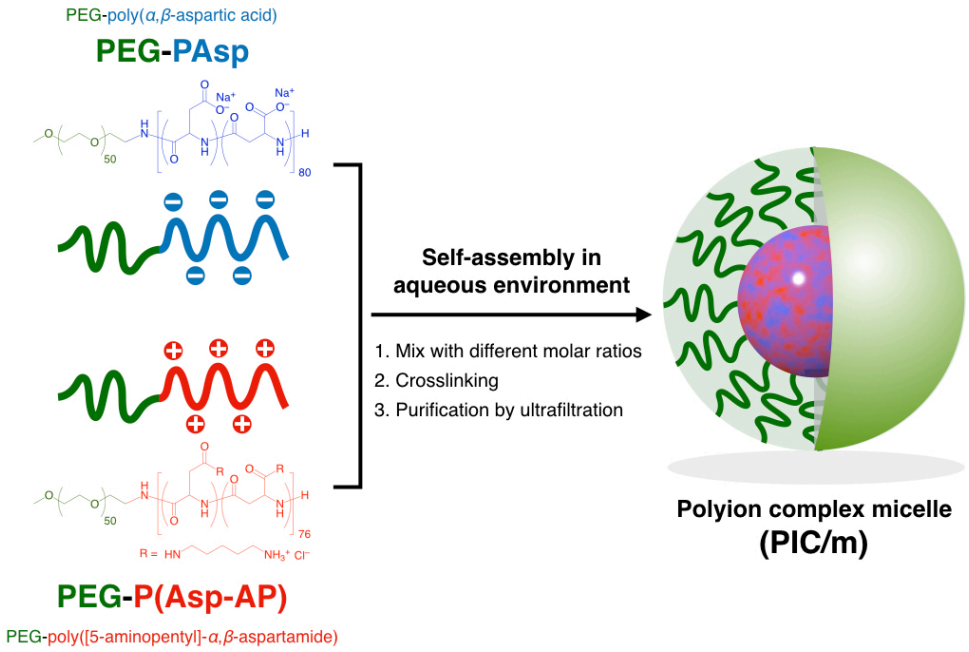

Scheme 2-4. Preparation of PIC/m consisted with the combination of oppositely charged block copolymers

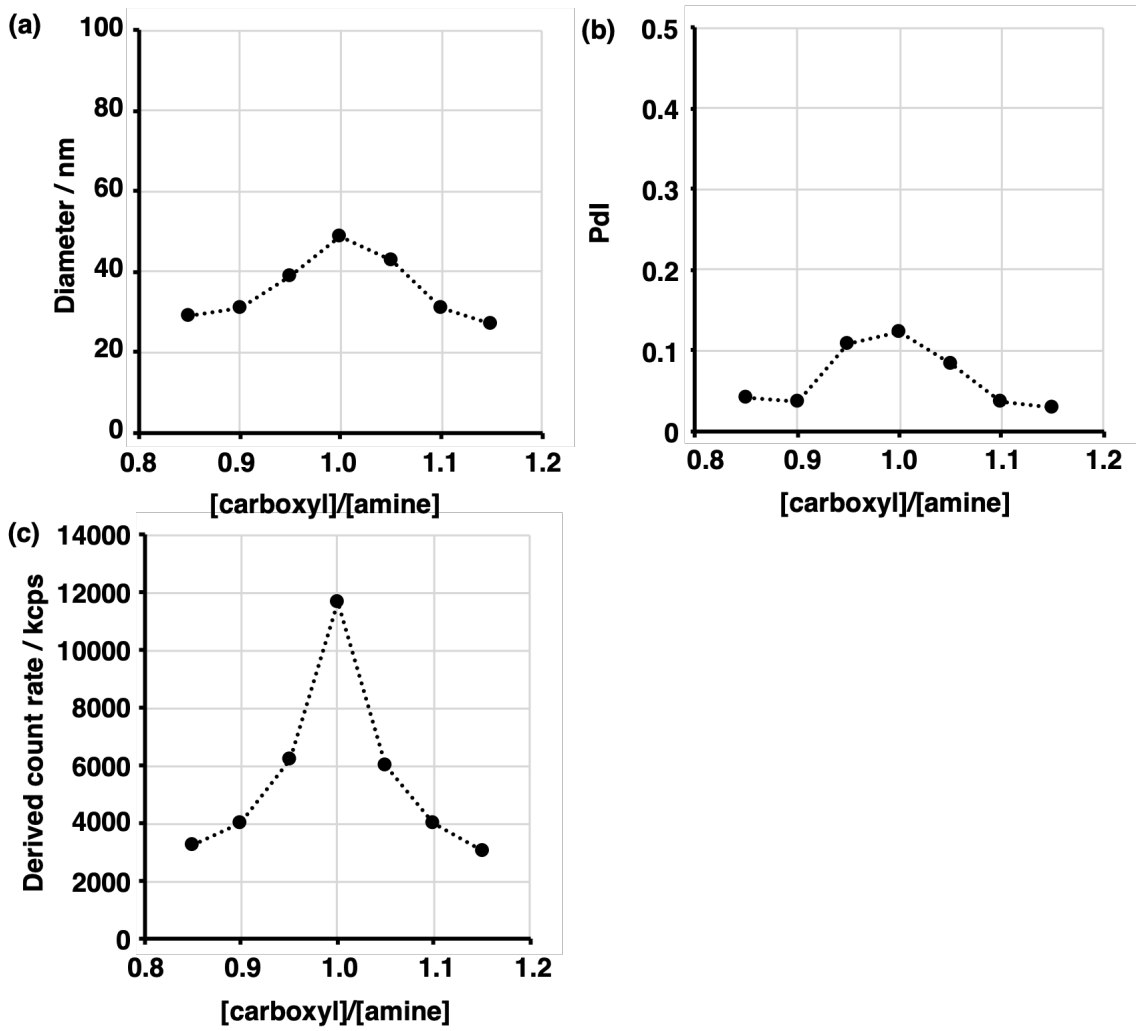

Figure 2-5. Structural characteristics of PIC micelles evaluated by DLS (a) cumulant diameter, (b) PdI and (c) derived count rate (1 mg/mL polymer concentration in 10 mM PB (pH 7.4, 0 mM NaCl), at room temperature)

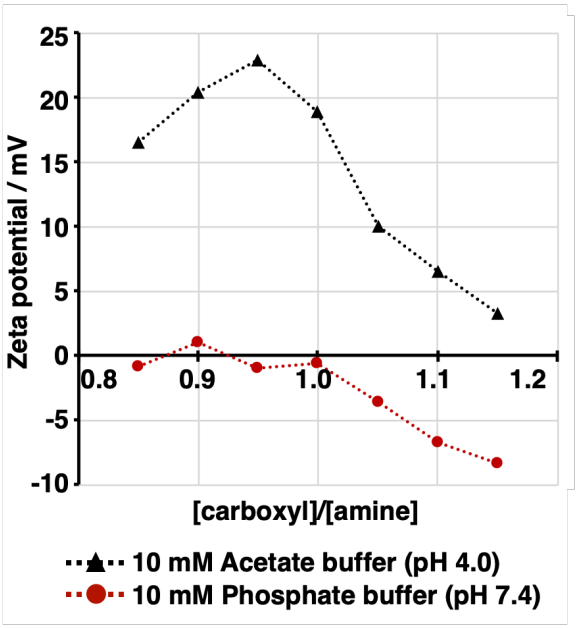

Figure 2-6. Surface zeta potential of PIC micelles measured by electrophoretic light scattering measurement at room temperature

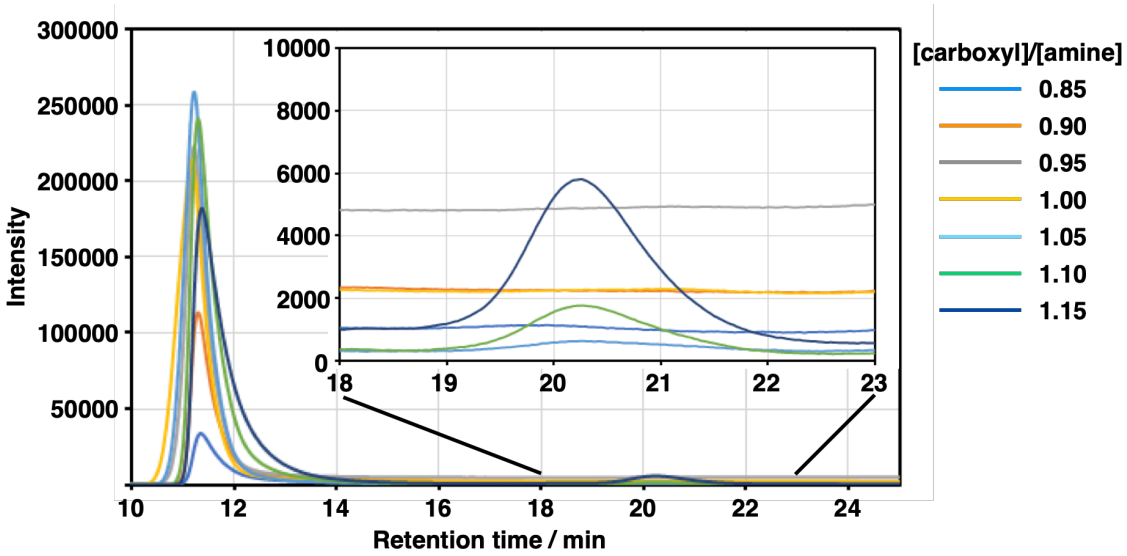

Figure 2-7. GPC spectra of PIC micelles before ultrafiltration (eluent: 10 mM PB (pH 7.4), 500 mM NaCl)

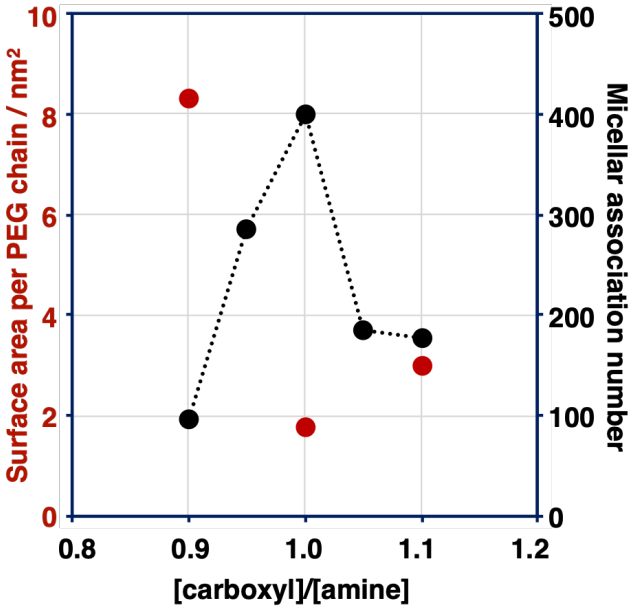

Figure 2-8. Micellar association number of PIC micelles quantified by SLS measurement and surface area per PEG chain calculated from the size of hydrophobic core observed by TEM imaging

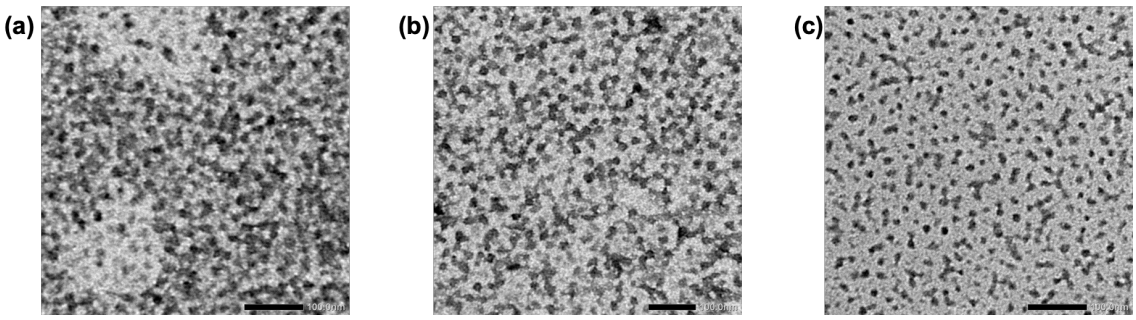

Figure 2-9. TEM observation of PIC micelle with [carboxyl]/[amine] = 0.90 (a), 1.00 (b) and 1.10 (c) (scale bar: 100 nm)

Table 2-1. Diameter of PIC hydrophobic core of PIC micelles observed by TEM (Analyzed using ImageJ FIJI, n = 250, means ± SD)

[carboxyl]/[amine]	0.90	1.00	1.10
Diameter / nm	16.3 ± 3.5	15.1 ± 2.7	13.4 ± 1.4

2. 3. 2. Investigation of structure of PIC micelle

PIC micelles are considered to be composed of a core (represented by the assembled charged part of the polymer) and a hydrophilic shell (represented by hydrophilic part of the polymer and surrounding water). Thus, the formation of micelles is expected to weaken the ^{1}H-NMR signals from protons located within the micellar core due to the restricted internal molecular motion. In fact, it has been reported that the peaks from protons of molecules encapsulated into the core of micelles showed significant decreased intensity[5-7]. Here, ^{1}H-NMR measurements were done with PIC micelles prepared in 10 mM deuterium phosphate buffer (0 mM NaCl, pD = 7.0). Cross-linking of the micelle core with EDC, and micelle purification were conducted as abovementioned. The peaks of protons in charged segment were detected from 1.0 to 1.9, from 2.4 to 3.2 and from 4.3 to 4.6 ppm. The intensities of these peaks were normalized with that of the peaks of protons in poly(ethylene glycol) segment appearing from 3.4 to 3.7 ppm (**Figure 2-10.**). The normalized intensities of peaks attributed to the charged segments decreased when C/A increased from 0.85 to 1.15 (**Figure 2-11.**). Note that this result is consistent with FT-IR measurement result, which suggests that consumption rate of carboxyl groups increases depending on the increased C/A. Cross-linking rate could not be calculated by the obtained FT-IR spectra because the peak shift of amine groups and carboxyl groups and overlapping with PEG peaks and amide peaks were observed. These peak shifts

indicated the changing of molecular states by encapsulating inside the core. (**Figure 2-12, Table 2-2**.). Hence, while PIC micelles having C/A above 1.0 may present compartmentalized core-shell structure with low integration values, the PIC micelles with excess cationic-charged block copolymers may lose the well-separated phases, as the protons in charged segment maintain the inter-molecular mobility.

Based on the ^{1}H-NMR observations, we hypothesized that the core-shell structure was not obtained when the PIC micelles formed against stoichiometric charge matching. To demonstrate this point, the micelles were investigated by small angle X-ray scattering (SAXS) measurement, which provides structural information at nanometer resolution by evaluating the distribution of electrons in micelles and the surrounding medium. The structures of the PIC micelles were calculated from the scattering pattern based on the difference of scattering length densities of the core, the shell and the media. The radius of gyration (R_g) of the PIC micelle was obtained from SAXS data fitted by the Guinier approximation (**Figure 2-13.)**. The ratio of R_g and R_h (hydrodynamic radius obtained from DLS measurement) provides insights about the particle compactness and shape. The calculated ratio of R_g to R_h (R_g/R_h) suggested spherical conformation for PIC micelles prepared with C/A from 0.90 to 1.05 (**Table 2-2.**). It is worth noting that the calculated R_g of PIC micelles with larger carboxylate molar ratio to amine (C/A = 1.10) was 1.00, corresponding to a uniform phase sphere[13]. This result is consistent with the SEC analysis of the micelles, which indicate that the PIC core cannot include excess anionic-charged segments, leading to uniform micelle assembly.

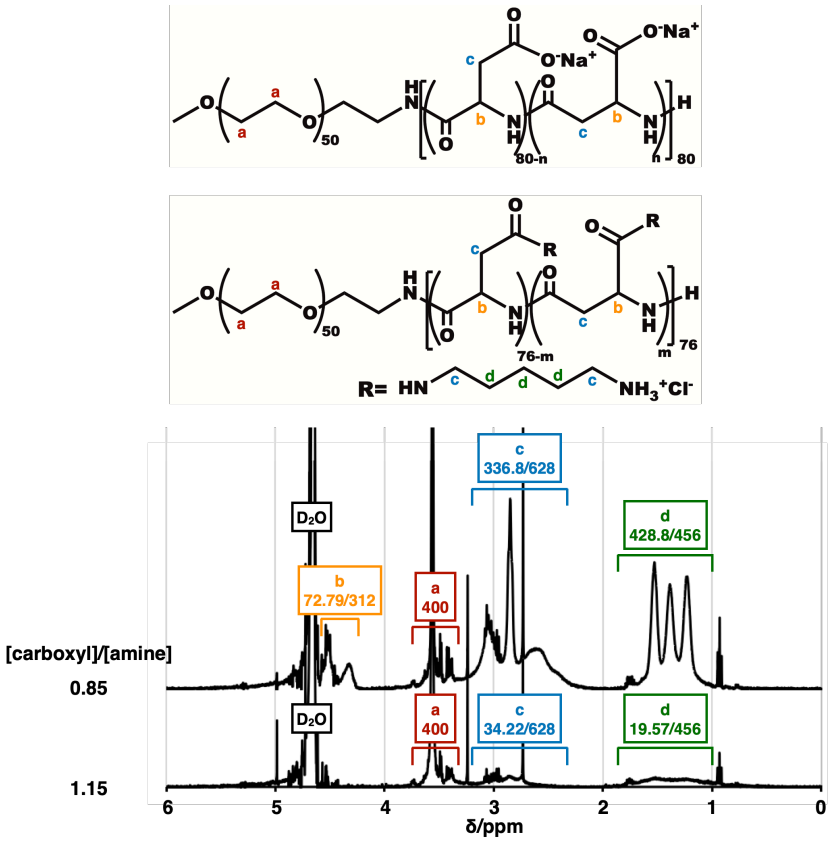

Figure 2-10. ^{1}H-NMR spectra of PIC micelle ([carboxyl]/[amine] = 0.85 and 1.15)

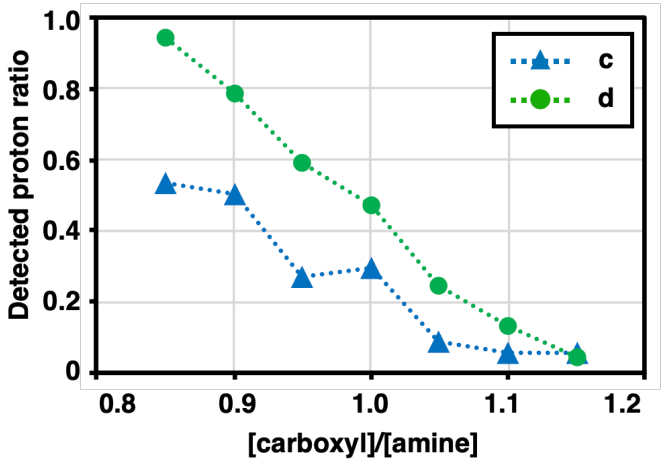

Figure 2-11. Detected proton (c and d in **Figure 2-10.**) ratio of PIC micelles to building block copolymers

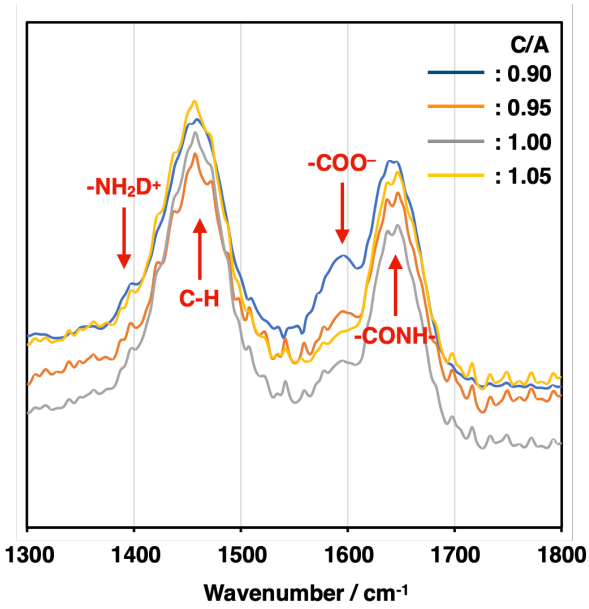

Figure 2-12. FT-IR spectra of PIC/m with varying C/A. crosslinking degrees of samples were determined by calculating consumption of -COO^- groups by the ratio of the PEG peak (1460 cm^{-1}, from scissoring and bending of C-H groups) to the carboxylic acid peak (1600 cm^{-1}, from anti-symmetric stretching of -COO^- groups)

Table 2-2. Calculated peak area ratio of FT-IR spectra. Peaks were compared to the peak of PEG peak (1460 cm^{-1} of **Figure 2-12.**) as a reference.

C/A	-COO^-	-CONH-	-NH_2D^+
0.90	0.25	0.82	0.033
0.95	0.13	0.97	0.068
1.00	0.045	0.65	-
1.05	0.020	0.78	-

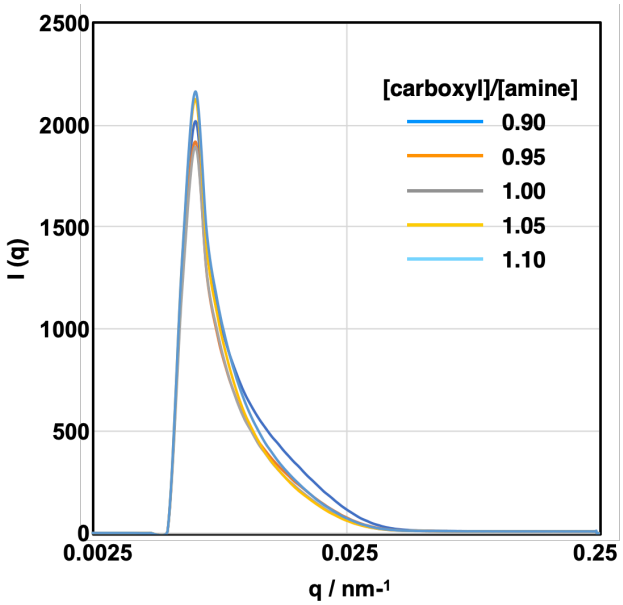

Figure 2-13. Scattering vector (q) vs intensity (I(q)) SAXS profiles of PIC micelles

Table 2-3. Radius of Gyration (R_g) evaluated from SAXS measurement, hydrophilic radius (R_h) quantified with DLS and calculated R_g/R_h

C/A	0.90	0.95	1.00	1.05	1.10
R_g / nm	9.0	9.7	12	15	16
R_h / nm	16	20	25	22	16
R_g/R_h	0.58	0.50	0.51	0.69	1.0

Table 2-4. Density of PEG chains and ions in the core of PIC micelles at a different C/A calculated from the micellar association number measured by SLS and R_g measured by SAXS

C/A	0.90	0.95	1.00	1.05
PEG / nm^{-2}	0.095	0.24	0.22	0.065
carboxyl / nm^{-3}	1.2	2.8	2.2	0.52
amine / nm^{-3}	1.3	3.0	2.2	0.50
total ions / nm^{-3}	2.5	5.8	4.4	1.0

2. 3. 3. Biodistribution of PIC micelle

Finally, we evaluated the stability of PIC micelles in the bloodstream, and their distribution in the organs of mice, which are significant features for applying PIC micelles as nanocarriers. Cy5-labeled PIC micelles were prepared by conjugating fluorescent molecules to the ω-end of cationic-charged block copolymers. The Cy5-labeled PIC micelles were intravenously injected to mice, and the fluorescent intensity in the vein was continuously monitored by intravital real-time confocal laser scanning microscopy (IVRT-CLSM). PIC micelles with C/A ≦ 1.00 disappeared from the bloodstream almost immediately after the administration, and only 10 % of the injected dose was detectable 1 h after administration. On the other hand, 90 % of injected PIC micelle circulated in the bloodstream stably when C/A was 1.05 and 1.10 (**Figure 2-13.**). These results confirmed that the excess amount of amine unit in the core of PIC micelle decreases the blood circulation of nanoparticles. The organ distribution of the PIC micelles was evaluated at 1-, 6- and 24-h after intravenous injection by quantifying the fluorescent intensity of each

collected organ after homogenization (**Figure 2-14.** and **Figure 2-15.**). PIC micelles remaining in the bloodstream were removed by perfusing with D-PBS (-) from hepatic portal vein before collecting organs. Liver accumulation rate of PIC micelle at a C/A ≤ 1.05 was correlated with the ion density in the core of micelles not PEG chain density (**Table 2-4.**). It is suggested that the lower ion density in the core of PIC micelle induces higher liver accumulation of it. Note that the PIC micelle at a C/A of 1.10 shows less than 10 % of liver accumulation while more than 50 % of PIC micelle at a C/A of ≤ 1.05 accumulates to the liver. The negatively charged surface potential of PIC at a C/A of 1.10 reduces the organ accumulation and prolongs the blood circulation. Furthermore, R_g quantified by SAXS measurement indicates deficient phase separation of between PEG segments and oppositely charged segments because R_g/R_h calculated to be 1.0. For these results, more extended distribution of charged segments in PIC micelle at a C/A of 1.10 compared to PIC micelle at a C/A ≤ 1.05 could be inferred.

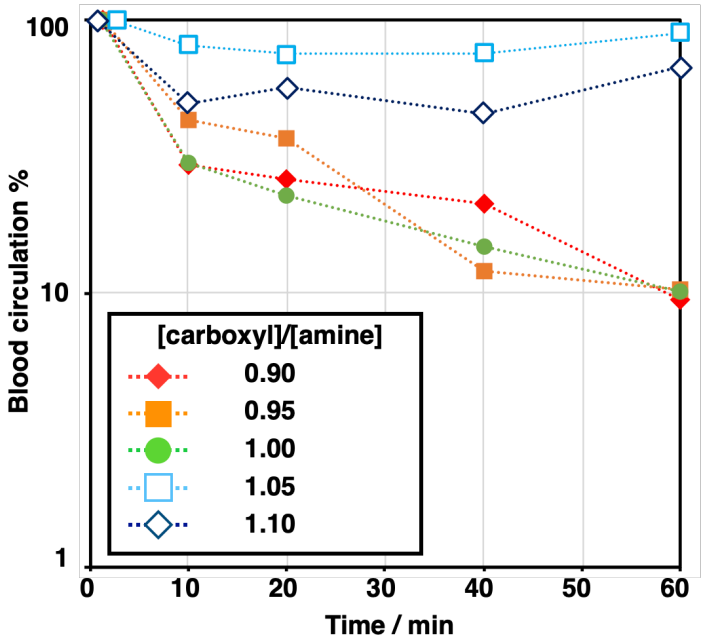

Figure 2-13. Blood circulation profiles of PIC micelle observed using IVRT-CLSM

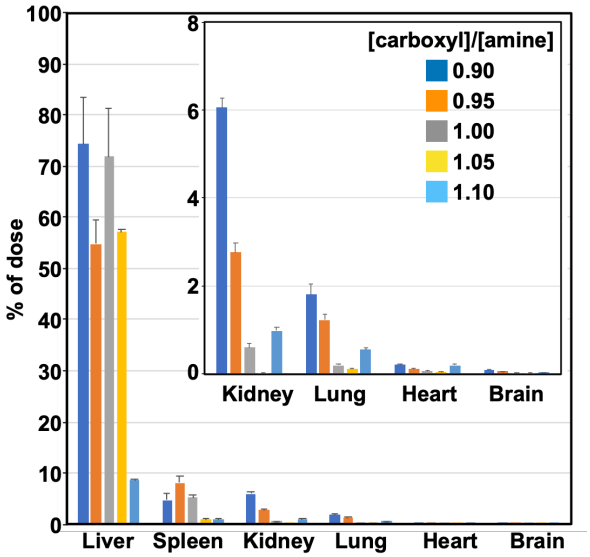

Figure 2-14. Biodistribution of PIC micelles 24 hours after the intravenous administration (n = 3, means ± SE)

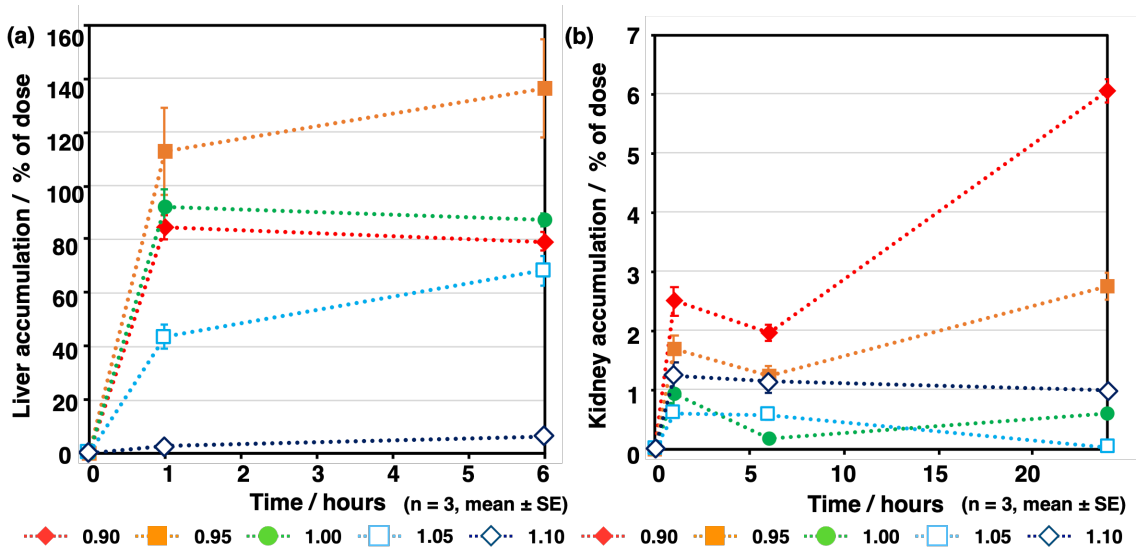

Figure 2-15. Time course of PIC micelle accumulation to (a) liver and (b) kidney (n = 3, means ± SE)

2. 3. 4. Observation of PIC micelles accumulated to the liver

As PIC/m with C/A from 0.90 to 1.00 showed highest accumulation in liver, the microdistribution of Cy5-PIC/m in liver was examined in real-time by intravital microscopy. For direct observation, the liver was surgically exposed and glued directly to the cover glass using a drop of oil [14]. Endothelial cells (the liver sinusoidal wall) were stained by i.v. injection of eFluor450-PECAM-1 at 30 min before starting IVRT-CLSM observation. PIC/m with C/A of 1.10 showed high fluorescence signal derived from PIC/m in intravascular lumen during the observation period **(Figure 2-16. (c) and (f))**, whereas PIC/m with C/A of 0.90 and 1.00 were observed binding along the vessel wall and rapidly clearing from the bloodstream, with PIC/m having a C/A of 0.90 being cleared most rapidly **(Figure 2-16. (a) and (d), (b) and (e))**. From our ^{1}H-NMR observations, it is reasonable to assume that the PIC/m with C/A of 0.90 and 1.00 may be exposing the extra cationic units in the PIC core. Thus, the binding of PIC/m with C/A of 0.90 and 1.00 to the liver sinusoidal wall could be attributed to the abundant anionic proteoglycans presenting on the sinusoidal extracellular matrix, which enable capturing oligo-cations [15], as well as to the highly expressed scavenger receptors, which can recognize cationic charged macromolecules, on the surface of sinusoidal cells [15].

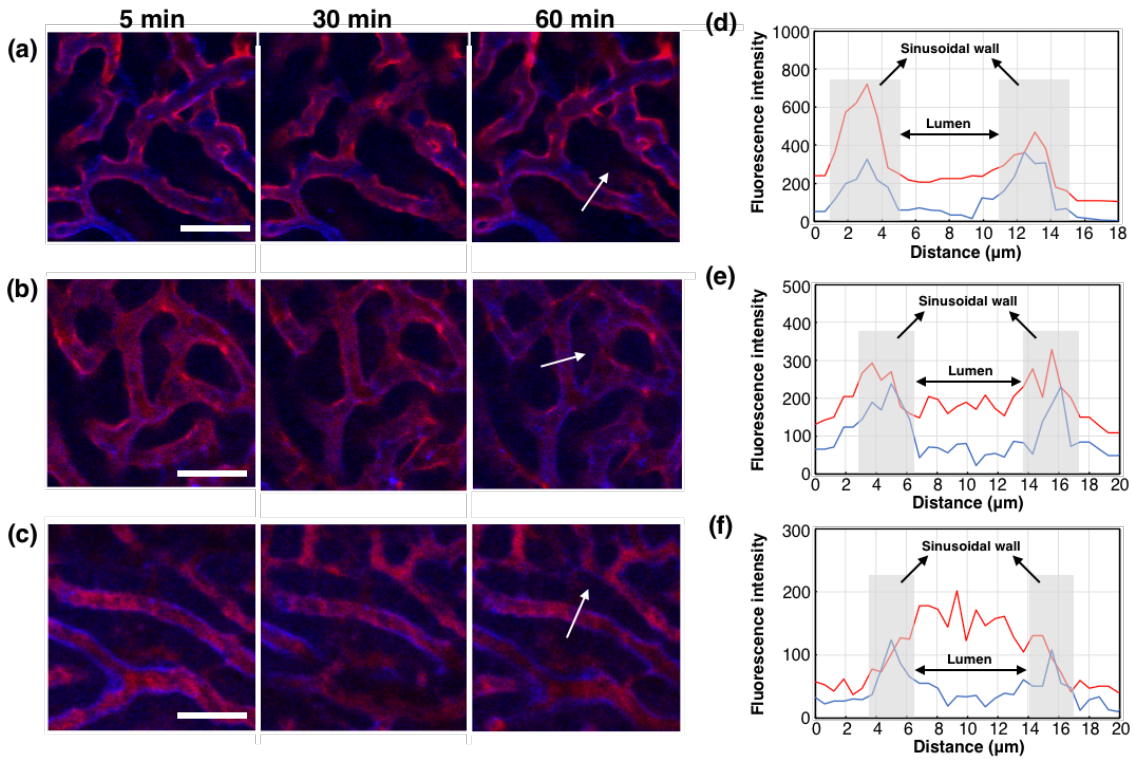

Figure 2-16. Cy5-PIC/m at a C/A of 0.90, 1.00 and 1.10 accumulated to liver sinusoidal wall. IVRT-CLSM images after injection of cy5-PIC/m (red) with C/A of (a) 0.90, (b) 1.00 and (c) 1.10. Liver sinusoidal wall (endothelial cells) was stained by eFluor405-PECAM-1 (blue). Intensity profiles of cy5 (red) and eFluor405 (blue) in the white arrows (a-c) are in (d-f), respectively: (d) 0.90, (e) 1.00 and (f) 1.10.

2. 4. Conclusion

Monodispersed PIC/m with diameter around 30-50 nm in a wide C/A area across the stoichiometry condition were effectively assembles. Although the sizes of these PIC/m are comparable, they present quite different physical properties, such as Z-potential and micellar association number. Further investigation of the core structure by ^{1}H-NMR showed that micelles bearing extra cationic units may exposed them from the PIC cores with low C/A. Evaluating the influence of these structural variations on the

biological performance of PIC/m gave contrasting results. Thus, PIC/m prepared with high C/A showed long blood-circulation, whereas PIC/m with low C/A were rapidly cleared from the bloodstream and accumulated mainly in the liver. Microscopic studies by direct liver observation with IVRT-CLSM suggested that PIC/m with low C/A may bind to the liver sinusoidal wall, which express abundant anionic proteoglycans. These findings provide valuable knowledge for precise formation of PIC-based nanocarriers with desired performance *in vivo*.

2. 5. References

1. Anraku, Y.; Kuwahara, H.; Fukusato, Y.; Mizoguchi, A.; Ishii, T.; Nitta, K.; Matsumoto, Y.; Toh, K.; Miyata, K.; Uchida, S.; Nishina, K.; Osada, K.; Itaka, K.; Nishiyama, N.; Mizusawa, H.; Yamasoba, T.; Yokota, T.; Kataoka, K., Glycaemic control boosts glucosylated nanocarrier crossing the BBB into the brain. *Nat Commun* **2017,** *8* (1), 1001.

2. Mutaf, O. F.; Kishimura, A.; Mochida, Y.; Kim, A.; Kataoka, K., Induction of Secondary Structure through Micellization of an Oppositely Charged Pair of Homochiral Block- and Homopolypeptides in an Aqueous Medium. *Macromol Rapid Commun* **2015,** *36* (22), 1958-64.

3. Wibowo, A.; Osada, K.; Matsuda, H.; Anraku, Y.; Hirose, H.; Kishimura, A.; Kataoka, K., Morphology Control in Water of Polyion Complex Nanoarchitectures of Double-Hydrophilic Charged Block Copolymers through Composition Tuning and Thermal Treatment. *Macromolecules* **2014,** *47* (9), 3086-3092.

4. Anraku, Y.; Kishimura, A.; Oba, M.; Yamasaki, Y.; Kataoka, K., Spontaneous formation of nanosized unilamellar polyion complex vesicles with tunable size and properties. *J Am Chem Soc* **2010,** *132* (5), 1631-6.

5. Endres, T. K.; Beck-Broichsitter, M.; Samsonova, O.; Renette, T.; Kissel, T. H., Self-assembled biodegradable amphiphilic PEG–PCL–lPEI triblock copolymers at the borderline between micelles and nanoparticles designed for drug and gene delivery. *Biomaterials* **2011,** *32* (30), 7721-7731.

6. Chandran, T.; Katragadda, U.; Teng, Q.; Tan, C., Design and evaluation of micellar nanocarriers for 17-allyamino-17-demethoxygeldanamycin (17-AAG). *International Journal of Pharmaceutics* **2010,** *392* (1), 170-177.

7. Tao, A.; Huang, G. L.; Igarashi, K.; Hong, T.; Liao, S.; Stellacci, F.; Matsumoto, Y.; Yamasoba, T.; Kataoka, K.; Cabral, H., Polymeric Micelles Loading Proteins through Concurrent Ion Complexation and pH-Cleavable Covalent Bonding for In Vivo Delivery. *Macromol Biosci* **2020,** *20* (1), e1900161.

8. Mutaf, O. F.; Anraku, Y.; Kishimura, A.; Kataoka, K., Unilamellar polyion complex vesicles (PICsomes) with tunable permeabilities for macromolecular solutes with different shapes and sizes. *Polymer* **2017,** *133*, 1-7.

9. Watanabe, S.; Hayashi, K.; Toh, K.; Kim, H. J.; Liu, X.; Chaya, H.; Fukushima, S.; Katsushima, K.; Kondo, Y.; Uchida, S.; Ogura, S.; Nomoto, T.; Takemoto, H.; Cabral, H.; Kinoh, H.; Tanaka, H. Y.; Kano, M. R.; Matsumoto, Y.; Fukuhara, H.; Uchida, S.; Nangaku, M.; Osada, K.; Nishiyama, N.; Miyata, K.; Kataoka, K., In vivo rendezvous of small nucleic acid drugs with charge-matched block catiomers to target cancers. *Nature Communications* **2019,** *10* (1), 1894.

10. Gref, R.; Minamitake, Y.; Peracchia, M. T.; Trubetskoy, V.; Torchilin, V.; Langer, R., Biodegradable long-circulating polymeric nanospheres. *Science* **1994,** *263* (5153), 1600-3.

11. Zahr, A. S.; Davis, C. A.; Pishko, M. V., Macrophage Uptake of Core−Shell Nanoparticles Surface Modified with Poly(ethylene glycol). *Langmuir* **2006,** *22* (19), 8178-8185.

12. Chuanoi, S.; Kishimura, A.; Dong, W.-F.; Anraku, Y.; Yamasaki, Y.; Kataoka, K., Structural factors directing nanosized polyion complex vesicles (Nano-PICsomes) to form a pair of block aniomer/homo catiomers: studies on the aniomer segment length and the catiomer side-chain structure. *Polymer Journal* **2014,** *46* (2), 130-135.

13. Szymusiak, M.; Kalkowski, J.; Luo, H.; Donovan, A. J.; Zhang, P.; Liu, C.;

Shang, W.; Irving, T.; Herrera-Alonso, M.; Liu, Y., Core-shell Structure and Aggregation Number of Micelles Composed of Amphiphilic Block Copolymers and Amphiphilic Heterografted Polymer Brushes Determined by Small-Angle X-ray Scattering. *ACS Macro Lett* **2017,** *6* (9), 1005-1012.

14. Dirisala, A.; Uchida, S.; Toh, K.; Li, J.; Osawa, S.; Tockary, T. A.; Liu, X.; Abbasi, S.; Hayashi, K.; Mochida, Y.; Fukushima, S.; Kinoh, H.; Osada, K.; Kataoka, K., Transient stealth coating of liver sinusoidal wall by anchoring two-armed PEG for retargeting nanomedicines. *Sci Adv* **2020,** *6* (26), eabb8133.

15. Lindberg, S.; Regberg, J.; Eriksson, J.; Helmfors, H.; Muñoz-Alarcón, A.; Srimanee, A.; Figueroa, R. A.; Hallberg, E.; Ezzat, K.; Langel, Ü., A convergent uptake route for peptide- and polymer-based nucleotide delivery systems. *Journal of Controlled Release* **2015,** *206*, 58-66.

Chapter 3.
Effect of ligand molecules amount and length of PEG chains on target recognition

3. 1. Introduction

Recently, we have succeeded to use the GLUT1 on BCECs for effectively overcoming the BBB by developing nanocarriers decorated with glucose molecules [1]. This system benefited from the accelerated translocation of GLUT1 from the apical side to the basal side after a period of fasting followed by administration of free glucose, which simultaneously transfers the glucosylated nanocarrier bound to the GLUT1 to the brain parenchyma. These findings indicate that the binding/dissociation balance of glucosylated nanocarriers to/from GLUT1 is important in the serial process of binding-translocation-release at the BBB. In this regard, the balance between binding and dissociation of glucosylated nanocarriers is necessarily managed by controlling the density of glucose ligands on the nanocarrier surface for tuning the multivalent interactions, by which the whole affinity is determined as the integration of the weak affinity between each component, *i.e.* glucose and GLUT1[2]. Thus, the crucial parameters involved in multivalent interactions are (i) the number of ligand molecules on each nanocarrier and (ii) the accessibility to GLUT1 for the glucose molecules on the surface of nanocarriers.

This study is devoted to clarify the effects of glucose ligand density and the spacer on GLUT1-mediated interaction between cells and glucose-conjugated nanocarriers. First, the effect of ligand density and the spacer effect was evaluated quantitatively by surface plasmon resonance (SPR). Because the isolation GLUT1 with preserved biological activity is difficult [3], this analysis was done by using the glucose-binding lectin concanavalin A (ConA) as a model molecule, which has moderate binding to glucose molecules comparable to GLUT1 and is an appropriate protein for the investigation of multivalent binding effect. Subsequently, we evaluated the roles of ligand density and spacer effect on the transporter-mediated delivery based the following *in vitro*

and *in vivo* experiments: (i) the uptake of the series of glucose-decorated nanocarriers into cells highly expressing GLUT1 was examined and contrasted with the SPR results; (ii) the ability of the glucosylated nanocarriers to reach brain parenchyma by targeting GLUT1 on BCECs coordinated with glycemic control was studied *in vivo* by quantifying their accumulation in brain tissues. Finally, we revealed the key structural features for glucosylated nanocarriers actively targeting GLUT1 through optimized molecular interaction between ligands and transporters.

3. 2. Experimental section

3. 2. 1. Materials

1, 2: 3, 4-di-O-isopropulidene-α-D-glucofuranoside (DIG) was purchased from Tokyo Chemistry Industry (Tokyo, Japan). Ethylene oxide (EO) and α-methoxy-ω-amino poly(ethylene glycol) (MeO-PEG-NH_2) (M_n = 2,000, 5,000 and 12,000; M_w/M_n = 1.05) were purchased from Nippon Oil and Fats Co. Ltd. (Tokyo, Japan). Tetrahydrofuran (THF) and dimethyl ether were purchased from Kanto Chemical Co. Inc. (Tokyo, Japan). Methanol (MeOH), triethylamine (TEA), collagenase, dispase, DNase type I, trypsin, puromycin and endothelial cell growth supplement were purchased from Sigma Aldrich Japan Co. LLC (Tokyo, Japan). Methanesulfonyl chloride (MsCl), trifluoroacetic acid (TFA), concanavalin A (ConA), RPMI-1640, DMEM, Ham's F12 medium, Hanks' Balanced Salt Solution (HBSS) and phloretin were purchased from FUJIFILM Wako Pure Chemical Co. (Tokyo, Japan). 1-ethyl-3-(3-dimethylaminopropyl) carbodiimide hydrochloride (EDC/HCl) were purchased from Tokyo Chemical Industry Co. Ltd. (Tokyo, Japan). Endothelial cell growth medium MV2 kit was purchased from Promocell GmbH (Heidelberg, Germany). CM5 sensor chip and EDC coupling kit

(including N-ethyl-N'-(3-demethylaminopropyl carbodiimide (EDC), N-hydroxysuccineimide (NHS) and ethanolamine) were purchased from Cytiva (Marborough, MA, USA). Cytochalasin B was purchased form Cayman Chemical Co. (Ann Arbor, MI, USA). Balb/c mice (female; 5 weeks old) and SD rats (female; 7 weeks) were purchased from Charles River Laboratories Japan (Kanagawa, Japan). All the animal experiments were performed according to the Guidelines for the Care and Use of Laboratory Animals, as stated by The University of Tokyo (Tokyo, Japan) and iCONM (Innovation Center of NanoMedicine, Kawasaki, Japan).

3. 2. 2. Polymer characterization

The degree of polymerization (DP) was determined by proton nuclear magnetic resonance (^{1}H-NMR) spectroscopy using JEOL ECS400 (JEOL Ltd., Tokyo, Japan). The molecular weight distribution of block copolymers was verified gel permeation chromatography (GPC) using a high performance liquid chromatography (HPLC) system (JASCO, Tokyo, Japan) connected to a Superdex 200-10/300GL column (GE Healthcare, Chicago, IL, USA).

3. 2. 3. Synthesis of glucose-decorated poly(ethylene glycol)-b-poly(α, β- aspartic acid)

Poly(ethylene glycol)-b-poly(α, β- aspartic acid) with glucose conjugated to the α-end of the PEG segment via a bond with the C6-O moiety (Gluc-PEG-PAsp) was synthesized as previously described (**Scheme 3-1.**)[1]. Firstly, DIG was sublimed in a vacuum at 70 ℃ and then dissolved in THF. Then, EO (45, 114 and 273 molar equivalent to DIG) was added to DIG solution in argon atmosphere after the addition of 0.3 M potassium naphthalene solution in THF (1 molar equivalent to DIG). The reaction

solution was stirred at room temperature for 48 hours, and then 1 mL of MeOH was added. DIG-PEG-OH (M_n of PEG = 2,000, 5,000 and 12,000) was obtained as a white powder after the reprecipitation in ice-cold diethyl ether.

The ω-hydroxyl group of DIG-PEG-OH was converted to ω-amino group by the following terminus amination method. DIG-PEG-OH was dissolved in THF and added to a THF solution of MsCl (5 molar equivalent to DIG-PEG-OH) with TEA (6 molar equivalent to DIG-PEG-OH) in ice. The reaction mixture was stirred at room temperature for 6 hours, and then precipitated as DIG-PEG-OMs into ice-cold diethyl ether. After drying under a vacuum, obtained white powder was dissolved in 25 % aqueous ammonia solution and stirred at room temperature for 2 days. The reaction solution was dialyzed against diluted ammonia solution, and then deionized water using a Spectra/Por 6 dialysis membrane (Repligen, Waltham, MA, USA) [MWCO: 1,000 Da] after evaporating. After the lyophilization, non-aminated PEG fraction was removed by ion-exchange chromatography using Sephadex C-25 (GE Healthcare, Chicago, IL, USA) and DIG-PEG-NH_2 was obtained.

DIG-PEG-PBLA was polymerized by ring-opening polymerization of BLA-NCA using the terminal primary amine group of DIG-PEG-NH2 according to the scheme described in the *section 2. 2. 3*. The benzyl ester groups of DIG-PEG-PBLA were deprotected with the same method as described in the *section 2. 2. 4*. and then DIG-PEG-PAsp was obtained. Protective groups of DIG moiety of DIG-PEG-PAsp were removed by dissolved in TFA/water (9:1, v/v) mixture and stirred at room temperature for 1 hour. The resulting solution was sequentially dialyzed against 10 mM NaOH for 1 day and deionized water for 1 day using a Spectra/Por 1 dialysis membrane [MWCO: 6,000 – 8,000 Da] and then lyophilized.

The DP of PAsp unit was calculated as shown in **table 3-1** from the ^{1}H-NMR measurement by comparing the peak area ratio using the methylene protons of PEG as the reference peak. The GPC spectra of obtained Gluc-PEG-PAsp was nearly unimodal.

3. 2. 4. Synthesis of block copolymers for preparing polymeric micelle

Poly(ethylene glycol)-poly(β-benzyl-L-aspartate) (MeO-PEG-PBLA) was polymerized by ring-opening polymerization of β-benzyl-L-aspartate *N*-carboxyl-anhydride (BLA-NCA) using the terminal primary amine group of α-methoxy-ω-amino poly(ethylene glycol) (MeO-PEG-NH_2) (M_n = 2,000, 5,000 and 12,000) as the initiator according to the scheme described in the *section 2. 2. 3*. Subsequently, Poly(ethylene glycol)-b-poly(α, β- aspartic acid) (MeO-PEG-PAsp, M_n of PEG = 2,000, 5,000 and 12,000), poly(ethylene glycol)-b-poly([5-aminopenthyl]- α, β-aspartamide) (MeO-PEG-P(Asp-AP), M_n of PEG = 2,000, 5,000 and 12,000) and cy5-labeled MeO-PEG-P(Asp-AP) polymers were synthesized according to the scheme described in the *section 2. 2. 4*., *2. 2. 5*. and *2. 2. 6*.

The DP of PAsp unit or P(Asp-AP) unit was calculated as shown in **table 3-1** from the ^{1}H-NMR measurement by comparing the peak area ratio using the methylene protons of PEG as the reference peak. The GPC spectra of obtained polymers were nearly unimodal.

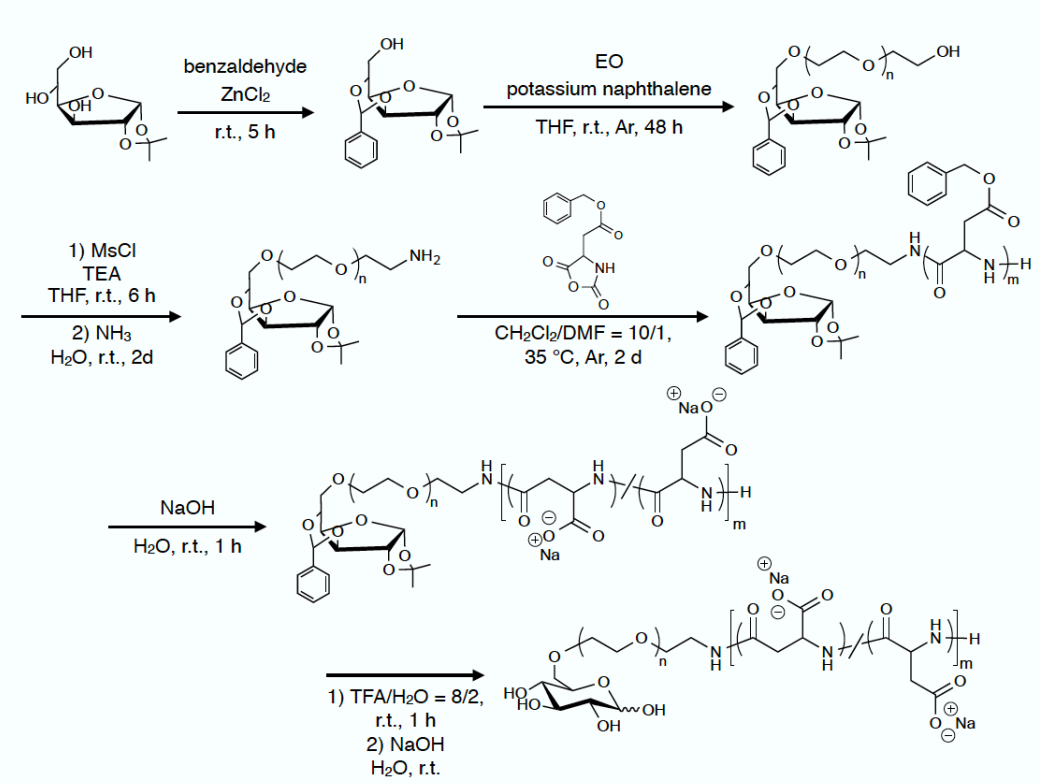

Scheme 3-1. Synthetic route for Gluc-PEG-PAsp block copolymer[1]

Table 3-1. Characterization of block copolymers for preparing G-PM

	M_n of PEG [Da]	DP of poly(amino acid) unit
Gluc-PEG-PAsp	12,000	76
	5,000	74
	2,000	70
MeO-PEG-PAsp	12,000	80
	5,000	72
	2,000	67
MeO-PEG-P(PAsp-AP)	12,000	67
	5,000	73
	2,000	69
MeO-PEG-P(Asp-AP)-cy5	12,000	80
	5,000	75
	2,000	68

3. 2. 5. Preparation of glucose-decorated polymeric micelle

Solution of block copolymers (Gluc-PEG-PAsp, MeO-PEG-PAsp, MeO-PEGP(Asp-AP) (and MeO-PEG-P(Asp-AP) for the preparation of cy5-labeled samples)) were prepared at a concentration of 1 mg/mL in 10 mM phosphate buffer (PB, pH 7.4, 0 mM NaCl) and passed through a 0.22 μm membrane filter to remove dust particulates. Gluc-PEG-PAsp solution and MeO-PEG-PAsp solution were mixed at varying residual molar ratio of carboxyl groups to obtain a series of block aniomer solutions, and then block aniomer and catiomer were subjected to vortex-mixing at 1.05 molar ratio of

carboxyl groups to amine groups to form glucose-decorated polymeric micelle (G-PM). For the purpose of preparing G-PM with varying chain length of PEG strands in the shell layer, block copolymers which contains PEG chains with the same chain length (M_n = 2,000, 5,000 and 12,000 for each) were combined into a micelle. Obtained G-PMs were named G-YPM with Y represents the chain length of PEG. All these G-PMs were cross linked by adding 10 mg/mL EDC/HCl in 10 mM PB at 10 molar equivalent amounts to carboxyl groups of block aniomer, and maintained overnight at room temperature followed by the purification via ultrafiltration with VIVASPIN 6 (Satrius stedium Biotech GmbH, Goettingen, Germany) [MWCO: 100,000 Da]. During the purification process, the solvent was replaced with deionized water (for static light scattering measurement), 10 mM PB (pH 7.4, 150 mM NaCl) (for surface plasmon resonance measurement) or D-PBS (-) (for cellular experiment and animal experiment).

3. 2. 6. Characterization of glucose-decorated polymeric micelle

The size and corresponding distribution of G-PM was evaluated by conducting dynamic slight scattering (DLS) measurement using a Zatasizer Nano ZS90 (Marvern Instruments Ltd., Worcestershire, UK) equipped with a diode-pumped solid state laser (532 nm) same as described in the *section 2. 2. 8*.

The molecular weight of G-PMs was verified by static light scattering (SLS) measurement using a DLS-8000 instrument (Otsuka Electronics, Osaka, Japan) as described in the *section 2. 2. 10*. And then, the micellar association number of G-PMs was calculated from the obtained result (molecular weight of G-PM) and molecular weight of building block copolymers.

The morphology of G-PMs was observed by transmission electron microscopy

(TEM) using JEM-1400 (JEOL, Tokyo, Japan) as described in the *section 2. 2. 11*.

3. 2. 7. Quantification of G-PM associated with GLUT-1 expressing cancer cells

MDA-MB-231 cells were cultured in RPMI-1640 medium (with 10 % FBS and 1 % penicillin streptomycin) at 37 ℃, 5 % CO_2. Cells were plated on 96 well black plate with a cell density of 10000 cells/well and then incubated for 24 h. These cells were subsequently treated with 20 μg/mL cy5-labeled G-PM containing medium for 1 h. Cells were thoroughly washed with HBSS(+) before fluorescence analysis with an Infinite M2000 Pro spectrophotometer (Tecan, Mannedorf, Switzerland). For the GLUT-1 inhibition assays, cells were preliminary incubated with a series of concentrations of GLUT inhibition reagent, phloretin and cytochalasin B, for 1 h, and then incubated with G-PM in the presence of inhibition reagent.

3. 2. 8. Primary brain endothelial cells isolation and culturing

Primary rat brain endothelial cells were extracted and isolated as previously described. SD rat (female, 8 weeks) was sacrificed, and then the brain was extracted and washed with cold HBSS buffer containing 1 % BSA and 2 % Pen/Strp. The brain cortex was cut out in the cold HBSS with 1 % BSA and 2 % Pen/Strp, sequentially the meninges and visible blood vessels on the surface was removed by rolling over the filter paper. The isolated cortex was incubated at 37 °C in the mixture of DMEM and Ham's F12 medium with DNase, collagenase and trypsin after homogenized. The medium solution containing digested brain cortex was centrifuged in 25 % BSA in HBSS several times, and the micro vasculatures were isolated as a small pellet. Following the 1 hour incubation in the mixture of DMEM and Ham's F12 medium with DNase, collagenase and trypsin at 37 °C,

obtained microvasculature cells were plated in on the cell culture flask coated with collagen and fibronectin. Cells were maintained in supplemented endothelial cell growth medium MV2 with 5 % Pen/Strep and 4 μg/mL puromycin. After culturing for several days, the concentration of puromycin was decreased to 1 μg/mL, and then 0 μg/mL. By sufficient cellular growth until reaching to the confluent, cells formed vasculature like morphology. For the experiments, cells were collected with trypsin/EDTA, seeded on black 96-well plate coated with collagen and fibronectin, and then cultured again until reaching to confluent.

3. 2. 9. Quantification of G-PM associated with rat primary brain endothelial cells

Primary rat brain endothelial cell monolayers plated to black 96-well plates were treated with cy5-labeled G-PM in supplemented MV2 medium without VEGF. After 1 h incubation with G-PM, cells were thoroughly washed with HBSS three times, fixed with 4 % PFA and stained with Hoechst to evaluate the number of cells. G-PM associated with endothelial cells and cell number in each well were quantified using Infinite M2000 Pro spectrophotometer (Tecan, Mannedorf, Switzerland).

3. 2. 10. Surface plasmon resonance measurement

Surface plasmon resonance (SPR) measurements were done using a BIACORE T200 (Cytica, Marlborough, MA, USA). Concanavalin A (conA) was bound to the carboxymethyl dextran gel on the surface of CM5 chip by amine coupling. A freshly prepared mixture of 0.2 M EDC and 0.05 M NHS in deionized water was injected, chemically activating the surface carboxymethyl groups of the gel. Then, 98 μL of 100 μg/mL conA solution in 10 mM PB (pH 7.4, 150 mM NaCl) was injected for the purpose

of immobilizing the activated surface of dextran gel until the response unit reached to 2000 RU (22 nm^2 for each conA molecule). Finally, the injection of 128 μL of 1M ethanolamine/HCl (pH 8.5) ensured the deactivation of non-reacted carboxymethyl ends on the surface of dextran gel. A similar procedure was done over a reference channel, for which the ligand injection was a blank injection of 10 mM PB (pH 7.4, 150 mM NaCl). Internal reference subtraction was then used to establish all data. G-PM sample solutions in 10 mM PB (pH 7.4, 150 mM NaCl) were injected with a series of different concentration with a contact time of 120 seconds and flow rate of 30 μL per minute. All experiments were conducted flowing 10 mM PB (pH 7.4, 150 mM NaCl) as a mobile phase at a room temperature.

3. 2. 11. Biodistribution of G-PM

To evauate the brain accumulation of G-PM *in vivo*, G-PM administrated to Balb/c under glycemic control as previously described. Balb/c mice (n = 5, female, 7 weeks old) were reared without food for 24 h. Then, these mice were intravenously injected with 200 μL of 1 mg/mL cy5-labeled G-PM in D-PBS(-). After 30 min, they were intraperitoneally injected with 200 μL of 20 wt% glucose solution in D-PBS(-). The mice were sacrificed 60 min after glucose injection and the excess blood was washed by perfusion with D-PBS(-). Blood was collected from the interior vena cava, heparinized and centrifuged to obtain plasma. The brain, liver, kidneys, spleen, heart, lung and femoral muscle were excised, washed with D-PBS(-), weighed after removing excess fluid and homogenized with cell lysis buffer using Multi Beads Shocker MBX (Yasui Kikai, Osaka, Japan). The accumulated amount of G-PM was quantified by measuring

fluorescent intensities using an Infinite M2000 Pro spectrophotometer (Tecan, Mannedorf, Switzerland).

3. 3. Results and discussion

3. 3. 1. Characterization of G-PM with varying length of PEG blocks

This research purposes on clarifying the effects of (i) the number and the density of glucose ligands and (ii) the spacer length of conjugated glucose on nanoparticulate carriers on their efficiency of GLUT1-mediated intra-/trans-cellular transport. For this purpose, core-crosslinked polyion complex micelles (PMs) with poly(ethylene glycol) (PEG) shell was selected as a model nanoparticulate carriers [17], since the number and the density as well as the spacer length of ligands can be independently and precisely controlled by managing the α-end functionality and the length of each PEG strands forming the shell layer of PMs. Furthermore, the association number of PMs is variable depending on the chain length balance between the hydrophilic segment, *i.e.*, PEG, and the ionically charged segment [4].

Glucose-conjugated PM (G-PM) was prepared by mixing the solutions of MeO-PEG-PAsp(AP), MeO-PEG-PAsp and Gluc(6)-PEG-PAsp at a stoichiometric residual molar ratio of amino groups to carboxyl groups. The number of glucose ligands on the PM was controlled by varying the mixing molar ratio of MeO-PEG-PAsp and Gluc(6)-PEG-PAsp in the solution. G-PMs were then crosslinked by adding 10 mg/mL EDC in 10 mM PB at 10 equivalent molar of the amount of residual carboxyl groups in the block copolymers, followed by the purification process as described in detail in **Experimental Section**. A series of G-PMs with different length of shell-forming PEG strands was prepared from the block copolymers with varying Mw of PEG segments as 2,000 (=2k), 5,000 (=5k) and

12,000 (=12k), respectively. G-PMs thus prepared are abbreviated as G-XkPM, where X stands for the Mw/1,000.

Then, the size, the polydispersity index (PDI), the association number, and the morphology of G-PM were characterized. Dynamic light scattering measurement revealed that the diameter of G-XkPMs was in the rage of 30-35 nm with narrow distribution (PDI<0.1) regardless of the length of PEG (**Table 3-1.**). Spherical morphology of G-XkPMs were confirmed in TEM images (**Figure 3-1.)**. The apparent molecular weight of G-XkPMs was determined from Zimm plots obtained by static light scattering (SLS) measurements, and the micellar association number was calculated from the micellar molecular weight assuming the charge stoichiometric composition of G-XkPMs. Obviously, the micellar association number decreased with an increase in the PEG length (**Table 1.**), presumably due to the higher steric repulsion of the longer PEG chains in the shell layer[5]. As molar ratio of MeO-PEG-PAsp(AP) and (MeO-PEG-PAsp + Gluc(6)-PEG-PAsp) in each of the G-XkPM should be unity at charge stoichiometric condition, maximum number of glucose ligands on a single G-XkPM is calculated to be the half the number of the micellar association number as summarized in Table 1. Accordingly, the number of glucose ligands on each of the G-XkPM can be readily tuned from zero to the half of the association number just by changing the mixing ratio of MeO-PEG-PAsp and Gluc(6)-PEG-PAsp in the preparation step.

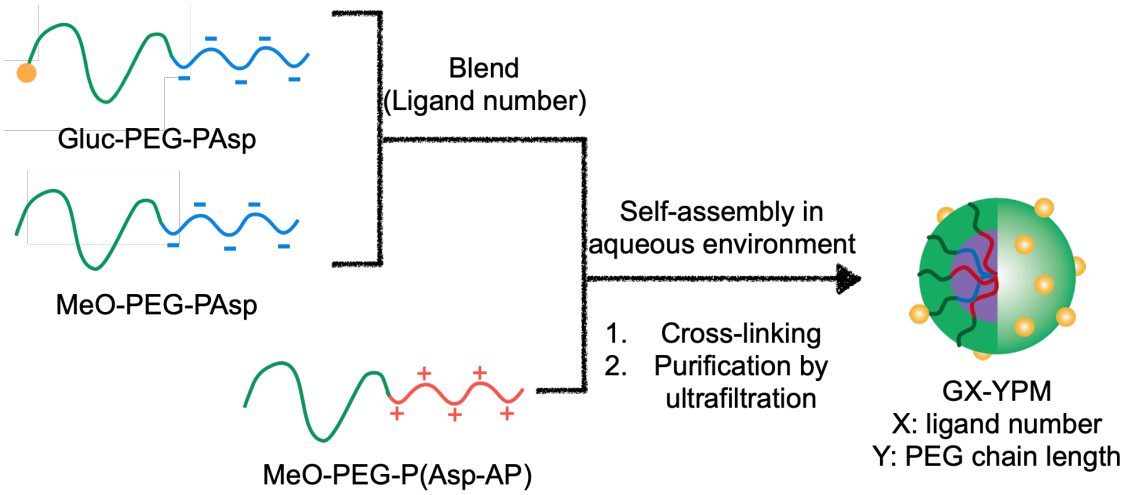

Scheme 3-2. Preparation of G-PM with varying length of PEG segment (chain length of PEG: 2,000, 5,000, and 12,000 Da)

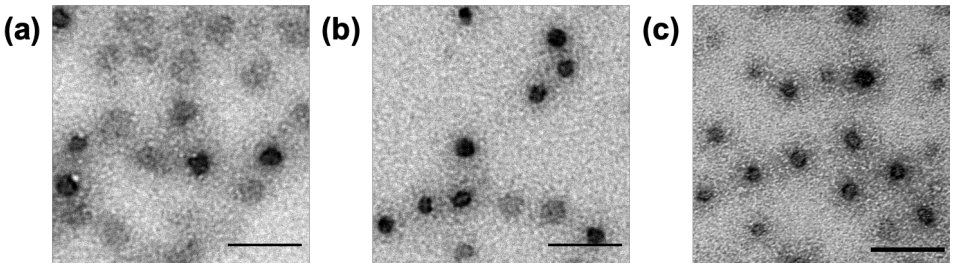

Figure 3-1. Transmission electron microscopic images of (a) G-2kPM, (b) G-5kPM and (c) G-12kPM

Table 3-2. Characterization of G-PM with different length of PEG chains

MW of PEG [Da]	Diameter[a] [nm]	PdI[b]	MW of micelles[c] [$\times 10^6$ Da]	Micellar association number[d]	Maximum glucose number[d]
2000	30.1 ± 0.67	0.041	2.62	131	66
5000	30.5 ± 0.24	0.058	2.01	87	44
12000	34.4 ± 0.43	0.077	1.12	44	22

[a]Determined by DLS (n = 3, means ± SD); [b]Polydispersity index of nanoparticles determined by DLS (n = 3); [c]Determined by SLS; [d]Calculated from MW of micelle

3. 3. 2. Effect of PEG chain length and ligand density on the interaction between G-PM and GLUT-1 highly expressing cancer cells

The binding affinity of glucose to GLUT-1 is rather weak with K_D of 3 x 10^{-3} M[6], and is much lower than other biospecific interactions often used in ligand-mediated targeting, such as antibody-antigen ($K_D \geq 10^{-8}$ M)[7] and integrin-peptides ($K_D \geq 10^{-9}$ M) interactions[8]. Thus, the multivalent interaction between multiple GLUT-1 molecules expressed on the targeted cellular surface and multiple glucose ligands conjugated on a nanoparticle plays a crucial role in maximizing the recognition process, as multivalency enables higher binding affinity based on the integration of weak molecular interactions[2]. Thus, we intensively examined here the mutivalency effect on the GLUT-1 mediated uptake of Cy5-lablled G-XkPM (G-XkPM-Cy5) into human breast adenocarcinoma (MDA-MB-231) cells known to overexpressing GLUT-1[9-11].

The number of glucose ligands on G-XkPM was tuned by varying the mixing molar ratio of MeO-PEG-PAsp and Gluc(6)-PEG-PAsp in the preparation step, and thus prepared micelle sample was abbreviated as GY-XkPM, where Y stands the number of glucose ligands on each of the micelle calculated from the data given in Table 1. It should be noted that the size of GY-XkPM is almost constant (~30 nm) regardless of PEG length. Therefore, if the micelle samples are set up to have the equal number of glucose ligands per micelle, their glucose ligand density on the surface can be regarded as same. Notably, as seen in **Figure 3-2**, there was observed a clear threshold in cellular uptake of G-2kPM with increasing number of glucose ligands, and obviously, the uptake abruptly increased for those with more than 33 ligands. To check whether this boosted cellular uptake indeed occurred via GLUT-1 dependent pathway, inhibition assay was conducted using GLUT

inhibitors, *i.e.*, phloretin and cytochalasin B. As seen in **Figure 3-3**, G33-2kPM uptake into MDA-MB-231 cells significantly and dose dependently decreased in the presence of phloretin and cytochalasin B, indicating that the uptake is mediated by the interaction of GLUT-1 molecules with glucose ligands on the micelles. This result suggests that a critical multivalent ligand effect may be achieved when the density of glucose ligands on the surface of PM reaches to the critical value to allow a substantial multivalent interaction with GLUT-1 molecules expressed on the cell surface. In addition, cellular association of G-2kPM to rat primary endothelial cells showed similar ligand number dependency as shown in **Figure 3-4**. As the diameter of G-2kPM is 30.1 ± 0.67 nm (**Table 3-2**), the footprint of a glucose molecule on the surface of G33-2kPM is calculated to be 86 nm^2. Thus, a distance between two glucose ligands on G33-2kPM is estimated to be 9.9 nm. Worth noting in this regard is that GLUT-1 molecule with a size of 4.6 nm[12] is known to form dimer and tetramer on the cellular surface[13]. It may be reasonable to assume that the density of glucose ligands on G33-2kPM may become high enough to induce multivalent interaction with GLUT-1 dimer and tetramer on the cellular membrane surface.

In a sharp contrast with G-2kPM series, no drastic increase in ligand density-dependent cellular uptake was observed for G-5kPM series, and the G44-5kPM uptake into the cells was just slightly higher than G0-5kPM. In this regard, it is important to note the glucose molecules conjugated to the α-end of longer PEG chain are less likely to be exposed compared to glucose molecules installed on shorter PEG chains, assuming a random-coiled conformation of tethered polymer strands. Furthermore, the steric repulsion between neighboring PEG chains may be increased for longer PEG chains[14], and this might also be a factor to impair the approach of glucose-ligand to the recognition site in

GLUT-1 channel locating in a recessed position with low accessibility. These factors are assumed to be the reason for the restrained cellular uptake of G-5kPM compared to G-2kPM, having the same number of glucose ligands. All the samples in G-12kPM series revealed no increase in cellular uptake even elevating the number of glucose ligands per micelle. Unfortunately, the maximum number of glucose ligands per micelle in G-12kPM series was limited to lower than the range expecting to observe multi-valency effect due to the decreased association number of the micelle, yet it may be reasonable to assume the less favorable multivalent interaction with GLUT-1 compared to G-2kPM and G-5kPM serieses due to lowered ligand-exposure and higher steric repulsive effects of longer PEG strands.

The *in vitro* evaluation of GLUT-1 recognition of G-PMs does not fully reflect the *in vivo* situation, particularly monolayer cultured cells are not affected by blood flow and interaction with other brain cells regulating the direction of brain parenchyma and brain vasculature. Moreover, while several sophisticated *in vitro* BBB models are under investigation, they still do not completely reflect *in vivo* conditions. Thus, it is necessary to investigate BBB penetration ability of G-PM *in vivo* to determine optimized structural parameters.

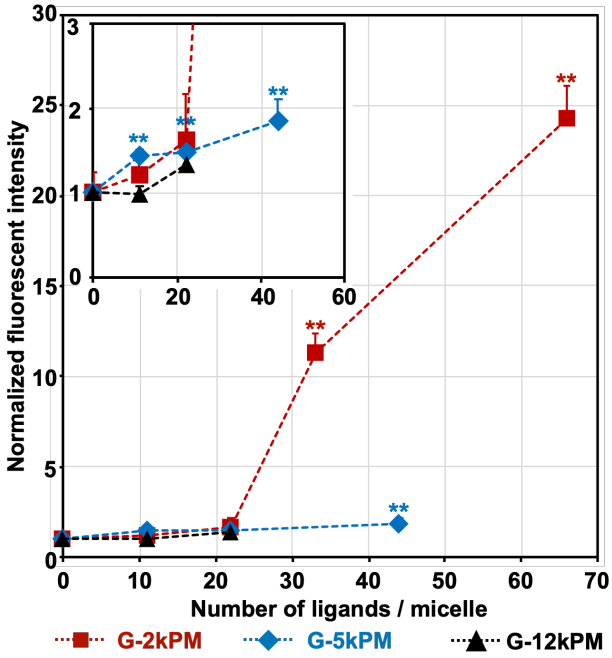

Figure 3-2. Cellular of internalization G-PM with GLUT-1 highly expressing cancer cells (MDA-MB-231) (n = 10, means ±SE, t-test with G-0PM, *; $p < 0.05$, **; $p < 0.01$)

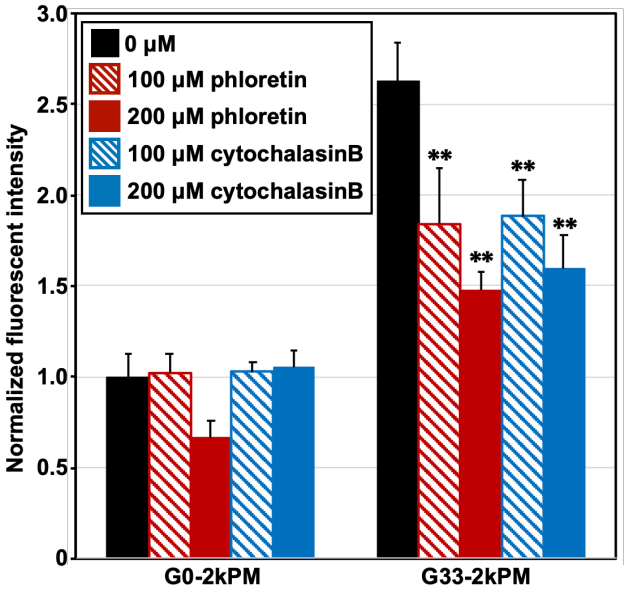

Figure 3-3. G33-2kPM and G0-2kPM internalization with MDA-MB-231 cells inhibited by phloretin and cytochalasin B (n = 10, means ±SE, t-test with 0 μM, **; $p < 0.01$)

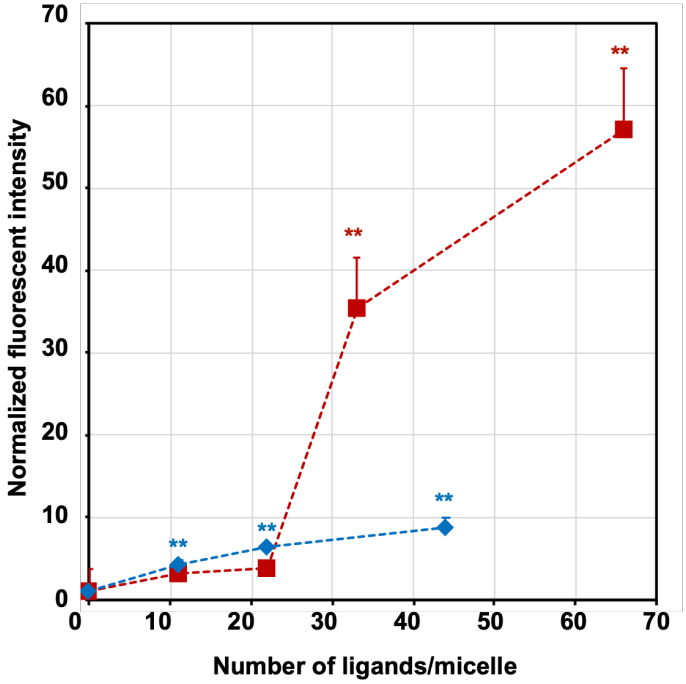

Figure 3-4. Internalization of G-2kPM and G-5kPM with rat primary BCECs (n = 5, means ± SE, t-test with G0-PM, **; $p < 0.01$)

3. 3. 3. Quantitative analysis of interaction between G-PM and sugar binding lectins

The binding affinity of G-PM with PEG chains having different length to the targeted protein was quantified using surface plasmon resonance (SPR) to clarify how the ligand density affects target recognition of G-PM. In this study, we conjugated the lectin ConA, which recognizes glucose, on the surface of sensor chips and quantified the binding affinity by flowing G-PM in the channel and tracing their dissociation after flowing buffer. The dissociation constant (K_D) of each G-PM from ConA is shown in **Table 3-3**. G66-2kPM presented double-digit smaller dissociation constant compared to G33-2kPM, which means that G66-2kPM has much stronger binding affinity to conA than G33-2kPM. It is important to note that all the glucose molecules on G-PMs binding

to ConA are required to dissociate for the detaching G-PM from the ConA-installed sensorchip. In other words, G-PM binding to the ConA molecules on the surface by multivalent interactions are less likely to dissociate from the chip. Thus, the strong binding affinity of G66-2kPM to ConA suggests that a high ligand density on the surface of nanoparticles contributes to obtaining multivalency, intensifying the binding affinity of G-PM to ConA. As 1 ConA molecule on the sensor chip occupies 22 nm^2, which is calculated from increasing of response with 2000 RU after ConA immobilization (1 RU = 1 pg/mm^2 protein), the distance between each ConA molecule is 5 nm. Because the distances between each glucose molecule on the surface of G-PMs are 9.9 nm for G33-2kPM and 7 nm for G66-2kPM, it is consistent that multivalent binding between ConA and G-PM was obtained.

Based on our findings showing that the length of PEG chains determines maximum ligand density of G-PM through the association number, it is important to also study the formulations with longer PEG chains. Thus, the binding of G-5kPM was found to be stronger as the ligand density increased. However, the binding affinity of G-5kPM to ConA was weaker than that of G-2kPM having the same ligand density. Moreover, G-12kPM binding to ConA cannot be quantified as the SPR signal was quite low. Generally, ligand molecules conjugated to a-end of longer PEG chains are less likely to be expose on the surface, as well as restrained by the surrounding steric repulsion of PEG. Hence, the accessibility of ligand molecules to targeted proteins is determined by the length of PEG chains, that is, longer PEG chains restrict the target recognition of ligands. Consequently, the effective number of ligand molecules on one nanoparticle that are available for ConA binding decreases when the ligands are conjugated to longer PEG chains.

Table 3-3. Dissociation constant of G-PMs from glucose-binding lectin (concanavalin A) evaluated by surface plasmon resonance measurements

	G66-2kPM	G33-2kPM	G44-5kPM	G22-5kPM
K_D	7.40×10^{-8}	2.26×10^{-6}	1.88×10^{-4}	3.78×10^{-4}

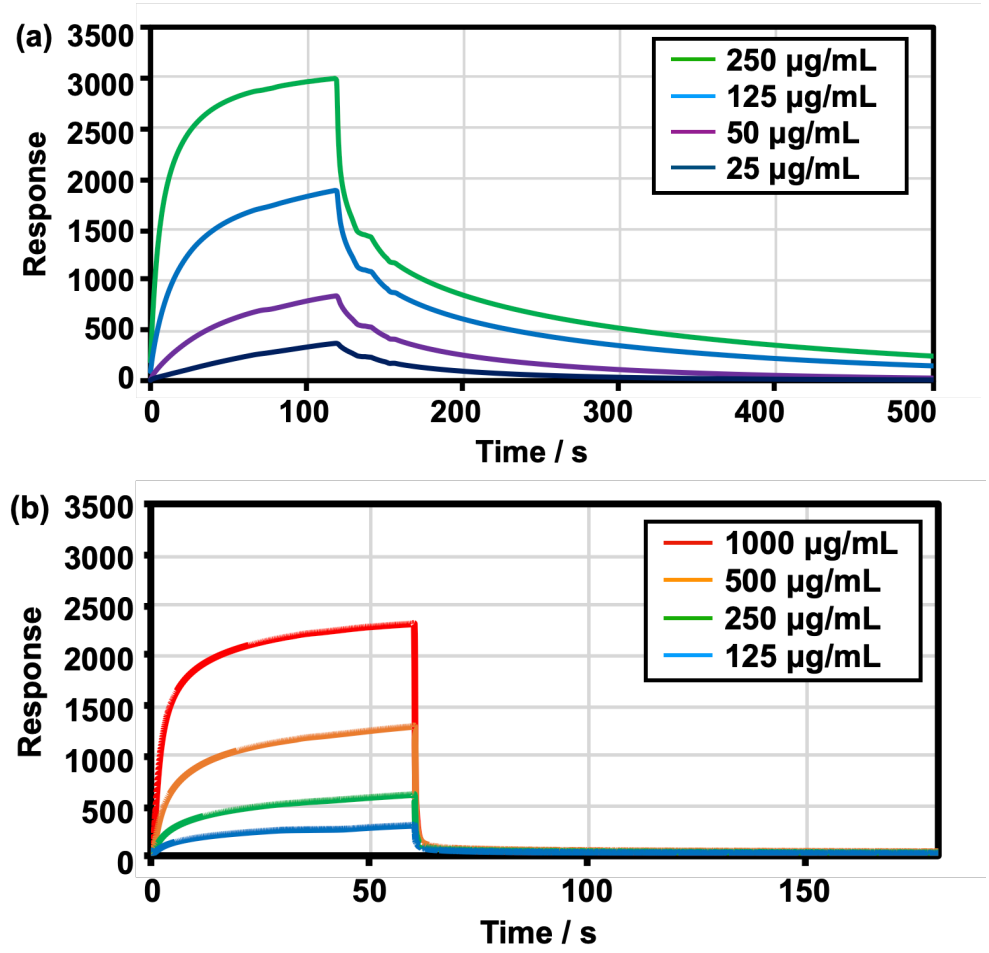

Figure 3-5. SPR sensorgram of (a) G66-2kPM and (b) G33-2kPM binding to concanavalin A

3. 3. 4. Brain accumulation efficacy of systemically-administrated G-PM with varying length of PEG chains

The results of the preceding section revealed that the glucose ligands on the G-PMs were able to be recognized by GLUT-1 molecules expressed on cellular surfaces, facilitating the cellular uptake of G-PM depending on the PEG length and the glucose density per micelle. Here, we applied these GLUT-1 recognizable G-PMs to *in vivo* study, examining their capability of systemically targeting the brain through the multivalent interaction with GLUT-1 molecules overexpressing on the brain capillary endothelial cells (BCECs). According to our previous report[1], the experiments were done with 24hr fasting mice receiving *i.p.* injection of glucose 30 min after systemic administration of G-PM to facilitate GLUT-1 translocation from apical to basal sides of the BBB. It should be noted, as summarized in **Table 3-4**, all the series of G-PM has appreciable longevity in blood circulation with >80% of initial dose remaining in plasma even 90 min after the injection, indicating that the brain accumulation behavior of these G-PMs can be compared without considering the difference in the blood circulation profile. As seen in **Figure 3-6**, there is a clear trend of increasing brain accumulation with decreasing the PEG length of the micelle shell. Comparing at the sample having the same number (density) of glucose ligands per micelle, the G-2kPM series always attained higher brain accumulation than the G-5kPM and G-12kPM serieses. There is also a trend that the

accumulation increased with an increase in the number of glucose ligands, except for the G-2kPM with highest number of glucose (G66-2kPM). Apparently, as discussed in the preceding section addressing GLUT-1 mediated uptake of G-PMs into MDA-MB-231 cells, these trends of increasing brain accumulation with decreasing PEG length and increasing the number of glucose ligands is consistent with the view of facilitated multivalent interaction of glucose ligands on the micelle with GLUI-1 molecules due to the synergistic contribution of increased ligand density, lowered steric repulsion, and higher probability of ligand exposure. Note that highest brain accumulation of 6% of dose/g-brain achieved here by G33-2kPM is comparable with our previous result obtained by the micelle with the same composition[1]. This value is much more efficient than previously developed brain targeting nanoparticulate systems such as transferrin-conjugated liposome ($\approx$ 0.1 %ID)[15] and angiopep-2 decorated polymeric micelle ($\approx$0.4 %ID/g)[16].

Worth noting in the results shown in **Figure 3-6** is that the further increase in the density of glucose ligands over G33-2kPM resulted in the significant decrease in brain accumulation, even though more effective multivalent interaction with GLUT-1 molecules is expected. Actually, the presence of optimal glucose density on the micelle surface to maximize brain accumulation has already been observed in our previous study

[20], and the present examination faithfully reconfirmed this observation. The phenomenon might be explained by assuming the restricted release of the micelles with high density of glucose ligands from GLUT-1 molecules on BCEC at the basal side due to lowered dissociation constant derived from strong and effective multivalent glucose-GLUT-1 interaction (**Figure 3-7.**).

Table 3-4. Stability of G-PM in the blood stream 90 min after intravenous administration to mice (n = 5, means ± SE)

	% of dose in plasma
G0-2kPM	90.2 ± 11
G11-2kPM	91.9 ± 8.8
G33-2kPM	104 ± 12
G66-2kPM	84.9 ± 11
G0-5kPM	97.6 ± 9.9
G11-5kPM	103 ± 6.0
G22-5kPM	85.8 ± 3.9
G44-5kPM	92.9 ± 5.8
G0-12kPM	81.9 ± 11
G11-12kPM	94.3 ± 3.1
G22-12kPM	90.4 ± 2.7

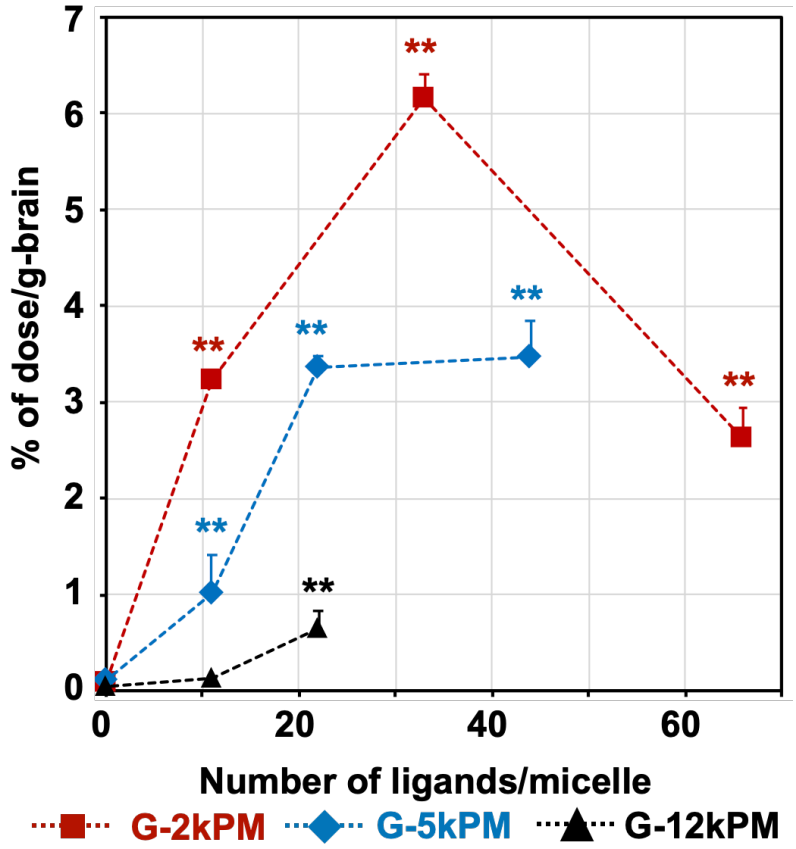

Figure 3-6. Brain accumulation ratio of G-PM (n = 5, means ± SE, t-test with G0-PM, **; $p < 0.01$)

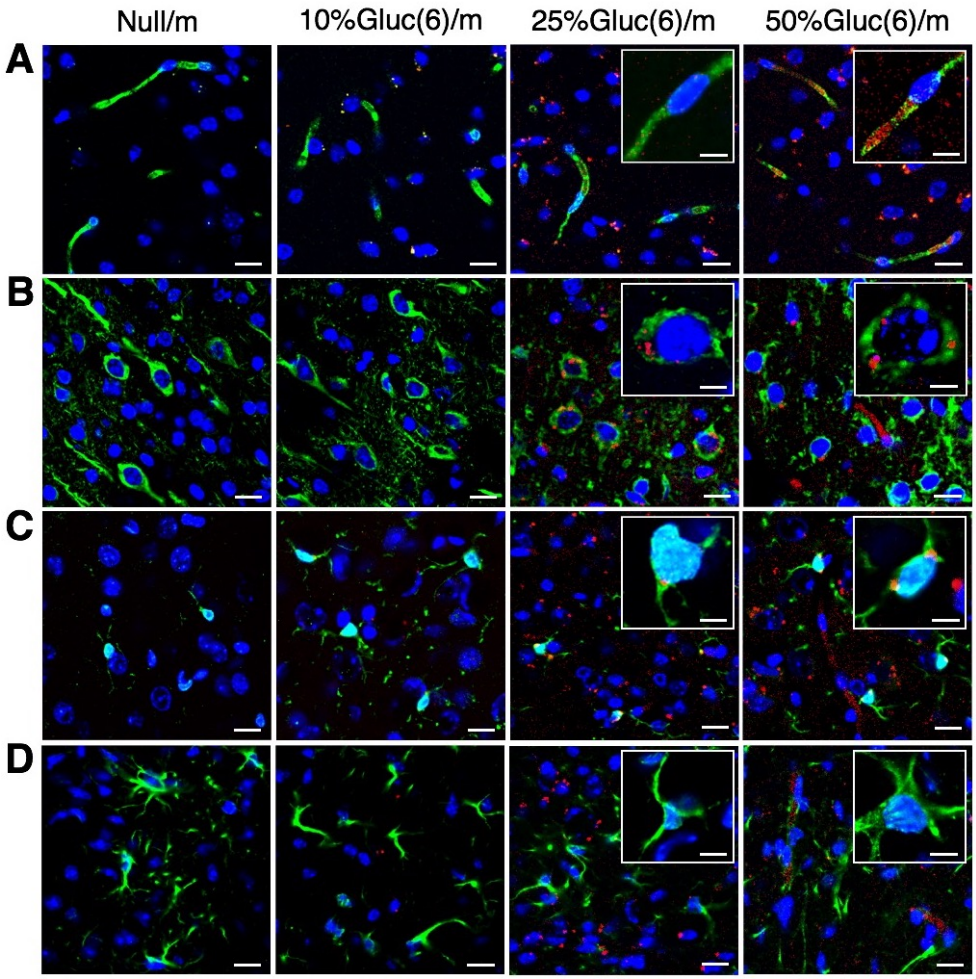

Figure 3-7. Immunohistochemical analysis of the of mice after the administration of G-2kPMs. Brain sections extracted 48 h after the administration of G0-2kPM (Null/m), G11-2kPM (10%Gluc(6)/m), G33-2kPM(25%Gluc(6)/m) and G66-2kPM (50%Gluc(6)/m) labeled with cy5 (red). BCECs (a), neurons (b), microglial cells (c) and astrocytes (d) are labeled and visualized with anti-PECAM1, anti-Tuj1, anti-Iba1 and anti-GFAP antibodies, respectively (green). Nuclei are labeled with DAPI (blue). The scale bar indicates 20 μm (10 μm in insets) (**Previously published data**[1])

3. 4. Conclusion

G-PM has outstanding BBB penetration efficiency, with brain accumulation

levels that are orders of magnitude higher than other DDS targeting the brain. We found that the length of PEG chains dramatically affects to the association number of G-PMs, which decreased as the length of PEG chains, resulting in a lower number of ligands per micelle. Such structural alterations limit the multivalency between the glucose ligands on the micelles and GLUT-1 on cells that is necessary for transporter-mediated DDS using small molecules as ligands. Notably, there was a ligand density threshold for increasing the binding affinity of G-PM to GLUT-1 on cultured cells *in vitro*, indicating that the multivalent effect is critical for G-PM association to GLUT-1. For successful brain accumulation of G-PM *in vivo*, we clarified that the ligand density affects the targeting efficiency and the PEG length drastically changes the interaction of ligand molecules to the target protein due to the steric repulsion with neighboring PEG chains.

3. 5. References

1. Anraku, Y.; Kuwahara, H.; Fukusato, Y.; Mizoguchi, A.; Ishii, T.; Nitta, K.; Matsumoto, Y.; Toh, K.; Miyata, K.; Uchida, S.; Nishina, K.; Osada, K.; Itaka, K.; Nishiyama, N.; Mizusawa, H.; Yamasoba, T.; Yokota, T.; Kataoka, K., Glycaemic control boosts glucosylated nanocarrier crossing the BBB into the brain. *Nat Commun* **2017,** *8* (1), 1001.

2. Mammen, M.; Choi, S. K.; Whitesides, G. M., Polyvalent Interactions in Biological Systems: Implications for Design and Use of Multivalent Ligands and Inhibitors. *Angew Chem Int Ed Engl* **1998,** *37* (20), 2754-2794.

3. Pattnaik, P., Surface plasmon resonance: applications in understanding receptor-ligand interaction. *Appl Biochem Biotechnol* **2005,** *126* (2), 79-92.

4. Harada, A.; Kataoka, K., Effect of Charged Segment Length on Physicochemical Properties of Core−Shell Type Polyion Complex Micelles from Block Ionomers. *Macromolecules* **2003,** *36*.

5. Hagan, S. A.; Coombes, A. G. A.; Garnett, M. C.; Dunn, S. E.; Davies, M. C.; Illum, L.; Davis, S. S.; Harding, S. E.; Purkiss, S.; Gellert, P. R., Polylactide−Poly(ethylene glycol) Copolymers as Drug Delivery Systems. 1. Characterization of Water Dispersible Micelle-Forming Systems. *Langmuir* **1996,** *12* (9), 2153-2161.

6. Patching, S. G., Glucose Transporters at the Blood-Brain Barrier: Function, Regulation and Gateways for Drug Delivery. *Mol Neurobiol* **2017,** *54* (2), 1046-1077.

7. Landry, J. P.; Ke, Y.; Yu, G. L.; Zhu, X. D., Measuring affinity constants of 1450 monoclonal antibodies to peptide targets with a microarray-based label-free assay platform. *J Immunol Methods* **2015,** *417*, 86-96.

8. Sato, Y.; Uemura, T.; Morimitsu, K.; Sato-Nishiuchi, R.; Manabe, R.; Takagi, J.; Yamada, M.; Sekiguchi, K., Molecular basis of the recognition of nephronectin by integrin alpha8beta1. *J Biol Chem* **2009,** *284* (21), 14524-36.

9. Younes, M.; Brown, R. W.; Mody, D. R.; Fernandez, L.; Laucirica, R., GLUT1 expression in human breast carcinoma: correlation with known prognostic markers. *Anticancer Res* **1995,** *15* (6B), 2895-8.

10. Younes, M.; Lechago, L. V.; Somoano, J. R.; Mosharaf, M.; Lechago, J., Wide expression of the human erythrocyte glucose transporter Glut1 in human cancers. *Cancer Res* **1996,** *56* (5), 1164-7.

11. Brown, R. S.; Wahl, R. L., Overexpression of Glut-1 glucose transporter in human breast cancer. An immunohistochemical study. *Cancer* **1993,** *72* (10), 2979-85.

12. Salas-Burgos, A.; Iserovich, P.; Zuniga, F.; Vera, J. C.; Fischbarg, J., Predicting the three-dimensional structure of the human facilitative glucose transporter glut1 by a novel evolutionary homology strategy: insights on the molecular mechanism of substrate migration, and binding sites for glucose and inhibitory molecules. *Biophys J* **2004,** *87* (5), 2990-9.

13. Looyenga, B.; VanOpstall, C.; Lee, Z.; Bell, J.; Lodge, E.; Wrobel, K.; Arnoys, E.; Louters, L., Determination of GLUT1 Oligomerization Parameters using Bioluminescent Förster Resonance Energy Transfer. *Scientific Reports* **2016,** *6* (1), 29130.

14. Kenworthy, A. K.; Hristova, K.; Needham, D.; McIntosh, T. J., Range and magnitude of the steric pressure between bilayers containing phospholipids with covalently attached poly(ethylene glycol). *Biophys J* **1995,** *68* (5), 1921-1936.

15. van Rooy, I.; Mastrobattista, E.; Storm, G.; Hennink, W. E.; Schiffelers, R. M., Comparison of five different targeting ligands to enhance accumulation of liposomes into

the brain. *Journal of Controlled Release* **2011,** *150* (1), 30-36.

16. Shen, J.; Zhan, C.; Xie, C.; Meng, Q.; Gu, B.; Li, C.; Zhang, Y.; Lu, W., Poly(ethylene glycol)-block-poly(d,l-lactide acid) micelles anchored with angiopep-2 for brain-targeting delivery. *Journal of Drug Targeting* **2011,** *19* (3), 197-203.

Chapter 4.
BBB penetration of cocktail PEGylated glucose-decorated polymeric micelle

4. 1. Introduction

Despite the fact that glucose-decorated micelles with short length PEG strands with a molecular weight of 2 kDa can be recognized by GLUT-1 and observed accumulating in brain, micelles with long length PEG strands with a molecular weight of 12 kDa cannot recognize GLUT-1. For the purpose of increasing stability of micelles and loading various drugs, the development of ligand-loaded micelles with high molecular weight PEG chains which maintains the ligand accessibility to the target membrane proteins is highly required. Previous research hypothesized that the ligand accessibility is reduced by the neighboring PEG chains and the target receptor recognition of ligands is restrained when longer ligand-installed PEG chains attached to nanoparticles[1].

In this chapter, for the purpose of overcoming this PEG dilemma, the novel polymeric micelle design consisting of long PEG chains conjugated with the glucose ligand molecules and short PEG chains was developed. This technique is called cocktail PEGylation, and mixing short PEG strands is expected to improve the target recognition of ligand molecules[2-4]. The interaction between GLUT-1 and cocktail PEGylated G-PM was investigated both *in vitro* and *in vivo*. The brain accumulation of G-PM baring long PEG chains was drastically increased by cocktail PEGylation.

4. 2. Experimental section

4. 2. 1. Materials

Gluc(6)-PEG-PAsp (Mn of PEG = 12,000, DP of PAsp = 70), MeO-PEG-PAsp (Mn of PEG = 12,000, DP of PAsp = 67), MeO-PEG-PAsp (Mn of PEG = 2,000, DP of PAsp = 80), MeO-PEG-P(Asp-AP) (Mn = 12,000, DP of P(Asp-AP) = 69) and MeO-PEG-P(Asp-AP) (Mn of PEG = 2,000, DP of P(Asp-AP) = 67) were synthesize

as described in the *section 3. 2. 3.* and *3. 2. 4.* Collagenase, dispase, DNase type I, trypsin, puromycin and endothelial cell growth supplement were purchased from Sigma Aldrich Japan Co. LLC (Tokyo, Japan). Concanavalin A (ConA), RPMI-1640, DMEM, Ham's F12 medium, Hanks' Balanced Salt Solution (HBSS) phloretin and anti Iba-1 antibody were purchased from FUJIFILM Wako Pure Chemical Co. (Tokyo, Japan). 1-ethyl-3-(3-dimethylaminopropyl) carbodiimide hydrochloride (EDC/HCl) were purchased from Tokyo Chemical Industry Co. Ltd. (Tokyo, Japan). Endothelial cell growth medium MV2 kit was purchased from Promocell GmbH (Heidelberg, Germany). CM5 sensor chip and EDC coupling kit (including N-ethyl-N'-(3-demethylaminopropyl carbodiimide (EDC), N-hydroxysuccineimide (NHS) and ethanolamine) were purchased from Cytiva (Marborough, MA, USA). Cytochalasin B was purchased form Cayman Chemical Co. (Ann Arbor, MI, USA). Passive lysis buffer was purchased from Promega Corporation (Madison, WI, USA). Anti PECAM-1 antibody was purchased from Santa Cruz Biotechnology (Dallas, TX, USA). Anti TUj-1 antibody was purchased from Covance Inc. (Princeton, NJ, USA). Anti GFAP antibody was purchased from Merc Millipore (Burlington, MA, USA). Goat anti-rat IgG (H+L) cross-adsorbed secondary antibody, Alexa Fluor 488, goat anti-rabbit IgG (H+L) cross-adsorbed secondary antibody, Alexa Fluor 488 and Prolong gold with DAPI were purchased from Thermo Scientific (Waltham, MA, USA). Balb/c mice (female; 5 weeks old) and Sprague-Dawley rats (female; 7 weeks old) were purchased from Charles River Laboratories Japan (Kanagawa, Japan). All the animal experiments were performed according to the Guidelines for the Care and Use of Laboratory Animals, as stated by The University of Tokyo (Tokyo, Japan) and iCONM (Innovation Center of NanoMedicine, Kawasaki, Japan).

4. 2. 2. Preparation of cocktail PEGylated glucose-decorated polymeric micelle

Cocktail PEGylated G-PM (cG-PM) was prepared with Gluc(6)-PEG-PAsp (Mn of PEG = 12,000, DP of PAsp = 70), MeO-PEG-PAsp (Mn of PEG = 12,000, DP of PAsp = 67), MeO-PEG-PAsp (Mn of PEG = 2,000, DP of PAsp = 80), MeO-PEG-P(Asp-AP) (Mn = 12,000, DP of P(Asp-AP) = 69) and MeO-PEG-P(Asp-AP) (Mn of PEG = 2,000, DP of P(Asp-AP) = 67). Solution of block copolymers were prepared at a concentration of 1 mg/mL in 10 mM phosphate buffer (PB, pH 7.5, 0 mM NaCl) and passed through a 0.22 μm membrane filter to remove dust particulates. These block aniomer and catiomer solutions were subjected to vortex mixing at 1.05 molar ratio of carboxyl groups to amine groups to form cG-PM with varing fraction of shorter PEG strands and glucose-decorated longer PEG strands in PEG shell layer (**Scheme 4-1.**). All these cG-PMs were cross linked by adding 10 mg/mL EDC/HCl in 10 mM PB at 10 molar equivalent amounts to carboxyl groups of block aniomer, and maintained overnight at room temperature followed by the purification via ultrafiltration with VIVASPIN 6 (Satrius stedium Biotech GmbH, Goettingen, Germany) [MWCO: 100,000 Da]. During the purification process, the solvent was replaced with deionized water (for static light scattering measurement and analytical ultracentrifugation measurement) or D-PBS (-) (for surface plasmon resonance measurement, cellular experiment and animal experiment).

4. 2. 3. Characterization of cG-PM

The size and corresponding distribution of G-PM was investigated by conducting dynamic slight scattering (DLS) measurement using a Zatasizer Nano ZS90 (Marvern Instruments Ltd., Worcestershire, UK) connected to a diode-pumped solid state laser

(wavelength = 532 nm) same as described in the section *2. 2. 8*.

The molecular weight of G-PMs was verified by static light scattering (SLS) measurement using a DLS-8000 instrument (Otsuka Electronics, Osaka, Japan) as described in the section *2. 2. 10*. And then, the micellar association number of G-PMs was calculated from the obtained result (molecular weight of G-PM) and molecular weight of building block copolymers.

The morphology of G-PMs was observed using transmission electron microscopy (TEM) using JEM-1400 (JEOL, Tokyo, Japan) as described in the section *2. 2. 11*.

4. 2. 4. Analytical ultracentrifugation measurement

Analytical ultracentrifugation (AUC) measurement was performed using an analytical ultracentrifuge Optima XL-1 (Beckman Coulter, Brea, CA, USA) equipped with AnTi60 rotor cells that were able to hold three sets of 1.2 mm two channels Epon filled centerpieces. The measurement was carried by the setting the detection of absorbance at 220 nm and the rotation speed to 150,000 rpm at room temperature. Radial absorbance data was collected in continuously scanning mode at 0.002 cm intervals and 3 minutes increments for a total of 120 scans. Obtained sedimentation boundaries were fitted based on the equation by the continuous sedimentation coefficient model in the SEDFIT software (Beckman Coulter) to acquire the sedimentation coefficient disttribution. The parameters were set to as follows; resolution: 100, s_{min}: 100, s_{max}: 150, friction: 1.2, μ (buffer density): 1.02 g/cm^3, viscosity: 0.01002 poise and partial specific volume: 0.73 cm^3/g. Sedimentation coefficient was converted to molecular mass (M) by the Svedberg equation:

$$M = RTs/\big((1-\nu\rho)D\big)$$

where R is the gas constant, T is the absolute temperature, s is the sedimentation coefficient, ν is the partial specific volume, ρ is the solution density and D is the diffusion coefficient. D is calculated from the Einstein-stokes equation with the DLS diameter.

4. 2. 5. Surface plasmon resonance measurement

The interaction between glucose binding lectins and cG-PM was quantified using a BIACORE T200 (Cytica, Marlborough, MA, USA) as previously described in *the section 3. 2. 10.*

4. 2. 6. Cellular experiments

The cellular association of cG-PMs and G-12kPM to GLUT-1 highly expressing cancer cells (MDA-MB-231) and rat primary brain endothelial cells was evaluated for the purpose of certificate that cocktail PEGylation demonstrates the imroved accessibility of ligand molecules conjugated to long PEG chains to targeted membrane transporters GLUT-1 on the surface of culturing cells *in vitro*. These experiments were conducted as previously described in *the section 3. 2. 7, 3. 2. 8, and 3. 2. 9*.

4. 2. 7. Biodistribution of cG-PM

To investigate the effect of cocktail PEGylation on the target recognition ability of ligand molecules tethered to longer PEG chains *in vivo*, biodistribution of cy5-labeled cG14-2k50%PM, cG15-2k60%PM and cG16-2k70%PM were evaluated following the same procedure described in *the section 3. 2. 11*.

4. 2. 8. IVRT-CLSM observation of cG-PM penetrating BBB

To directly observe the BBB crossing of cG-PMs, Balb/c mice (female, 7 weeks) were fasted for 24 hours, and then anesthetized with 2.5 % isoflurane. The mouse was subjected on a Thermoplate (Tokai Hit, Tokyo, Japan) after the skull of mouse was partially exposed. The surface of brain was attached with a coverslip (Muto Pure Chemicals, Tokyo, Japan) under a proper pressure. Then the mouse was intravenously administrated with 200 μL of cy5-labeled cG-PM samples (1 mg/mL in D-PBS(-)), and 30 minutes after, the mouse was administrated with 200 μL of glucose solution at a concentration of 20 wt% in D-PBS(-) intraperitoneally. The fluorescence signal of cy5-labeled cG-PMs in the brain parenchyma were acquired using an A1R confocal laser scanning microscopy system (Nikon Co., Tokyo, Japan) connected to an upright Eclipse EN1 (Nikon Co.). Fluorescent intensity was recorded at several region of interest (ROI) points covering parenchymal tissue. Obtained images were processed using NIS-Elements software (Nikon Co.).

4. 2. 9. Immunohistochemical analysis of mice brain section

Mice were reared without food for 24 hours, and then intravenously injected with the solution of cy5-labeledcG2k50, 60 and 70%PM, followed by an intraperitoneal injection of glucose solution at a concentration of 20 wt% in PBS. 48 h after micelle administration, mice were euthanized, and perfused with PBS and 4% PFA. The mice brains were fixed overnight in 4% paraformaldehyde at 4 °C and sequentially immersed in 20 wt% overnight and subsequently 30 wt% sucrose solution at 4 ℃. The fixed brains

were frozen in cooled hexane (-100 ℃) and sliced into 14 μm thickness sections using a CM1950 cryostat (Leica Microsystems, Wetzler, Germany). The sliced sections were immunolabeled with antibodies against PECAM-1 (1:300) to visualize BCECs. Next, the sections were incubated with an Alexa Fluor 488-conjugated secondary antibody. The cell nuclei were stained with DAPI during mounting the section. All images were acquired with LSM880 laser scanning microscope (Carl Zeiss, Zurich, Switzerland) and processed using ImageJ FIJI.

4. 3. Results and discussion

4. 3. 1. Characterization of cG-PM

For these results, we confirmed that longer PEG chains restrain GLUT1 recognition of glucose ligands conjugated to G-PM, even if the number of glucose molecules on the surface of G-PM is the same, and decreases brain targeting efficacy of the micelles. The installation of glucose molecules to the end of longer PEG chains is estimated to decrease their affinity to target membrane protein, while the number of accessible ligands per nanoparticle declined. Since steric repulsion with neighboring PEG chains increases by increasing of chain length, the probability that the ligand attached to long PEG exposes on the surface of nanoparticle decreases. G-PM with long PEG chains showed less target recognition because of less effective number of ligands per micelle due to high steric repulsion with neighboring PEG chains. To get further understanding on the effect of PEG chains on G-PM recognition to GLUT-1, we focused on the technique called cocktail PEGylation, which allows increasing the accessibility of ligand molecules by mixing relatively shorter PEG chains with longer PEG chains conjugated with ligands. The improved ligand recognition by cocktail PEGylation has been revealed

in vitro [ref]. Here, we focused on G-12kPM, which showed lower brain accumulation rate compared to G-5kPM and G-2kPM, to develop cocktail PEGylated G-PM (cG-PM). Thus, a series of cocktail PEGylated micelles were prepared by mixing polyanion solutions containing Gluc-PEG(12k)-PAsp, MeO-PEG(12k)-PAsp and MeO-PEG(2k)-PAsp with polycation solutions of MeO-PEG(2k)-P(Asp-AP). We referred to these micelles as cGX-2kY%PM, where X is the glucose number in a PM and Y is the weight ratio of block copolymer having 2k PEG to all block copolymers (**Scheme 4-1.**). All cG-PMs presented unimodal diameter of 40 nm regardless of the ligand density and mixing ratio of short PEG chains (Y) from 50 to 70% (**Table 4-1.**). The spherical morphology of each cG-PM was confirmed by TEM (**Figure 4-1.**). In addition, the molecular weight of cG-PMs was measured by SLS, and the association number was calculated to be from 52 polymers for cG14-2k50%PM to 63 polymers for cG16-2k70%PM, which are larger than that of G-12kPM, *i.e.* 44 polymers. Unimodal distribution of cG-2k50%PM was observed by the analytical ultracentrifugation (**Figure 4-2.**). It is confirmed that the separation of micellar association number population does not occur due to cocktail PEGylation.

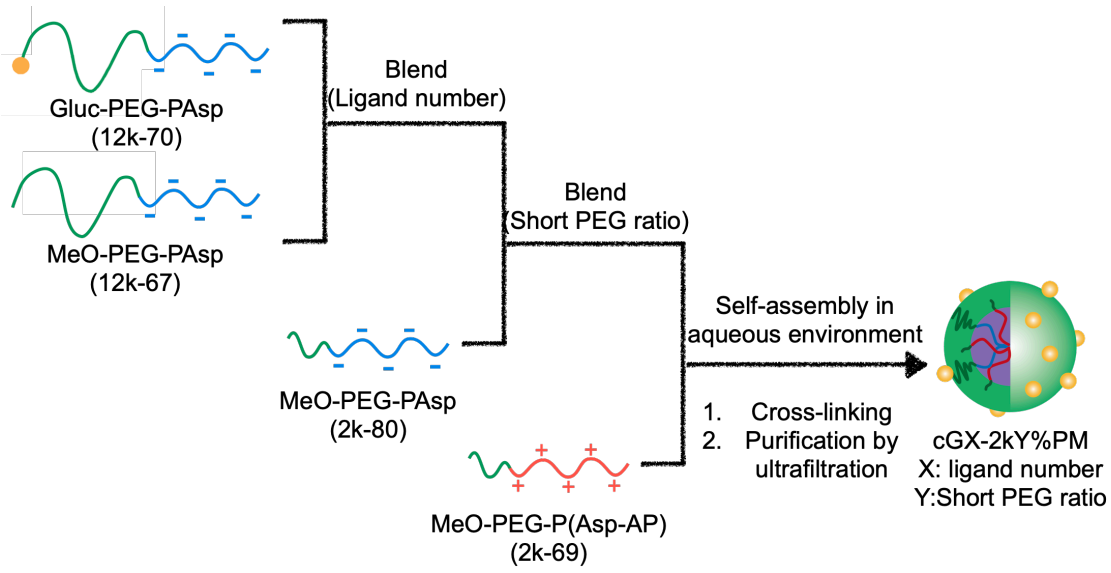

Scheme 4-1. Preparation of cG-PM from building block copolymers the chain length of PEG segment of which are 12,000 Da or 2,000 Da

Table 4-1. Characterization of cG-PMs

MW of PEG; 12000 Da : 2000 Da	Diameter[a)] [nm]	PdI[b)]	MW of micelles[c)] [$\times 10^6$ Da]	Micellar association number[d)]
50:50	41.8 ± 0.47	0.061	1.31	52
40:60	38.9 ± 0.29	0.020	1.43	60
30:70	39.7 ± 0.37	0.025	1.44	63

[a)]Determined by DLS (n = 3, means ± SD); [b)]Polydispersity index of nanoparticles determined by DLS (n = 3); [c)]Determined by SLS

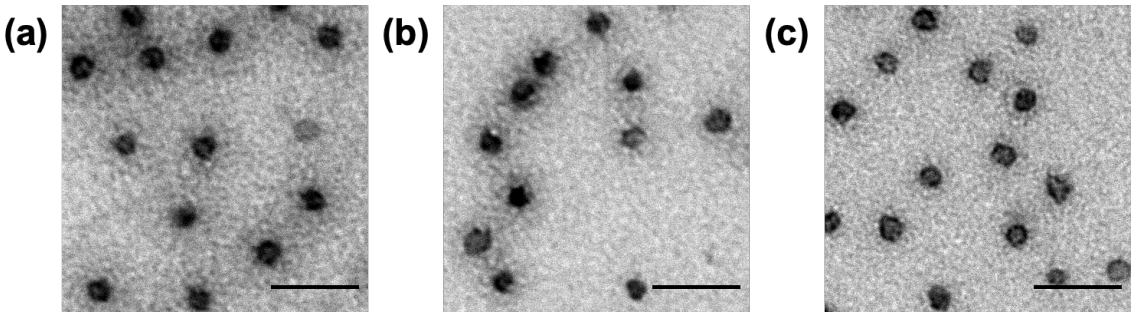

Figure 4-1. Transmission electron microscopic images of (a) cG-2k50%PM, (b) cG-2k60%PM and (c) cG-2kP70%M

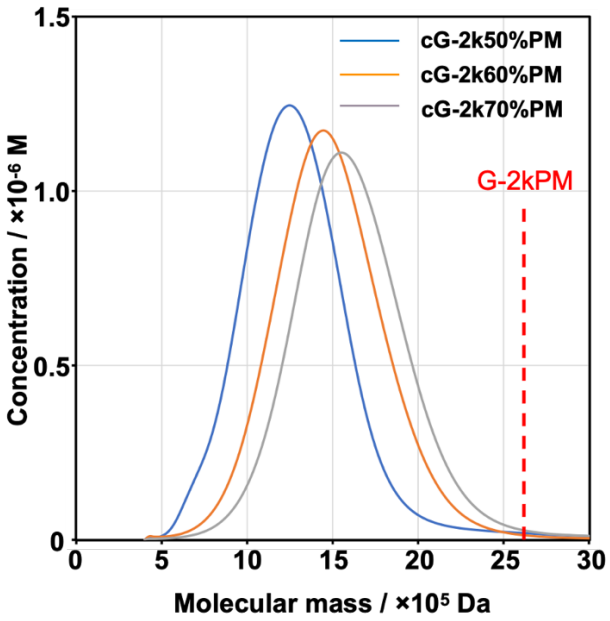

Figure 4-2. Molar mass distribution of cG-PMs analyzed by ultracentrifugation (blue: cG-2k60%PM, orange: cG-2k60%PM and gray: cG-2k70%PM)

4. 3. 2. Effect of shorter PEG ratio on the interaction between cG-PM and GLUT-1 highly expressing cells

The binding affinity of G-cocktail PM to GLUT-1 expressing on cultured cells was evaluated by quantifying Cy5-labeled G-cocktail PM associated with MDA-MB-231 cells. The amount of G-cocktail PM associated with the cells highly expressing GLUT-1 significantly increased compared to that of cG0-PM, which has no glucose ligand (**Figure 4-3.**). The cellular association of cG-PM was inhibited by GLUT inhibitors, phloretin and cytochalasin B, indicating that the interaction is mediated by glucose ligands and GLUT-1(**Figure 2(b)**). The results confirmed that cocktail PEGylation provide target recognition to GLUT-1 to the glucose molecules conjugated to long PEG (MW = 12 kDa). Notably, a larger ratio of short PEG increased the GLUT-1 recognition of the micelles, and cG16-2k70%PM with the highest ratio of 2 kDa PEG showed the highest binding to MDA-MB-

231 cells. This result is consistent with the result of cellular association of cG-PM with rat primary endothelial cells (**Figure 4-5.**) and dissociation constant from glucose binding lectins quantified by SPR measurement (**Table 4-2**.).

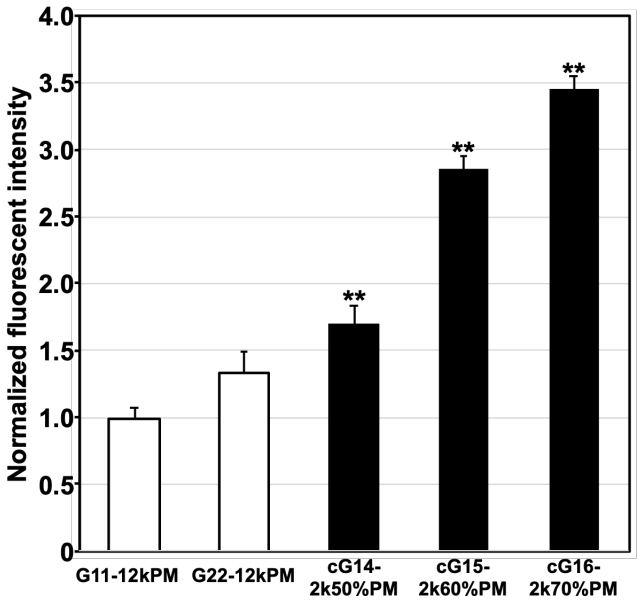

Figure 4-3. Cellular internalization of cG-PM with GLUT-1 highly expressing cancer cells (MDA-MB-231) (n = 10, means ± SEM, t-test with cG0-PM with same amount of short PEG chains, **; $p < 0.01$)

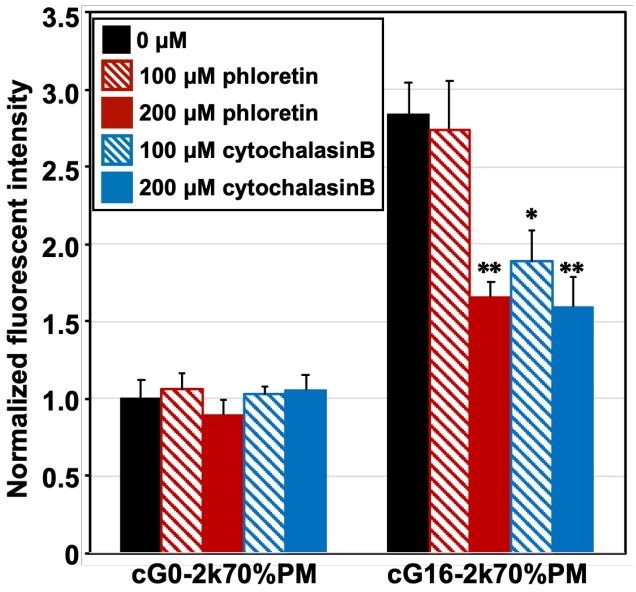

Figure 4-4. cG16-2k70%PM and cG0-2k70%PM internalization with MDA-MB-231 cells inhibited by phloretin and cytochalasin B (n = 10, means ± SEM, t-test with 0 µM, *; $p < 0.05$, **; $p < 0.01$)

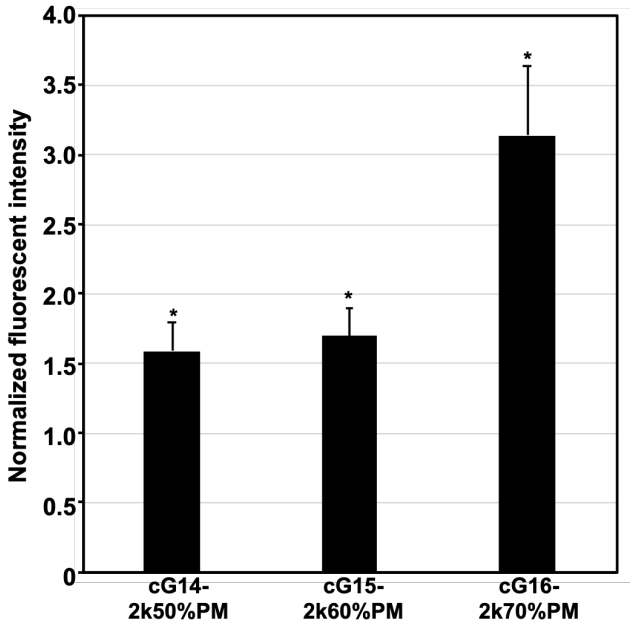

Figure 4-5. cG-PM internalization with rat primary endothelial cells (n = 5, means± SEM, t-test with cG-0PMs with same ratio of short PEG chains, * $p < 0.01$)

Table 4-2. Dissociation constant of G-PMs from glucose-binding lectin (concanavalin A) evaluated by surface plasmon resonance

	cG14-2k50%PM	cG15-2k60%PM	cG16-2k70%PM
K_D	6.58×10^{-5}	4.04×10^{-5}	1.68×10^{-5}

4. 3. 3. Cocktail PEGylation effect on the brain accumulation of G-PM

Motivated by the enhanced *in vitro* binding of cG-PM to GLUT-1 on cells, the ability of the cocktailed micelles to reach brain tissues was evaluated *in vivo*. Here, we studied the brain accumulation of cG14-2k50, cG15-2k60%PM and cG16-2k70%PM, which showed improved target recognition in the *in vitro* experiment, with the purpose of investigating the effect of cocktail PEGylation on *in vivo* GLUT-1 recognition of glucose ligands conjugated to long PEG chains. Importantly, the blood circulation of cG-PM was not affected by the mixing ratio of short PEG from 50 % to 70 %, and all micelles showed comparable long circulation, which allow us to exclude the pharmacokinetics effects on the distribution to brain tissues (**Table 4-3.**). As a result, cG-PMs showed much higher brain accumulation ratio compared to G-12kPM. The brain accumulation results of cG-PM showed that the ratio of short PEG for cocktail PEGylation controlled the access into the organ, with cG15-2k60%PM achieving 4.0 % of dose/g of brain tissue, which was more than twice the amount of cG14-2k50%PM and cG16-2k70%PM (**Figure 4-6.**). In addition, the BBB penetration of cG15-2k60%PM was successfully observed by direct brain surface observation using IVRT-CLSM (**Figure 4-7.**). Thus, while the larger amount of short PEG contributes to the improvement of target recognition of glucose ligands attached to long PEG chains, excess binding affinity to GLUT-1 prevents the dissociation of cG-PM from GLUT-1 and cG-PMs remains in the vascular wall, so that the penetration

of nanocarriers into the brain parenchyma is reduced. As demonstrated in our earlier studies, the BBB penetration of glucosylated nanocarrier consists on three independent processes; i) binding to GLUT-1 on brain endothelial cells; ii) transcytosis to brain parenchyma; and iii) dissociating from GLUT-1 on endothelial cells to reach the parenchyma side. Failure in these process limits the accessibility of the nanocarriers into brain. We investigated the accumulation of G-cocktail PM to brain endothelial cells by immunohistochemical analysis of brain sections (**Figure 4-8.**). The colocalization rate of cG16-2k70%PM with endothelial cells of brain capillaries was significantly higher than that of cG14-2k50%PM and cG15-2k60%PM (**Figure 4-9.**). This result was consistent with the result of *in vitro* cellular experiment, which indicated that a higher mixing ratio of short PEG increases the binding affinity of cG-PM to GLUT-1. Thus, we would like to point out that there is an optimal ratio of short PEG to increase the brain targeting efficacy of G-PM by cocktail PEGylation. cG-PMs accumulated in the brain were internalized microglia as well as neurons, not astrocytes (**Figure 4-10.**) after the penetration of BBB same as G-2kPMs[5].

Table 4-3. Stability of cG-PM in the blood stream 90 min after intravenous administration to mice (n = 5, means ± SEM)

	% of dose in plasma
G22-12kPM	90.4 ± 2.7
cG14-2k50%PM	98.5 ± 3.7
cG15-2k60%PM	84.2 ± 11
cG16-2k70%PM	88.2 ± 14

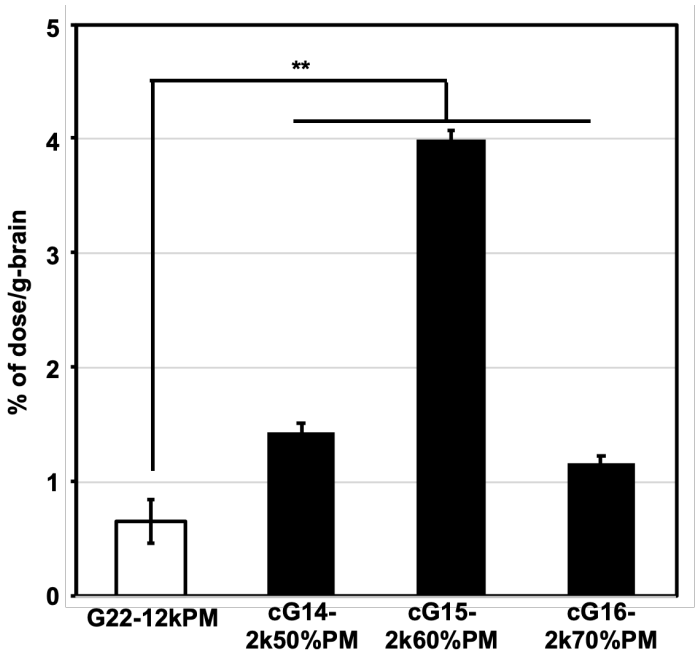

Figure 4-6. Brain accumulation ratio of cG-PM (n = 5, means ± SEM, t-test with G22-12kPM, **; $p < 0.01$)

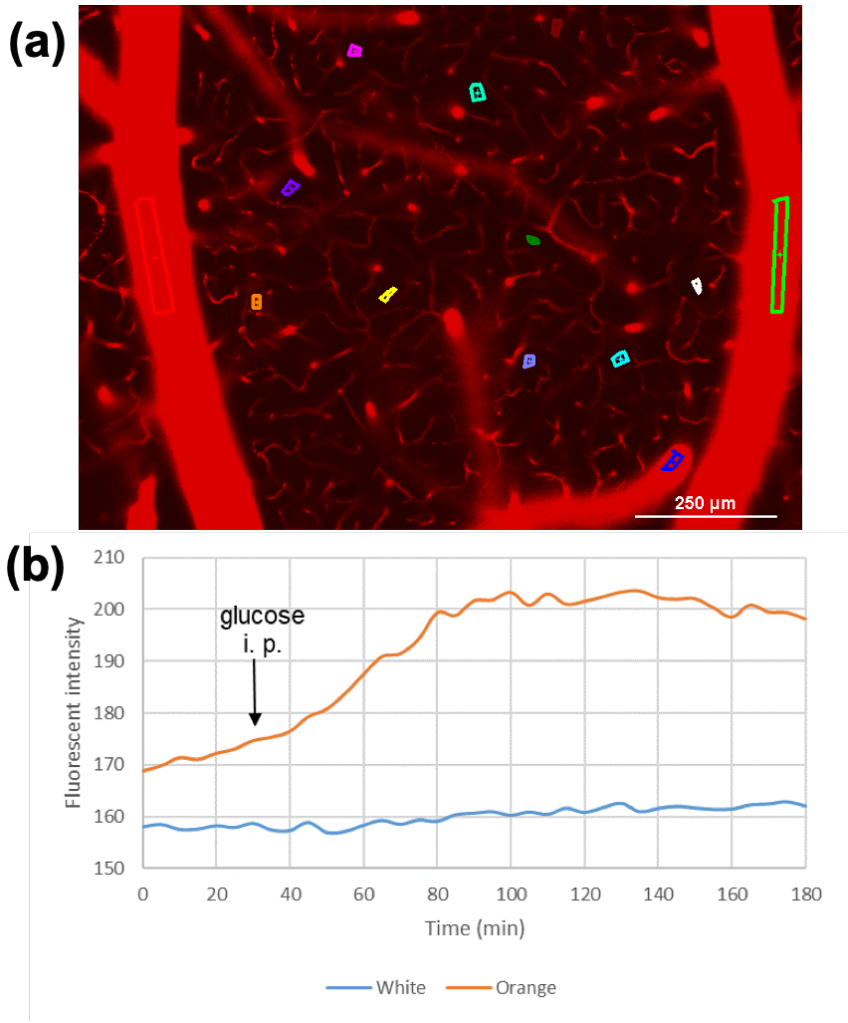

Figure 4-7. cy5-labeled cG15-2k60%PM in the brain observed using IVRT-CLSM (a) ROIs in the brain tissue and (b) averaged relative fluorescent intensity at each ROI

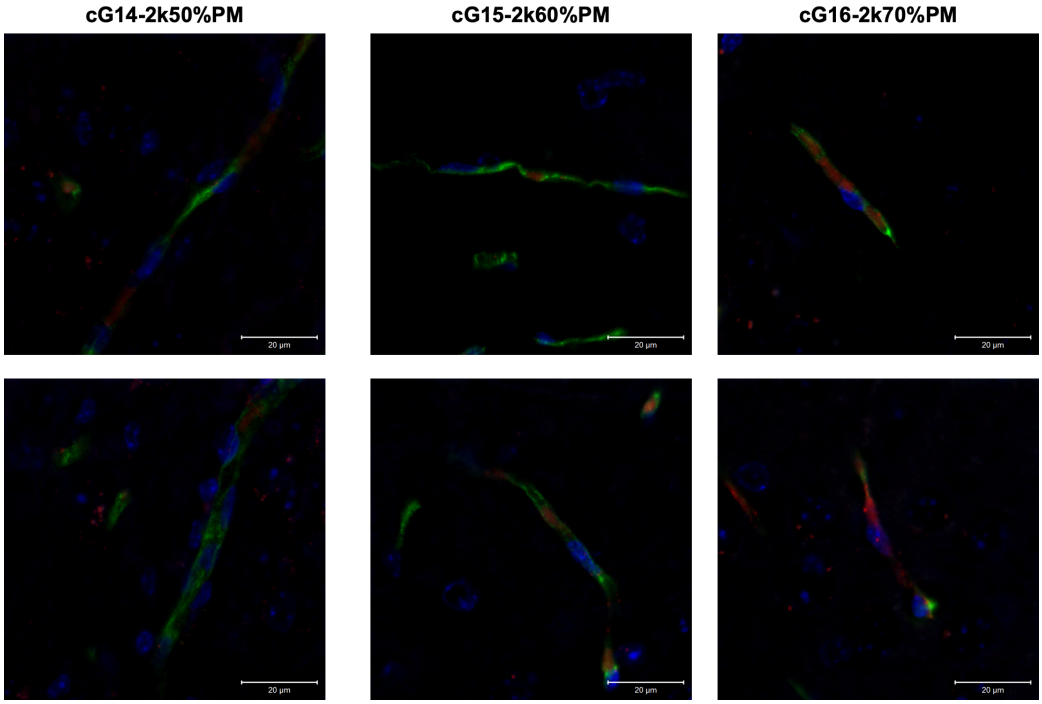

Figure 4-8. Immunohistochemical analysis of mice brain endothelial cells 48 hours after intravenous administration of cG-PM (green: PECAM-1, blue: DAPI, red: cy5-labeled cG-PM, scale bar: 20 µm)

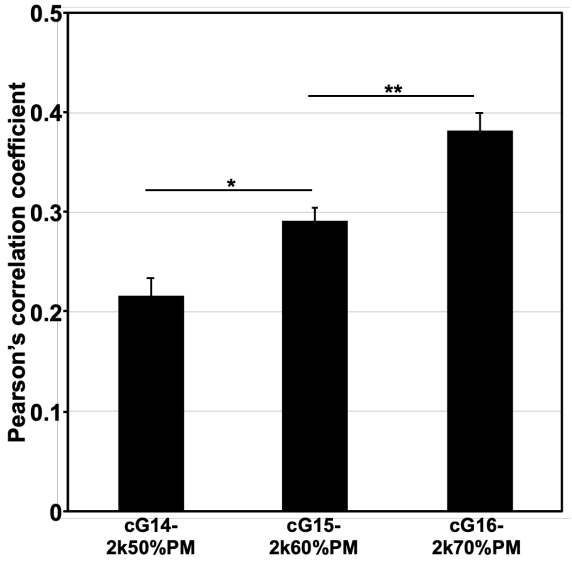

Figure 4-9. Pearson's correlation efficient of cG-PMs colocalized with brain endothelial cells (n > 100 cells were analyzed for each cG-PM, means ± SEM, *; $p < 0.05$, **; $p < 0.01$)

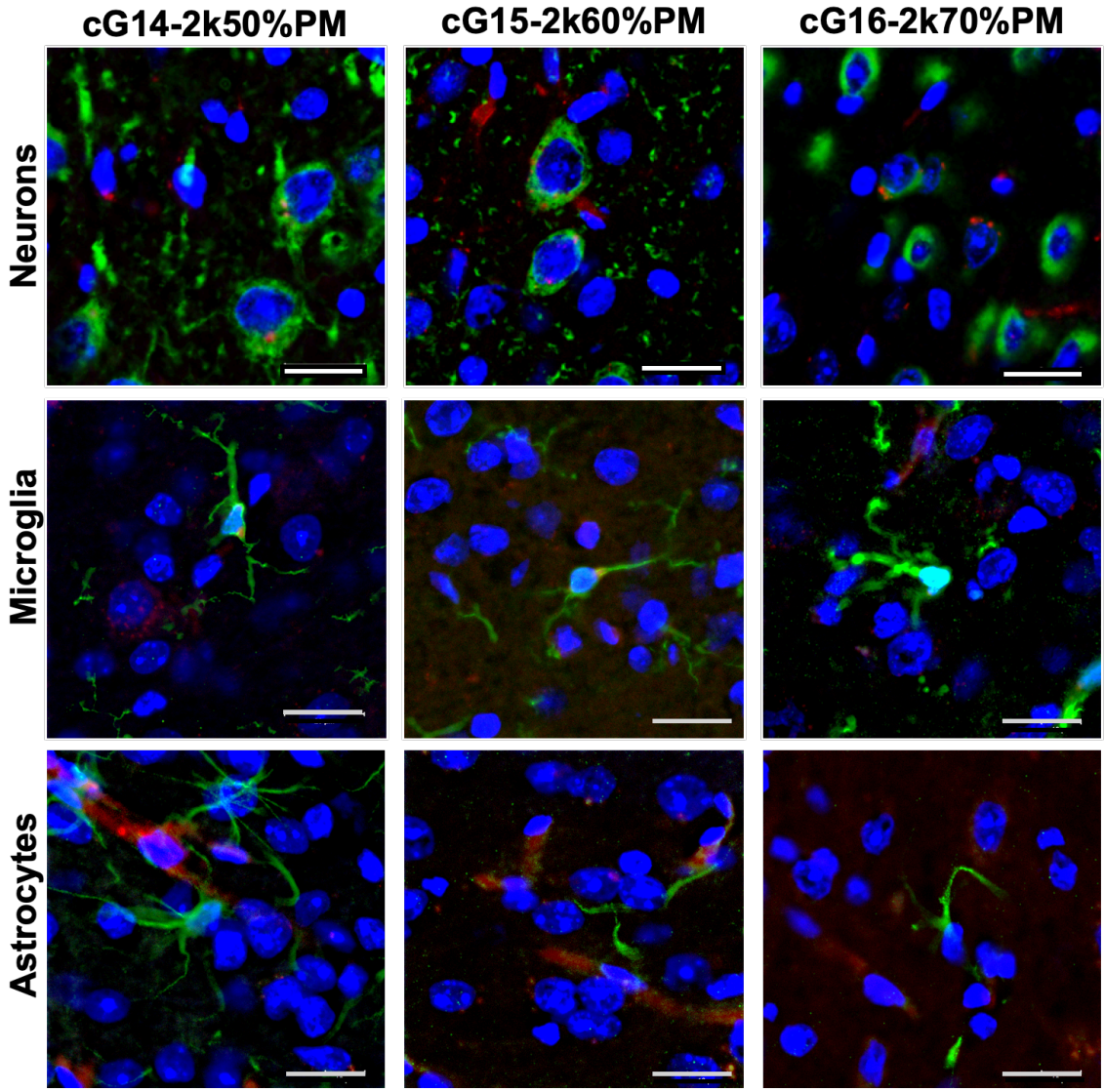

Figure 4-10. Immunohistochemical analysis of mice brain parenchymal cells

4. 4. Conclusion

In this research, cocktail PEGylated Gluc/m was successfully developed and the interaction between glucose ligand molecules and GLUT was evaluated both *in vitro* and *in vivo*. Interaction between GLUT1 on the surface of MDA-MB-231 and glucose ligands of cocktail PEGylated Gluc/m was demonstrated. It is confirmed that BBB penetration ability of Gluc/m was increased by cocktail PEGylation. It is suggested that there is an optimal condition for utilizing cocktail PEGylated Gluc/m.

4. 5. References

1. Otsuka, H.; Nagasaki, Y.; Kataoka, K., Characterization of Aldehyde-PEG Tethered Surfaces: Influence of PEG Chain Length on the Specific Biorecognition. *Langmuir* **2004,** *20* (26), 11285-11287.

2. Ishii, T.; Miyata, K.; Anraku, Y.; Naito, M.; Yi, Y.; Jinbo, T.; Takae, S.; Fukusato, Y.; Hori, M.; Osada, K.; Kataoka, K., Enhanced target recognition of nanoparticles by cocktail PEGylation with chains of varying lengths. *Chemical Communications* **2016,** *52* (7), 1517-1519.

3. Pearson, R. M.; Sen, S.; Hsu, H. J.; Pasko, M.; Gaske, M.; Kral, P.; Hong, S., Tuning the Selectivity of Dendron Micelles Through Variations of the Poly(ethylene glycol) Corona. *ACS Nano* **2016,** *10* (7), 6905-14.

4. Pannuzzo, M.; Esposito, S.; Wu, L. P.; Key, J.; Aryal, S.; Celia, C.; di Marzio, L.; Moghimi, S. M.; Decuzzi, P., Overcoming Nanoparticle-Mediated Complement Activation by Surface PEG Pairing. *Nano Lett* **2020,** *20* (6), 4312-4321.

5. Anraku, Y.; Kuwahara, H.; Fukusato, Y.; Mizoguchi, A.; Ishii, T.; Nitta, K.; Matsumoto, Y.; Toh, K.; Miyata, K.; Uchida, S.; Nishina, K.; Osada, K.; Itaka, K.; Nishiyama, N.; Mizusawa, H.; Yamasoba, T.; Yokota, T.; Kataoka, K., Glycaemic control boosts glucosylated nanocarrier crossing the BBB into the brain. *Nat Commun* **2017,** *8* (1), 1001.

Chapter 5.
Conclusions

5. 1. Conclusions

The present study focused on universal structural parameters of polymeric micelle as drug delivery carrier targeting blood-brain barrier (BBB) *via* glucose ligand molecule interact with glucose transporter-1 (GLUT-1) for central nervous disorders therapy.

In *chapter 2*, structural characteristics of polyion complex micelle (PIC/m) with varying charge mixing ratio in core-forming oppositely charged segments were evaluated, and then the performance of these PIC/m in the biological condition as a DDS carrier was investigated. PIC/m formation was performed with a wide range of charge mixing ratio ([carboxylate]/[amine], C/A) across a stoichiometry with a diameter of 30 to 50 nm, narrow size distribution and spherical morphology. The decreasing of surface charge potential with from neutral to carboxylate rich PIC/m was observed by electrophoretic light scattering measurement and remaining polyanion block copolymers were detected after micellar formation by size exclusion chromatography when C/A $\geq$ 1.10. Proton nuclear magnetic resonance (^{1}H-NMR) and small angle X-ray scattering (SAXS) measurement provided further detailed structural information of core of PIC/m. The decreased mobility of atoms in core-forming segment depending on increasing of C/A was observed by ^{1}H-NMR. In addition, it was suggested that PIC/m did not maintain the phase separated core-shell structure with C/A = 1.10 from SAXS result while PIC/m with C/A from 0.90 to 1.05 successfully obtained core-shell structure nanoparticle. Thus, these structural parameters confirmed to determine the *in vivo* performance of PIC/m as a DDS carrier represented by the stability in the bloodstream, biodistribution, as well as the uptake by sinusoidal walls in the liver vasculature.

In *chapter 3*, the effect of hydrophilic shell-forming segment on the efficiency

of transporter-mediated ligand-installed DDS carrier targeting the brain was investigated, utilizing PIC/m with C/A = 1.05 which performed reduced non-specific distribution to organs maintaining core-shell structure. Glucose-decorated polymeric micelle (G-PM) targeting glucose transporter-1 (GLUT-1) on the blood-brain barrier (BBB) with varying chain length of poly(ethylene glycol) (PEG) was successfully fabricated with a diameter of around 30 nm and narrow size distribution regardless of PEG chain length. Note that significantly restrained micellar association number depending on increasing of PEG chain length was confirmed by static light scattering (SLS) measurement, resulted in restrained ligand number per micelle, which means same as ligand density for nanoparticles with the same size. The association of G-PM to GLUT-1 expressing cultured cells (MDA-MB-231 cells and rat primary endothelial cells) significantly determined by two parameters; 1) number of ligands and 2) length of PEG chains. These results were consistent with the dissociation constant of G-PM from sugar binding lectin quantified by surface plasmon resonance (SPR) measurement. The brain accumulation of G-PM was more significantly affected by these parameters except for the deceasing of the brain accumulation of G-PM with the shortest PEG and larger number of ligands on the surface of it. This result was consistent with the previous research which suggests the reduced brain accumulation of G-PM with excess binding affinity to GLUT-1 comparing with appropriate value followed by stacking in brain endothelial cells. Moreover, it is worth noting that multivalent interaction is necessary for ligand molecules achieving low binding affinity with 1 to 1 interaction, e. g., sugars represented by glucose. For this reason, ligand number of G-PM was the crucial parameter to delivered to the brain efficiently.

In *chapter 4*, the effect of cocktail PEGylation on the target recognition of ligand

glucose molecules conjugated to long PEG chain tethered with G-PM was investigated. In *chapter 3*, it is conformed that the interaction of ligand molecules with target proteins restrained by long neighboring PEG chains, resulted in decreased targeting efficiency of G-PM with longer PEG chains. Cocktail PEGylation is the technique improves the accessibility of ligand molecules attached to longer PEG by mixing shorter PEG chains. In this study, cocktail PEGylated G-PM (cG-PM) were successfully fabricated with the similar structural property to G-PM. It was confirmed that cocktail PEGylation significantly improved the interaction between G-PM and GLUT-1 both of *in vitro* and *in vi*vo with a range of short PEG mixing ratio from 50 to 70 %. Note that cG-2k70%PM demonstrated decreased brain accumulation ratio and promoted accumulation to brain endothelial cells comparing with cG-2k60PM even the ligand number was almost same. It was suggested that the fine tuning of binding/dissociation balance between G-PM and GLUT-1 should be considered for the fabrication of cG-PM with efficient delivery to the brain.

5. 2. Future perspectives

These findings about the structural parameters of PIC/m improve current knowledge on the formation of PIC based nanoparticulated materials, which could allow PIC/m-based carriers with structural and functional characteristics for controlling *in vivo* action. Moreover, investigated universal structural parameters of G-PM to emphasize the accumulation to the brain rationalize the structural design of DDS carrier based on G-PM as a carrier of varying types of drugs, such as nucleic acid drugs and antibody drugs for the CNS disorders therapy.

Appendix

S1. Preparation of PICm with the presence of NaCl as free counter ions

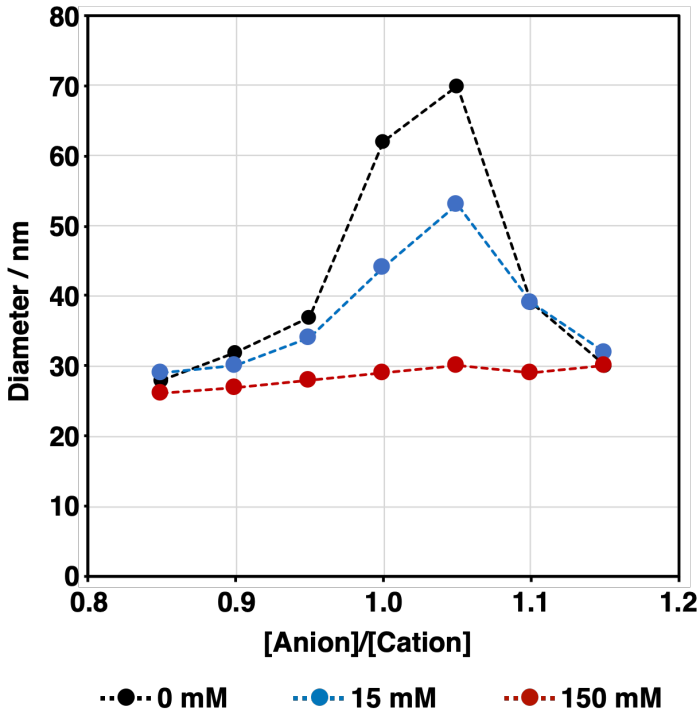

Figure S1-1. Diameter of PIC micelles prepared with MeO-PEG-PAsp (Moleculae weight (MW) of PEG = 2.2 kDa, degree of polymerization (DP) of PAsp unit = 80) and MeO-PEG-P(Asp-AP) (MW = 2.2k, DP of P(Asp-AP) unit = 76) in 10 mM phosphate buffer (PB) with and without the presence of NaCl (0, 15 and 150 mM) measured by dynamic light scattering same as described in *the section 2. 2. 8.*

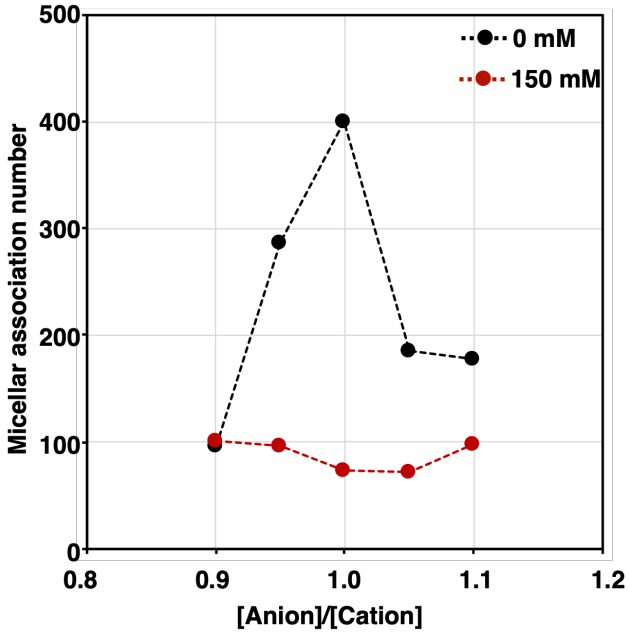

Figure S1-2. Molecular association number of PIC micelles formed with and without the presence of free counter ions in 10 mM PB (pH 7.4, 0 or 150 mM NaCl) calculated from molecular weight of PICm determined by static light scattering measurement same as described in the *section 2. 2. 9.*

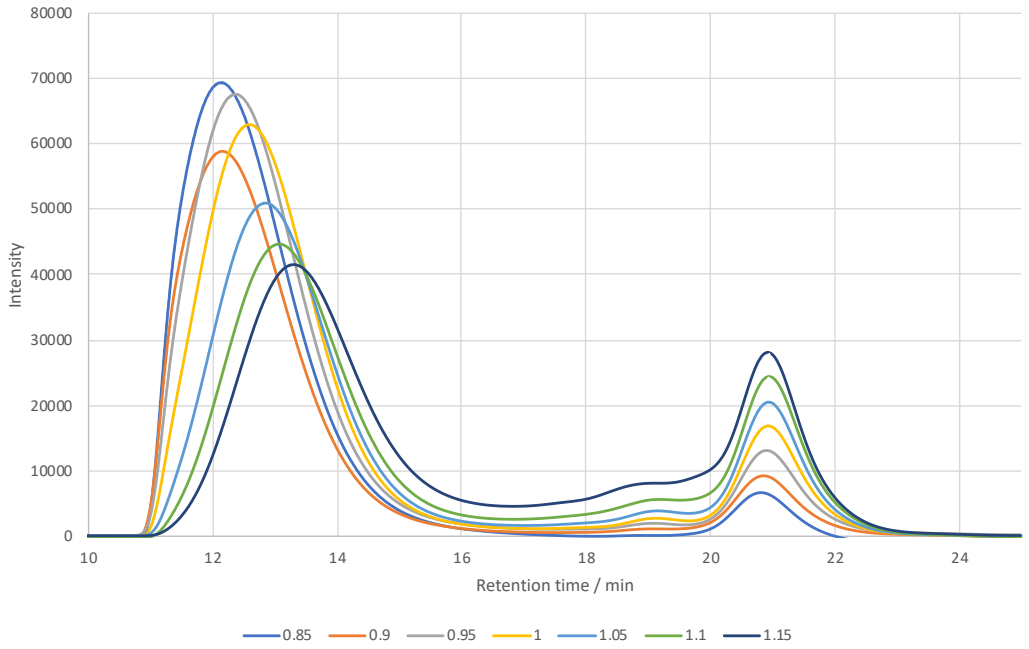

Figure S1-3. Size exclusion chromatography spectra of PIC micelles formed in 10 mM PB (pH 7.4, 150 mM NaCl) collected same as described in *the section 2. 2. 12.*

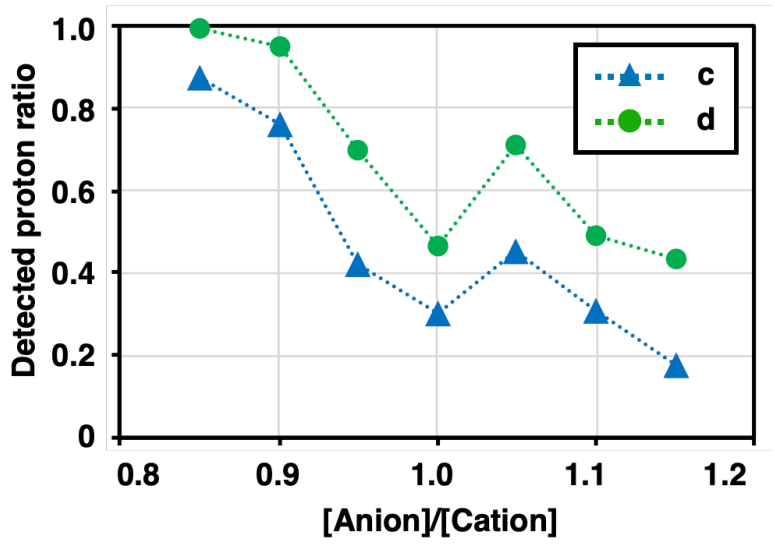

Figure S1-4. Detected proton (c and d in **Figure 2-10**.) ratio of PIC micelles formed in 10 mM PB prepared with D_2O (pD 7.0, 150 mM NaCl)

S2. Cocktail PEGylated glucose-decorated micelles (cG-PM) with less than 50 % of short PEG chains

Table S2-1. Characterization of cG-PMs

MW of PEG; 12000 Da : 2000 Da	Diameter[a)] [nm]	PdI[b)]	MW of micelles[c)] [$\times 10^6$ Da]	Micellar association number[d)]
60:40	42	0.074	1.39	57
70:30	41	0.054	1.24	53

[a)]Determined by DLS; [b)]Polydispersity index of nanoparticles determined by DLS (n = 3); [c)]Determined by SLS; [d)]Calculated from MW of micelle

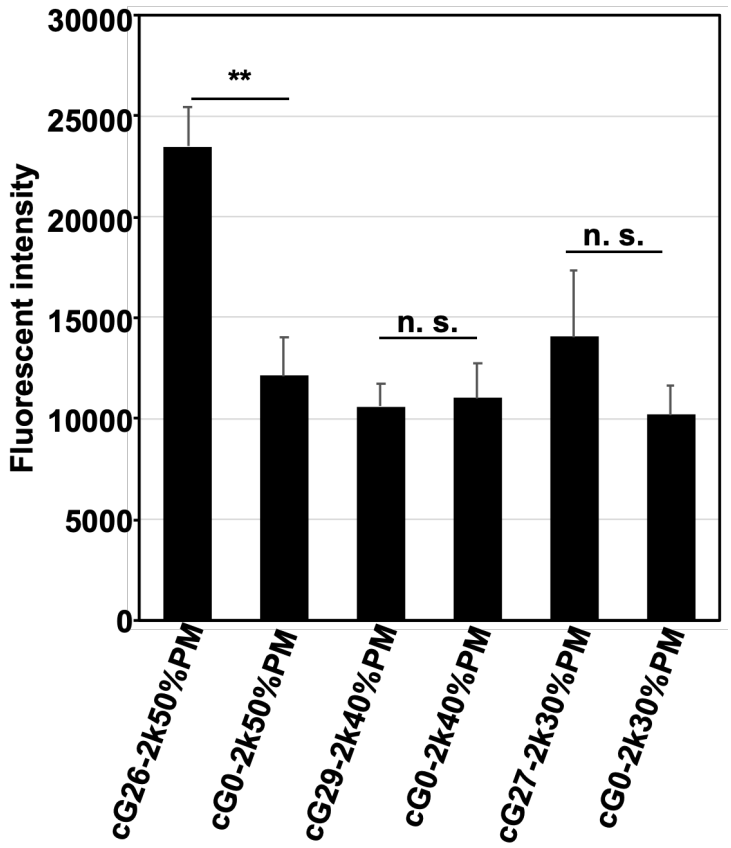

Figure S2-1. Cellular internalization of cG-PM with GLUT-1 highly expressing cancer cells (MDA-MB-231) (n = 8, means ± SE, t-test with cG0-PM with same amount of short

PEG chains, **; $p < 0.01$) investigated same as described in *the section 3. 2. 7.*

List of Publications

Ⅰ Original Articles

[1] J. Xie, D. G-Carter, T. A. Tockary, **N. Nakamura**, Y. Xue, M. Nakakido, H. Akiba, A. Dirisala, X. Liu, K. Toh, T. Yang, Z. Wang, S. Fukushima, J. Li, S. Quader, K. Tsumoto, T. Yokota, Y. Anraku, K. Kataoka, ”Dual-sensitive nanomicelles enhancing systemic delivery of therapeutically active antibodies specifically into the brain”, *ACS Nano*, Published online (2020)

[2] M. Suhara, Y. Miura, H. Cabral, D. Akagi, Y. Anraku, A. Kishimura, M. Sano, T. Miyazaki, **N. Nakamura**, A. Nishiyama, K. Kataoka, H. Koyama, K. Hoshina, “Targeting ability of self-assembled nanomedicines in rat acute limb ischemia model is affected by size”, *J. Controlled Release*, 286, 394-401 (2018)

[3] **N. Nakamura**, Y. Mochida, K. Toh, S. Fukushima, Y. Anraku, H. Cabral, “Effect of mixing ratio of oppositely charged block copolymers on polyion complex micelles for *in vivo* application”, *Polymers,* 13 (2021)

[4] **N. Nakamura**, Y. Anraku, S. Fukushima, K. Toh, H. Cabral, K. Kataoka, “Quantitative analysis of targeting ability for glucose decorated polymeric micelle as transporter-mediated drug delivery carrier targeting brain”, *in preparation*

Ⅱ Presentations

[International Meetings, Oral]

[1] **Noriko Nakamura**, Yasutaka Anraku, Shigeto Fukushima, Kazuko Toh, Horacio Cabral, Kazunori Kataoka, “Multivalent interaction between target proteins and ligand molecules on polymeric micelle penetrating blood-brain barrier”, The International Chemical Congress of Pacific Basin Societies 2020, Honolulu, 2020 年 12 月

[2] **Noriko Nakamura**, Yasutaka Anraku, Shigeto Fukushima, Kazuko Toh, Horacio

Cabral, Kazunori Kataoka, “Quantitative analysis of targeting ability for glucose decorated polymeric micelle penetrating blood-brain barrier”, ACS Spring 2020 National Meeting & Exposition, Pennsylvania Convention Center, 2020 年 3 月

[3] **Noriko Nakamura**, Yasutaka Anraku, Shigeto Fukushima, Kazuko Toh, Horacio Cabral, Kazunori Kataoka, “Target recognition of ligand molecules on the polymeric micelle with a different length of hydrophilic segment penetrating blood-brain barrier”, 2nd GLowing Polymer Symposium in Kanto, 東京理科大学葛飾キャンパス, 2019 年 11 月

[4] **Noriko Nakamura**, Yasutaka Anraku, Shigeto Fukushima, Kazuko Toh, Horacio Cabral, Kazunori Kataoka, “Development of cocktail PEGylated polymeric micelle penetrating blood-brain barrier”, 1st GLowing Polymer Symposium in Kanto, 早稲田大学, 2018 年 12 月

[5] **Noriko Nakamura**, Yasutaka Anraku, Shigeto Fukushima, Kazuko Toh, Horacio Cabral, Kazunori Kataoka, “Interaction between target membrane proteins and ligand-decorated polymeric micelles penetrating blood-brain barrier”, 2018 MRS Fall Meeting and Exhibit, Hynes Convention Center, 2018 年 11 月

[6] **Noriko Nakamura**, Yasutaka Anraku, Shigeto Fukushima, Kazuko Toh, Horacio Cabral, Kazunori Kataoka, “Interaction analysis of ligand molecules on polymeric micelle penetrating blood-brain barrier”, Biomaterials International 2018, 東京大学, 2018 年 7 月

[7] **Noriko Nakamura**, Yasutaka Anraku, Shigeto Fukushima, Kazuko Toh, Horacio Cabral, Kazunori Kataoka, “Interaction analysis between ligand molecules and target receptors”, CIMR/University of Tokyo 2017 Student Symposium, Cambridge Institute for Medical Research, 2017 年 9 月

[International Meetings, Poster]

[1] **Noriko Nakamura**, Yasutaka Anraku, Shigeto Fukushima, Kazuko Toh, Horacio Cabral, Kazunori Kataoka, “Analysis of the interaction between target membrane proteins and ligand molecules on polymeric micelles”, the 12th SPSJ International Polymer Conference, 広島国際会議場, 2018 年 12 月

[Domestic Meetings, Oral]

[1] **中村乃理子**、福島重人、カブラルオラシオ、片岡一則、安楽泰孝、「PIC 型高分子ミセルにおける混合電荷比が生体内挙動に及ぼす影響」、第 69 回高分子学会年次大会、福岡国際会議場、2020 年 5 月

[2] **中村乃理子**、安楽泰孝、福島重人、藤加珠子、カブラルオラシオ、片岡一則、「Target recognition ability of DDS carrier penetrating blood-brain barrier with different molecular weight of hydrophilic shell」、第 68 回高分子学会年次大会、大阪国際会議場、2019 年 5 月

[3] **中村乃理子**、安楽泰孝、福島重人、藤加珠子、カブラルオラシオ、片岡一則、「Interaction analysis between glucose molecules on polymeric micelle and GLUT1 as a targeting membrane protein」、日本化学会第 98 回春季年会、日本大学理工学部船橋キャンパス、2018 年 3 月

[4] **中村乃理子**、安楽泰孝、福島重人、藤加珠子、カブラルオラシオ、片岡一則、「血液脳関門突破を指向した高分子ミセル表層のリガンド分子の標的認識能評価」第 39 回日本バイオマテリアル学会大会、タワーホール船堀、2017 年 11 月

[Domestic Meetings, Poster]

[1] **中村乃理子**、安楽泰孝、福島重人、藤加珠子、カブラルオラシオ、片岡一則、「血液脳関門突破を指向した高分子ミセル表層のリガンド分子の標的認識能評価」、第 41 回日本バイオマテリアル学会大会、つくば国際会議場、2019 年 11 月

[2] 中村乃理子、安楽泰孝、福島重人、藤加珠子、カブラルオラシオ、片岡一則、「血液納竿門の突破を指向した薬剤送達担体におけるリガンド分子と標的膜蛋白質との相互作用」、TEIJIN MIRAI FORUM 2019、大崎ブライトコアホール、2019 年 2 月

[3] 中村乃理子、安楽泰孝、渡邉拓也、福島重人、藤加珠子、カブラルオラシオ、片岡一則、「中枢神経系を標的とした高分子ミセルにおけるリガンド-受容体相互作用の評価」、第 66 回高分子学会年次大会、幕張メッセ、2017 年 5 月

[4] 中村乃理子、迫田龍、太田誠一、金子誠、矢冨裕、伊藤大知、「血小板接着ペプチド修飾ヒアルロン酸 in situ 架橋ハイドロゲルの開発」、第 66 回高分子学会年次大会、幕張メッセ、2017 年 5 月

[5] 中村乃理子、迫田龍、太田誠一、金子誠、矢冨裕、伊藤大知、「血小板接着ペプチド修飾ヒアルロン酸 in situ 架橋ハイドロゲルの開発と局所止血材への応用」、化学工学会第 82 年会、芝浦工業大学豊洲キャンパス、2017 年 3 月

Ⅲ Patents

【公開中】

[1] 片岡一則、安楽泰孝、中村乃理子、「脳への薬剤送達用のキャリアおよびこれを含んでなる組成物」、特願 2017-95055、ナノ医療イノベーションセンター

【申請中】

[2] 安楽泰孝、片岡一則、福里優、中村乃理子、西薗拓也、「脳内の局在を制御するための薬剤送達システム及びその方法」、PCT/JP2020/19007、東京大学

[3] 安楽泰孝、宝地戸秀和、中村乃理子、ホラシオカブラル、「十分な血中滞留性を有し、かつ、グリア限界膜への透過性が改善されたポリイオンコンプレックス型ポリマーソーム」特願 2020-83201、東京大学

[4] 安楽泰孝、片岡一則、Jingbing Xie、**中村乃理子**、「抗体の抗原結合性断片を脳へ送達するための方法および組成物」、特願 2019-85661、ナノ医療イノベーションセンター

Ⅳ Awards

[1] 第 41 回日本バイオマテリアル学会大会　優秀研究ポスター賞　2019 年 11 月

[2] TEIJIN MIRAI FORUM 2019　帝人賞(最優秀ポスター賞)　2019 年 2 月

[3] 第 66 回高分子学会年次大会　優秀ポスター賞　2017 年 5 月